Università degli studi di Milano – Bicocca

Doctorate in Material Science – XXVII cycle

A dissertation submitted for the degree of
Doctor of Philosophy in Materials Science

Polycrystalline Silicon as Thermoelectric Material

Bringing the nanotechnological advantage into bulk

Advisor:
Prof. Dario Narducci

Candidate:
Bruno Lorenzi

Dean of the Doctorate:
Prof. Gian Paolo Brivio

March 2015

"Well, in our country" said Alice, still panting a little,
"you'd generally get to somewhere else-if you run very
fast for a long time, as we've been doing."
"A slow sort of country!" said the Queen.
"Now, here, you see, it takes all the running you can do,
to keep in the same place. If you want to get somewhere
else, you must run at least twice as fast as that!"

-Alice's Adventures in Wonderland-
Lewis Carroll

I would like to thank:

My advisor Prof. Dario Narducci for his support and his guidance during my PhD study. He has been a very correct and wise leader, always able to support my work, respecting my opinions, debating my propositions and improving my ideas. This work has been possible only because his patient and indispensable presence.

Prof. Ken Goodson who made possible the six months long visit I made at the Stanford University in California. Due to his sense of foresight and confidence on this project I was able to practice this experience which has had a huge impact on my work and life.

Prof. Giampiero Ottaviani who led the group at the University of Modena and Reggio Emilia which provided most of the samples necessary for this work. I am very grateful to him for all support and the fruitful discussions on silicon and its properties, during which he always shared his great and deep experience in this field.

Prof. Gian Paolo Brivio Dean of the doctorate in Material Science at the University of Milano Bicocca, for his help in guiding me through the obligations related to this PhD course.

Maria Cristina Fassina and Linda Hubert respectively secretary of the PhD course that I followed, and secretary of the research group NanoHeat at Stanford University. Without their help I would be lost in the dense jungle of the administrative bureaucracy.

Prof. Stefano Frabboni, University of Modena and Reggio Emilia, for providing me "the eyes", by TEM analysis, and making possible to look inside of the secrets of the samples object of this thesis. His efforts and his suggestions has constituted a great part of this work.

Dr. Rita Tonini, University of Modena and Reggio Emilia, who along with Prof. Ottaviani works at samples preparation, in particular the helium implantation and the TPD analysis.

Dr. Alberto Roncaglia, IMM - CNR of Bologna, for having prepared samples necessary to understand the features of the material object of this thesis, and for having investigated the possibility of in-plane thermal characterizations.

Prof. Xanthippi Zianni and Dr. Neophytos Neophytou who established the computational framework which strengthened and supported the experimental efforts.

Dr. Andrea Arcari who introduced me to the basics of thermoelectric measures, for the tons of friendly and useful discussions which we have had. Also I would like to thank him particularly for having given me the basics on lab electronics and programming.

Prof. Maurizio Acciarri, University of Milano Bicocca, to whom I owe what I know in Hall measurements and photovoltaics. I would like to thank him for the time dedicated to the construction of the model describing HTEPV devices, and to preparation of the papers we have published on that.

Marc Dunham, PhD candidate at Stanford University, who hosted me at Stanford, and did the TDTR characterization on the samples object of this thesis. Without his help and courtesy, inside and outside the campus, I would not have obtained any result.

Aditya Sood, PhD candidate at Stanford University, for his help, time and efforts in introducing me and Marc to the TDTR measurement technique and setup.

Prof. Mehdi Asheghi, Stanford University, for the time which he has dedicated to this work and for his precious advices during our meetings.

Prof. Luciano Colombo, University of Cagliari, for the useful discussion during which he gave me some precious advices, with cordiality and humor. I would like to thank him also for his help during the writing of this thesis.

My colleagues at the University of Milano Bicocca, Laura, Andrea (Scacca), Sara, Raluca, Michele (Bambi), Khung, Alessia, Silvia, Daniela (Samantha), Pupetto, Pam, Jasmine, who gave me a lot of support and help in everyday working routine and university life, and who can be defined as good friends.

My colleagues at Stanford University, Michael, Shilpi, Joe, Junwan, Woosung, Tom, Matt, which made my visit at Stanford very enjoyable.

My family that always supported me during this path, applauding my successes, cheering me up during bad time, encourage me when I was lost.

At last, my wife. Thanks for your patience, your smile, your love, your support. I cannot even imagine my life without you, and I won't never be able to thank you enough for being who you are.

Abstract

The worldwide issue of the growing energy demand, along with the rapid decrease of the conventional fossil sources and the global warming, is one of the key challenges of this century. Among the solutions studied and developed to face these problems, reduction of the energy wastes and a strong energetic efficiency improvement are the most relevant. Since it is well known that nearly the 60% of the energy generated around the world is rejected as heat, the possibility to recover even just a small percentage of this huge amount of energy could led to a significant reduction of the consumption of fossil fuels and CO_2 emissions.
Thermoelectric devices are one of the viable options, especially because they can generate electrical power even with small temperature gradients and without moving parts. Energy conversion ratio for a thermoelectric material is related to its figure of merit: $ZT = \frac{\alpha^2\sigma}{\kappa}T$, where the numerator, often called power factor (PF), is the product between the square of the Seebeck coefficient (α) and the electrical conductivity (σ), and the denominator is the thermal conductivity (κ). Although thermoelectric efficiencies, achievable in case of bulk materials, are small compared to that of conventional power sources, nanotechnology has opened in the last decade new ways to increase thermoelectric performances.
In this PhD work the main activity was focused on a non-toxic abundant nanostructured material for thermoelectric applications, based on nanocrystalline silicon thin films highly doped with boron.
In the first part it will be demonstrated the possibility to induce a great enhancement of the film power factors, due to a simultaneous increase of the Seebeck coefficient and of the electrical conductivity, by annealing between 500 and 1000 °C. These enhancements have been shown to be caused by the dopant segregation (induced by thermal annealing) and the creation of a second phase, which led to an energy filtering effect. This evidence along with other characterizations led to a model which was confirmed by a computation.
In the second part it was studied the possibility to modulate the film thermal conductivity by generating a dispersion of nanovoids (NVs) using helium implantation and subsequent thermal treatments. The applicabil-

ity of this technique, known only for the single crystal case, was tested on the poly-silicon thin films. Concerning void morphology, it was observed that while the helium dose rules the film final porosity (in our case ~ 0.5 %), the characteristics of the annealing processes can be used to tune the NV morphology. In particular, since NV creation is a coalescence process it was observed an increase of the NV diameter, ranging between 1 and 20 nm, with the annealing temperature. Furthermore it was characterized the compatibility of the energy filtering effect with the NV generation process, noting a reduction of PF enhancement by a factor two due to the slower dopant segregation. Finally it was measured the thermal conductivity of a batch of samples treated at different temperatures (hence with different NVs morphologies) but with the same porosity, observing a proportionality between κ and the distance between NVs. This dependency was demonstrated to break down when the NV diameter is small, because of the frequency dependence of the phonon-NV scattering mechanism. Unfortunately, although it was showed that helium implantation is a useful technique to modulate the κ of nanocrystalline silicon thin films and that it is compatible with the mechanism of PF enhancement, minimal κ and maximum PF were found occurring at different annealing temperatures. This mismatch, although seemingly surmountable, limited ZT values to ~ 0.34.

Overall, it may be concluded that heavily boron-doped nanocrystalline silicon may qualify as an interesting system to develop thermoelectric devices meeting acceptable performances with remarkably low material costs.

Furthermore a theoretical analysis on the possibility to couple Thermo-Electric Generators (TEGs) with single–junction solar cells in Hybrid ThermoElectric PhotoVoltaic (HTEPV) devices was done as corollary to the main activity. In this study a model to predict the performances of the hybrid device is proposed. Moving from the so-called Shockley-Queisser limit, the maximum device efficiency is computed in two different configurations. The first just coupled the solar cell to the thermoelectric device; while the second made use of an additional absorbing layer to partially convert also the low-frequency tail of the solar spectrum.

The analysis led to the conclusion that in the first class of HTEPV devices the TEG stage only mitigates the standard decrease of the PV efficiency for increasing T_{cell}, suggesting that in this configuration HTEPV devices

are unlike to be a convenient option. The situation was found to be different in the second case, where the hybrid device was shown to operate with an enhanced efficiency exceeding the maximum achievable efficiency in a single–junction cell. It was further shown that the second construction also enables the use of wide bandgap materials in the PV stage, opening novel perspectives in the selection of photovoltaic materials.

Contents

List of Figures

Chapter 1

Introduction

1.1 Worldwide Energetic problem

It is estimated that the world population will continue to grow from today's 7.2 billion, to $\approx$ 9.6 billion in 2050 and then to $\approx$ 10.9 billion in the 2100 (Fig. 1.1a). The impulse to a such increase will come from the developing countries and especially from Asia (at least until 2050) and Africa [1].
More people means more food, more water and more energy to sustain their lives.

The main question is: will there be enough of these primary sources for everyone?
Nobody can answer this question.
Transcending the vital matters of food and water that are out of the topic of this thesis, and avoiding also the fundamental problem of the global warming and of the impact of the human being on earth, the following pages will be focused on the third crucial point: energy[1].

The immediate consequence of a population increase, is an increasing energy demand. Furthermore considering that the growing countries are contemporary developing their economies, and then multiply their needs,

[1] an extremely punctual and critical reportage on the present and future perspectives regarding food, water and environment can be found in [16]

the result is an exponential growth of the energy consumptions as shown in Fig. 1.1b.
This situation may not appear alarming (avoiding the global warming) if the fossil fuels, which represent more than the 80% of the current energy supply [3], were no running out. To support this statement in Fig. 1.2 is reported, the ratio between the fossil fuels estimated reserves and their consumption in 2013 [2]. This graph shows basically how many years of fuel consumption remain.
Considering the growing demand shown in Fig. 1.1b, it clearly follows that a strong change of this trend is needed in order to avoid a worldwide collapse. In the next section the strategies implemented or under implementation in order to face this energetic crucial situation will be showed.

Another important index to take into account is the pro-capita energy consumption. Around the world this value, normally expressed in tonne of oil equivalent (toe), floats between ≈ 8 for US, ≈ 3.5 for EU, ≈ 1.3 for Asia and ≈ 0.4 for Africa [17]. It is absolutely clear that it cannot be hoped and neither possible for the developing countries world to remain in

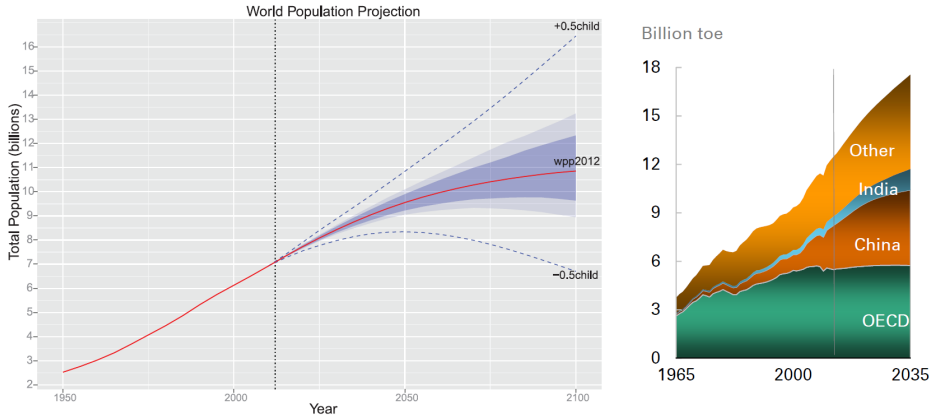

Figure 1.1: a) UN 2012 world population projection (red line), with 80% of probability (dark shaded), 95% of probability (light shaded), estimation with half a child added/subtracted from the total fertility rate. Reproduced with permission from [1]; b) Projections for the total world energy consumption divided by area until 2035, expressed in billions of equivalent tons of oil. Reproduced with permission from [2].

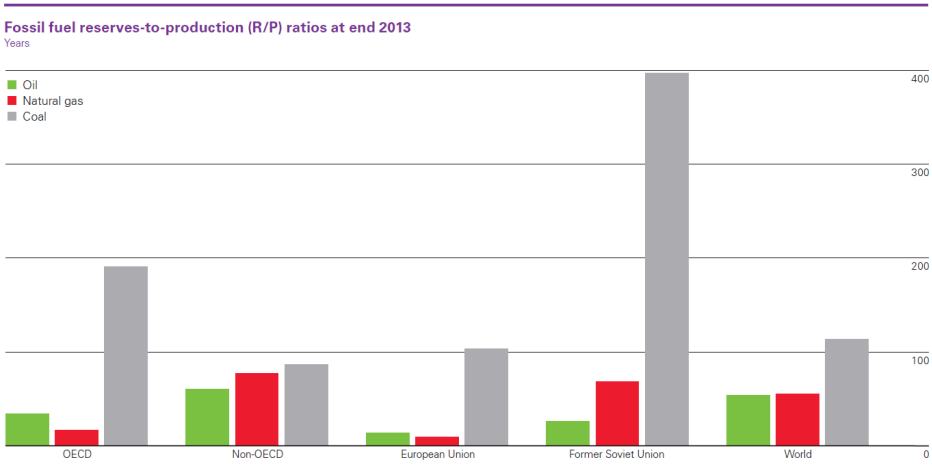

Figure 1.2: Fossil fuels reserves-to-production ratios at the end of 2013. Reproduced with permission from [2]. OECD stands for: Organisation for Economic Co-operation and Development. A list of the members can be found in [2].

its present poor conditions in order to contain the future energy demand. Furthermore not even a worldwide adjustment at the western countries level would be a viable solution.
Probably the right and sustainable consumption pro-capita is somewhere in between.
Eventually the western countries should program a contraction of their energy demand in order to accommodate the possibility for the other countries development. Furthermore they should, from the best of their scientific knowledge, develop the necessary know-how and the technologies needed to make the planet big enough to contain everyone. On the other hand the developing countries should immediately implement these technologies so as to make their growth sustainable.

It would be desirable the setting of a worldwide accepted consumption pro-capita. This individual amount of energy further to representing a guide to the political and economical decisions in the energy field, should be recognised as an inviolable human right as those already inserted in the international human right declaration.

1.2 The renewable revolution

In this section the strategies implemented around the world in order to contain and eventually partially solve the energy problems discussed in the previous section will be reported. These strategies, resumed in the provocative title of "renewable revolution", are essentially based on two kind of approaches.

The first consists in the implementation and use of renewable sources of energy in addition and/or replacement of the conventional fossil fuels.

The second focuses technological efforts onto the reduction of the energy demand through the improvement of the efficiency in producing, utilizing and delivering energy.

Both approaches are actually the main efforts implemented and pushed by governments and political programs around the world. One of the best examples is the so called 20-20-20 project of the European Community which requests the member nations the objectives of 20% of the energy demand satisfied by renewables and a decrease of at least 20% in the energy consumes plans.

1.2.1 Renewable sources of energy

With the therm "renewable sources of energy", or simply renewables, it is generally indicated a class of resources which are naturally replenished on the human time scale and the utilization of which do not prevent the possibility of their future exploitation. This intrinsic characteristic sets renewables on the opposite position compared to the fossil fuels which are instead exhaustible and that in general cannot be renewed (at least on the human time scale).
Renewable sources are numerous on our planet and their enormous potential is much bigger than the world actual energy demand. The renewables mainstreams are: wind, hydro, solar, biomass, biofuels, and geothermal. The discussion will not go into details regarding the high number of technologies and devices related to these sources, will be restricted instead to their spread and to some important features.

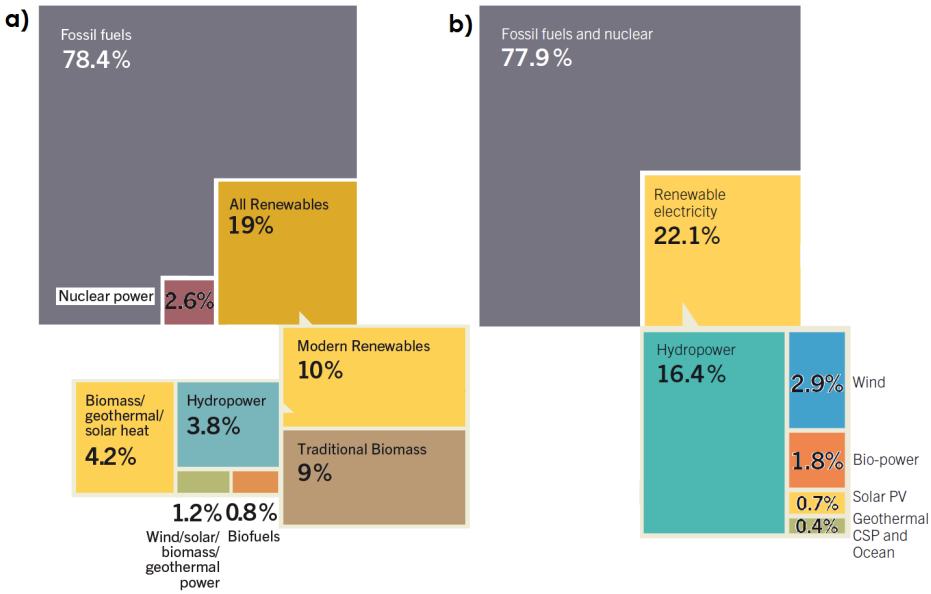

Figure 1.3: World final energy consumption in 2012 (a) and world electricity production in 2013 (b) divided among different kind of sources. Reproduced with permission from [3].

Regarding spread, in Fig. 1.3a the contribution of renewables to the world final energy consumption in 2012 is reported. As can be seen they account for nearly the 19% of the total, composed in equal part, by traditional biomasses (namely solid biomass combusted in inefficient open fires, stoves, or furnaces to provide heat for cooking, comfort, or small agricultural and industrial processes, typically in rural areas of developing countries) and modern renewables. Fig. 1.3b shows instead the renewables contribution to the world electricity production which accounts to nearly the 22%. Hydroelectric power plants dominate with 75% followed by wind, biomass, photovoltaics and others.
The historic distribution of renewable power generation around the world, without considering hydroelectrics is reported in Fig. 1.4. Europe and Eurasia lead with nearly 10% of their overall electricity generation, followed by the Americas (around 6%), Asia (with almost 4%) and Africa

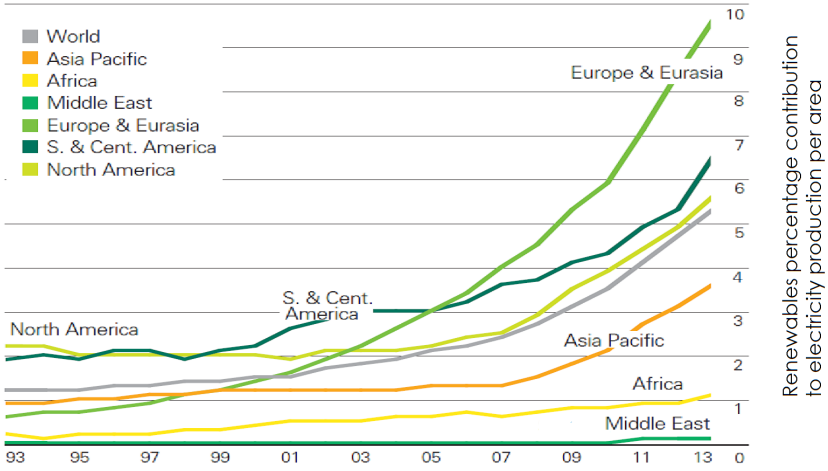

Figure 1.4: Historic world distribution of the renewable percentage contribution to electricity, without considering hydroelectrics. Reproduced with permission from [2].

and Middle East (with a smaller contributions).
The positive feature of these data is the increasing trend common to every area considered.

Now is necessary to highlight some important and general features of renewable sources which have to be considered for a proper exploitation of their potential.
One of the most important is their wide availability and diffusion over the planet. This characteristic implies the possibility of a distributed micro-generation of energy, which changes the traditional power production system and the related energy market. Before the advent of renewables in fact the production of energy and electricity were mainly centralized and delivered from few big plants to the final users. Now instead the situation is going towards an increasing de-localized generation, through small plants distributed over the territory. This micro-generation satisfies the local energy demand, and the possible surplus could be redirected towards other districts. As it will be highlighted in the next section this scenario requests an important update of the usual energy delivery and management systems.
The second fundamental feature of renewable sources is the fact that other

than further to be de-localized over the space they also vary over time. The main example is solar energy which is present during daytime (furthermore with a variable power depending on the sky conditions) but not at night. All renewables present this feature that normally implies a mismatch between energy availability and demand. For this reason some sort of energy storage is needed and efforts are due to develop new technologies and infrastructures. This topic is furthermore related to the transport sector which necessarily implies some kind of energy storage. The mainstreams are biofuels and batteries but research is also looking for new solutions e.g. fuel cells and new hydrogen technologies.

Finally some important parameters regarding renewable technologies have to be taken into account. These are the so-called Energy Payback, the Lifetime, and the Life Cycle Assessment (LCA). The first consists in the time needed, for a technology, in order to generate the same amount of energy required for its manufacture. This is normally compared with the second index, the Lifetime, since from their ratio one evaluates how many times the technology returns the energetic investment needed to its development. The latter is instead the determination of the overall environmental cost related to an energy source, from the raw material to the disposal. All these parameters have to be considered in order to evaluate energetically, environmentally, and economically the impact of an energetic source. An overview on this topic can be found in [18].

To conclude, it is clear that renewables have the potential to solve the current critical energetic situation leading to a sustainable way to harvest energy for our needs. Although important actions and huge economical efforts are due in order to develop the necessary technologies for a wide diffusion of this kind of sources. Investment in renewables field are greatly increasing over the last years but it is difficult to anticipate if they will be sufficient to facing the problem. For sure a reduction of the western countries energy demand is also needed to make the goal more achievable. The next section will be focused on this topic.

1.2.2 Energetic Efficiency

The improvement of the energetic efficiency in the whole energy market should guarantee a better usage of energy, leading in the near future to a decrease in the consumptions and costs. In this picture the expected enormous increase of the energy demand, mentioned in section 1.1 would be shortened with beneficial effects.
An effective increase of the energy savings should involve all of the three main sectors of energy: production, distribution and utilization. The words "production" and "distribution" basically refer to energy under the form of electricity which is produced from fossil fuels, or different sources as in the case of renewables. Instead "utilization" comprises the three main sectors of energy consumption: industrial, home and transport.

Production: nowadays the main way to produce electricity consists in the combustion of fuel, which transforms its chemical energy into heat, causing the expansion of a fluid and then the rotation of a turbine connected to an electric alternator. This chain of energy transformations (chemical - thermal - mechanical - electrical) represents $\approx 63\%$ of the electric energy production in the world and the $\approx 42\%$ in EU [3]. An improvement of its conversion efficiency would lead to an huge energy saving. Turbines are extremely efficient (up to 90%) thus the mechanical rotation is efficiently converted into electricity. However the overall transformation has a much lower efficiency. This is due to the fact the major part of the thermal energy generated in order to cause the fluid expansion cannot be converted by the system into electricity . Therefore an overall efficiency of ≈ 0.4 results.
The utilization of the so called co-generative (or combined heat and power, CHP) systems can greatly enhance this quantity. In this case the heat produced and not transformed into electricity is redirected and utilized for various purposes, as for example building heating or some productive/industrial steps which imply the utilization of heat. In this cases the efficiencies are subjected to a great enhancement, up to ≈ 0.8.
Co-generative systems have a great potential in terms of energy savings and they can be utilized for any kind of electricity production since in principle heat is always present as a secondary product.
However some constrains exist. The first is economic, as co-generative sys-

tems are in fact large capital investments. Therefore companies have to start significant economic investments with not immediate returns. Secondly since co-generative systems are normally able to produce supplemental power (beyond the needs of their loads) they should be interconnected with the existing grid. Thus co-generative systems have to be coupled with both electrical and heating grids in order to perform their great energy saving potential.
However CHP has expanded a lot during the first decade of this century . For example in Europe where the co-generation has reached nearly the 12% of the total electricity production in 2010 under the promotion of the so called CHP directive of the European community.

Distribution: regarding this sector an improvement of the electricity distribution efficiency can be achieved following the so called smart grid concept. In fact one of the major issues in the present energy market is the relationship between the old system of centralized electricity production and the novel concept of distributed micro-production. Actually the present electricity delivery system was realized as "passive", namely capable of unidirectional delivery only, from the high to the low voltage and then to the final users. The recent increase of small productive unities has changed this scenario. The delivery system in this context should be able to answer as a whole, directing electricity where there is a need in a given moment. This should happen in any directions, even from low to high voltage, behaving then as a smart grid.
The development of a smart delivery system needs many infrastructures and advanced technologies that will request time and investments to become reality. In Europe since 2002, 459 smart grids project were launched with a total investment of to 3.15 billion of euros invested [19].

Utilization: as already mentioned the three main energy user sectors are: industrial, home and transport. Any of these requests approximately one third of the total primary energy demand of a given country.

Regarding industries an improvement of the energetic efficiency resides basically requires improved production processes. The complexity of this topic is due to the fact that any process should be evaluated and improved

case by case. However in general a contraction of the industrial energy demand can be achieved by a systematic reduction of their losses. Typically the processes manly subjected to energetic losses are those including steam, vapour, or in general involving heat. The simple improvement of the thermal isolation and a better redirection of extra heat fluxes toward production steps where heat is needed in order to further increase energetic efficiency. Regarding this case one method to evaluate the thermal efficiency of a given industrial process were developed by the University of Manchester [20]. This method called Pinch Analysis were successfully implemented in several industrial setups. Other more complex and expensive strategies are based on combined cycles or different technologies which imply a reorganization of the production processes.
In Europe the industry energetic efficiency is promoted in the picture of the project ODYSSEE-MURE which also aims at monitoring several industrial fields progress through the so called ODEX index [21]. This value is based on the evaluation of the "energetic consumption unit" which is basically the energy consumption needed for the realization of a ton of a given product [21].

Regarding the home sector the energy demand comes generally from two principal needs: electricity and heating.
For the former an improvement of the efficiency can be achieved by the use of more efficient final loads. A diffuse use of high class appliances and low consumption light lamps are the best way for a reduction of the electricity demand. For this reason political and economical actions towards a higher diffusion of such technologies is needed.
For the latter the main strategy consists instead in a better building thermal insulation. While at least in EU a great political activity has been develop in this direction for new constructions, e.g. with the introduction of laws defining energetic efficiency classes, less effort has been devoted to existing buildings. Citizens are not sufficiently motivated to invest efforts and money in the energetic efficiency of their own properties. Normally the high costs related to an enhancement of the building insulation limits the diffusion of this practice. However considering the huge potential of this sector in therms of energy savings, new professional figures are diffusing. Examples are Energy Managers and Energy Service Companies

(ESCO), born in order to technologically and economically sustain private and industrial users towards a better energy use [22].

Regarding the transport sector the discussion will be addressed in section 1.3.1 where this topic would be fully discussed in the picture of thermoelectric heat recovery.

1.3 The thermoelectric opportunity

As it will be fully illustrate in the next chapter, thermoelectric devices or generators (TEGs) are solid state heat engines capable of converting heat into electricity (or vice versa), in the presence of a difference of temperature (they operate between an hot and cold junctions) without any moving parts. Thermoelectric effect has been successfully implemented since its discovery for temperature sensing in thermocouples, which remains nowadays their wider application. Other present uses are instead confined in some very narrow niches, e.g. portable fridge cooling and power source for deep space missions. Only recently, especially with the advent of nanotechnology, thermoelectric devices have been indicated as candidate for bulk applications field. In this context during the last decade several papers about the present and future thermoelectric potential appeared in literature. A suitable resume of this scientific debate is available in two commentaries appeared in Nature Materials [4, 23] between 2009 and 2011. The main points of the positions reported by the authors are summarized in Fig.1.5(a) and (b).
In Fig.1.5(a) a comparison between the efficiency of several heat-electricity conversion technologies and thermoelectrics is reported. Thermoelectric efficiencies are based on the so called adimensional figure of merit, that will be described in the next chapter, and that are labelled in function of their applicability as: available (ZT = 0.7), plausible (ZT = 2), ambitious (ZT = 4) and unlikely (ZT = 20). From this picture it is clear how the existing mechanical systems are far more efficient than thermoelectrics. Furthermore this situation seems reasonably stable and will remain so also in the future.
This point of view it has been used to state that thermoelectric converters unlikely will contribute to face the energetic problem [4].

Even though, Fig.1.5(b) reports a different feature which seems to mitigate these statement. In fact the graph (which is just illustrative) shows a comparison of the efficiency versus size for thermoelectrics and mechanical engines. As shown the thermoelectric case result more efficient below some power level as mechanical engines, are known to become worst scaling down in size. This consideration open the way, at least for small power applications, to thermoelectrics.
Furthermore it has been recently shown by Kraemer and colleagues [24] that using suitable and relatively simple thermal concentration technologies coupled with thermoelectric devices, it would be possible to achieve efficiencies comparable with those available from non concentrating solar cells [23]. This evidence indicates thermoelectric devices as candidate to play a role also in the future energy harvesting field.
Finally it should be pointed out that since thermoelectric systems are capable of generating electrical currents even with small gradients of temperature, they represent one of the few options to recover low enthalpy heat. Furthermore considering that thermoelectrics are basically the only present technology with these characteristics that also do not need moving parts one may expect them to impact in many heat recovery and micro-harvesting applications.

Therefore thermoelectric devices are basically promising for at least

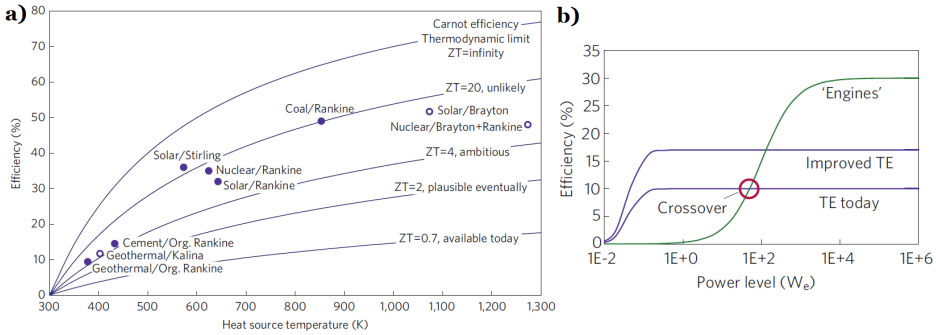

Figure 1.5: a) Comparison between efficiencies of several heat-electricity conversion technologies and thermoelectric; b) Illustrative plot of efficiency versus size for the two cases of Fig.(a). Reproduced with permission from [4].

two energy related fields: waste heat recovery and micro-harvesting from one hand, and bulk energy harvesting on the other.

1.3.1 Energy recycling: Waste recovery and Micro-harvesting

This field of thermoelectric applications is strictly related with the energy efficiency (1.2.2). In fact the main purpose is to recover wasted heat (or harvest it from any kind of source) at temperatures at which it cannot be recovered (or harvested) by conventional engines and/or in situations where it cannot be transformed in mechanical energy.
At the actual state of the art two applications attract the largest interest, namely car engines heat recovery and human body micro-harvesting.

Car Engines Heat Recovery: it is well know that nearly 60% of the chemical energy in fuels used by conventional automotive is lost as heat. Part of this large amount of lost power could be converted into electricity using thermoelectric devices. Recently BMW group reported, during the 2nd Thermoelectrics Applications Workshop, that in the case of a BMW (535i, NEDC) engine an average of 0.45 kW of thermal power is available [25]. This is equivalent to an estimated average fuel savings of 0.4-0.5 litre every 100 km, and a significant reduction of the CO_2 emission. However some limitations and difficulties arise in this picture. In fact firstly it should be noted that being the amount of wasted heat a fraction of the actual engine power, it is also a function of the car speed (or better the engine revolutions per minute) which furthermore changes the muffler temperature (where normally the device hot junction is placed) and then influence the conversion efficiency. Therefore both recoverable heat and efficiency are functions of the car velocity and this impact negatively on the device engineering and optimization. In addition, keeping a constant low temperature at the thermoelectric cold junction is difficult as it tends to increase towards the temperature of the hot side, (decreasing the efficiency).

Human Body Micro-harvesting: one of the prominent modern trend in commercial electronics is wearable devices with autonomous operation,

which do not need wire charge or frequent battery recharge and replace. Self-rechargeable devices, namely electronics able to harvest sufficient energy in order to recharge themselves, or at least to increase their operative time, would open new markets. Therefore it is not be surprising that many research projects and investigations have grown around thermoelectric micro-harvesting in the last few years. The human body seems the perfect candidate as thermoelectric heat source considering that it acts a thermal reservoir set at a temperature around 37 °C (inner body temperature). It was calculated that a person at rest releases a power density of 7 mW/cm^2. However considering the heat dissipated by sweat that cannot be recovered by a TEG the previous estimation decreases to 5 mW/cm^2 [26]. Power densities can anyway increased implementing dissipation systems,capable of dissipations up to values between 15-25 mW/cm^2 identified as the range for which the sensation of cold become to be uncomfortable [26]. Therefore assuming a heat flow of 20 mW/cm^2 with a standard thermoelectric module (ZT=1) operating between 34 (which is the skin temperature) and 22°C (room temperature), then with a ΔT of 12°C, one would estimate a harvested power density up to 180 $\mu W/cm^2$. This power output would be of commercial interest, at least for some kind of applications in the field of health monitoring sensors [27, 28]. However it was clearly shown [26] that the actual amount of power that can be harvested from the human body is cut by some constrains down to values around 25-31 $\mu W/cm^2$. The reason behind such a huge decrease comes from the fact that the actual temperature difference is much smaller than the 12 degrees considered and it do not exceeds 6 °C. This is due to the difficulty of guaranteeing large heat dissipations with the environment, which binds the heat flux and then temperature difference. In fact since a matching between the thermal resistances of the human body and the thermoelectric devices are needed, and considering that this quantity for the body is very high [29, 30], it is necessary to consider a high thermal resistance also for the TEG. But this controversially impact negatively on the heat dissipation.

Although these difficulties, the field of thermoelectric energy harvesting from human body is an increasing sector of thermoelectric research, which collects increasing interests and funding.

1.3.2 Energy Harvesting

The application that seems to attract most part of the interest for thermoelectrics in the field of energy harvesting, is solar energy. Many types of devices and systems have been proposed so far in literature, widely belonging to two classes: Hybrid Solar-ThermoElectric (HSTEG), and pure ThermoElectric (STEG).
In the first class systems differentiate depending (i) on the role of the thermoelectric part, which can be used for cooling [31] or electric production [32, 33, 34, 35]; and (ii) on which strategies are developed to transmit the heat to the thermoelectric hot junction, either by heat conduction, or directly splitting the incoming solar input [36].
In the second class, systems are classified depending on the kind of solar power concentration developed, which is mandatory to reach temperatures high enough to guarantee competitive efficiencies. Among the various approaches proposed, the most promising seem, as already mentioned, those reported by Kreamer and colleagues [24]. The system consists in a vacuum stage in which a flat metallic panel absorbs and concentrates solar radiation on the hot junction of a thermoelectric couple. Being a system for which the solar concentration is thermal and not optical it does not need tracking technologies which would impact negatively on the final device costs. The authors report a peak efficiency around 5% which promise to be competitive with other solar technologies under development.
However the need of a vacuum stage seems to be a strong limitation for a large diffusion of this kind of devices.
In this thesis some analysis were developed on hybrid thermoelectric-photovoltaics systems (HTEPV), namely TEGs coupled with PV cells, as corollary to the main activity (App. A).

Chapter 2

Theory Background

In this chapter the basics of thermoelectricity and the relevant material properties for this field will be introduced.
Starting from the description of the thermoelectric effects and the thermodynamics regarding conversion devices, it will be introduced the concept of thermoelectric efficiency and figure of merit which are useful tools to classify materials.
This will be necessarily supported by an introduction on the electrical and thermal properties of solids, considering firstly the bulk and secondly the nanostructured case.
Furthermore the field state of the art will be analysed focusing the discussion on some relevant topics, as the material crustal abundance and technological drawbacks for nanotechnologically designed devices.
Finally the thermoelectric and transport properties of silicon, which is the topic of this thesis will be described, to support the motivations to this PhD work.

2.1 Thermoelectric Effects

The absolute Seebeck effect is the spontaneous generation of an electrical potential within any isolated material subjected to a temperature gradient. This effect is defined in the open circuit configuration, hence is independent of any current flow. This definition implies that the absolute Seebeck effect is different and non influenced from the others thermoelectric phenomena namely the Peltier and the Thomson effects. Both of these in fact are present only when an electrical current flows within the material. Then in this context it is possible to define the Seebeck coefficient of a given material as the derivative of the electrical potential with respect to the temperature for a given temperature T:

$$\alpha(T) = \left[\frac{\mathrm{d}V}{\mathrm{d}T}\right] \tag{2.1}$$

The Seebeck coefficient can be positive or negative depending on the sign of the material majority carriers. Thus in the case of a p-type semiconductor, $\alpha(T)$ would be positive, and negative for a n-type material. When a junction of two different materials (namely a thermocouple) is formed, the resulting voltage is just due to the difference between the internal Seebeck potentials and is not affected by the external contact potential (the Volta effect). Basically it is possible to consider thermoelectric circuits as energy converts. In fact they can convert thermal energy into electrical energy. The most diffused application of the Seebeck effect is in thermoelectric thermometry, based typically on the utilization of thermocouple composed by two different and well characterized materials.
As already mentioned two other thermoelectric phenomena are instead caused by the flow of an electrical current. In particular, Peltier effect could be defined as the reversible change in heat at the interface between two different materials, caused by the change in the entropy of an electrical charge. Also in this case is possible to define a Peltier coefficient proportional to the ratio between the heat generated or absorbed per unit time and the electrical current:

$$\pi = \frac{\mathrm{d}Q_p/\mathrm{d}t}{I} \tag{2.2}$$

At last a reversible change of the heat content can be registered also within

a single material subjected to a temperature gradient when a electrical current passes within it. This third phenomenon is called Thomson effect for which is possible to define a coefficient τ by the following equation:

$$\frac{\mathrm{d}Q_t}{\mathrm{d}t} = -\tau J \frac{\mathrm{d}T}{\mathrm{d}x} \tag{2.3}$$

The relation between the three effect could be understood by the Kelvin equations which correlate the three mentioned coefficients:

$$\pi = \alpha T \tag{2.4}$$

$$\tau = \frac{\mathrm{d}\alpha}{\mathrm{d}T} T \tag{2.5}$$

This thesis were devoted to the study and the characterization of just one of the mentioned thermoelectric phenomena, namely the Seebeck effect and its applications into the energy field. In fact thermoelectric devices can be implemented in order to convert heat into electricity for energy harvesting and heat recovery.

2.2 Thermoelectric devices and conversion efficiency

A thermoelectric generator (TEG) device can generally be defined as an electric circuit or system, which can convert, with efficiency η, thermal power into electrical power. A part from the details of the device geometry the standard thermoelectric circuit is composed by a number of junctions between two thermoelectric materials, one with $\alpha(T)$ positive and the other with $\alpha(T)$ negative. The two elements are connected, typically by the utilization of a third conducting material, electrically in series and thermally in parallel (Fig. 2.1a). However the thermodynamics of the thermoelectric energy conversion do not prevent the realization of a circuit made with just one thermoelectric element as reported in Fig. 2.1b. In the following paragraph the thermodynamics of a thermoelectric generator will be discussed in order to find the conversion efficiency.

2.2.1 Conversion efficiency of thermoelectric devices

Consider the device reported in Fig. 2.1a, and suppose also that the heat source supplies the system so as to maintain a difference of temperature $\Delta T = T_{\mathrm{H}} - T_{\mathrm{C}}$, between the hot and the cold side. Furthermore lets take into account the case in which a load of resistance R_L is connected to the device, assuming no variation of the materials properties (e.g. Seebeck coefficient, thermal conductivity, electrical conductivity) in the range of temperature between T_{H} and T_{C}.
Therefore, the conversion efficiency η is simply the ratio between the electrical output power produced by the TEG:

$$W = \left[\frac{(\alpha_{\mathrm{p}} - \alpha_{\mathrm{n}})\,\Delta T}{R_{\mathrm{L}} + R_{\mathrm{p}} + R_{\mathrm{n}}}\right]^2 R_{\mathrm{L}} \tag{2.6}$$

and heat flow rate entering from the hot side:

$$\frac{\mathrm{d}Q}{\mathrm{d}t} = (K_{\mathrm{p}} + K_{\mathrm{n}})\,\Delta T + (\alpha_{\mathrm{p}} - \alpha_{\mathrm{n}})\,I T_{\mathrm{h}} - I^2 R/2 \tag{2.7}$$

In Eq. 2.6, α_{p} and α_{n} are respectively the Seebeck coefficient of the p and n materials, while R_{p} and R_{n} are the electrical resistance of the two legs. In Eq. 2.7 instead, K_{p} and K_{n} are their thermal conductance and

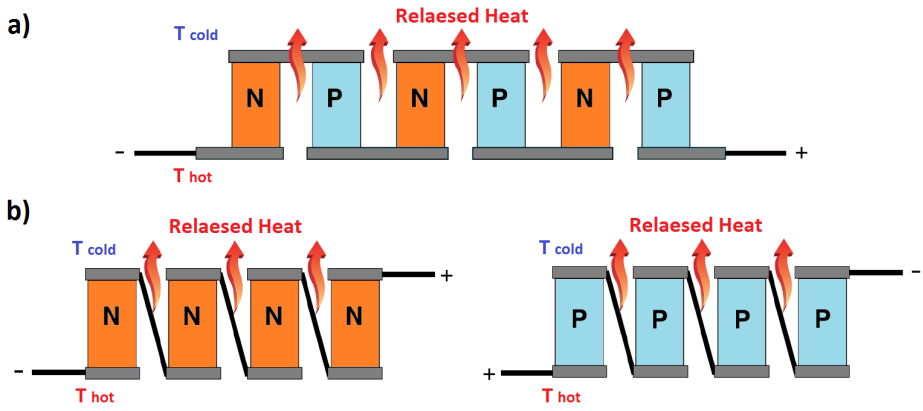

Figure 2.1: a) Schematics of an usual thermoelectric device with two different kind of legs, one made by a p-type and the second by a n-type material; b) Schematics of two different thermoelectric material for which just one kind of leg is implemented.

I is the electrical current. Following Ioffe [37] it is possible to optimize the TEG performances over the parameter $m = R_{\mathrm{L}}/\left(R_{\mathrm{p}} + R_{\mathrm{n}}\right)$ in two different ways. The first, for $m = 1$, maximize the output power W and returns a device efficiency

$$\eta_{\mathrm{W}} = \frac{1}{2}\eta_{\mathrm{C}}\left(1 + \frac{2}{Z_{12}T_{\mathrm{H}}} - \frac{\Delta T}{4T_{\mathrm{H}}}\right)^{-1} \tag{2.8}$$

with $\eta_{\mathrm{C}} = 1 - \frac{T_{\mathrm{C}}}{T_{\mathrm{H}}}$ and Z_{12} defined as the system figure of merit given by

$$Z_{12} = \frac{\left(\alpha_{\mathrm{p}} - \alpha_{\mathrm{n}}\right)^2}{\left(\sqrt{\rho_{\mathrm{p}}\kappa_{\mathrm{p}}} + \sqrt{\rho_{\mathrm{n}}\kappa_{\mathrm{n}}}\right)^2} \tag{2.9}$$

where ρ_{p} and κ_{p} are respectively the electrical resistivity and the thermal conductivity of the p leg, and ρ_{n} and κ_{n} are the same quantities for the n leg. As an alternative one can maximize the conversion efficiency by imposing a value of m which satisfies $\partial\eta_{\mathrm{TEG}}/\partial m{=}0$, which returns $m = \sqrt{\left(1 + Z_{12}T_{\mathrm{M}}\right)}$ (where $T_{\mathrm{M}} = \left(T_{\mathrm{H}} + T_{\mathrm{C}}\right)/2$) and gives

$$\eta_{\mathrm{TEG}} = \eta_{\mathrm{C}}\frac{\sqrt{1 + Z_{12}T_{\mathrm{M}}} - 1}{\sqrt{1 + Z_{12}T_{\mathrm{M}}} + T_{\mathrm{C}}/T_{\mathrm{H}}} \tag{2.10}$$

From the comparison between Eqs. 2.8 and 2.10 it is immediate to understand that $\eta_{\mathrm{W}} \leq \eta_{\mathrm{TEG}}$. In spite these considerations, the highest device conversion efficiency is not always the best solution, as recently pointed out by Narducci [38], especially when constant input heat flux is present. However in both equation the figure of merit Z_{12} plays a key role for the optimization of the device performances.
The figure of merit for a single thermoelectric material can be defined as

$$Z = \frac{\alpha^2\sigma}{\kappa} \tag{2.11}$$

where σ is the material electrical conductivity. The numerator of Eq. 2.11 is also called power factor PF which is related to the output power as

$$W = PF\frac{\Delta T^2}{\left(R + 2\right)l/S + R_{\mathrm{L}}} \tag{2.12}$$

where R is the material electrical resistance, l and S the length and the section of the thermoelectric element.
The maximization of these two parameters, the figure of merit and the power factor, has defined the two main streams on which the research thermoelectric community has focused onto in the last decades. Before discussing on the methods devoted to the modulation of these parameters is useful to introduce the basics of solid state physics which governs the material properties.

2.3 Electric and Thermal transport in solids

Since thermoelectric energy conversion is necessarily related to electric and heat transport, it is necessary to focus the discussion on the transport in solids. To do that it will be introduced the relaxation time approximation within the context of the Boltzmann Transport Equation (BTE), which is widely used to this scope. In this picture it will be possible to deepen the understanding of the electrical and thermal transport in solids and consequently the scattering mechanism.

2.3.1 Semiconductors, metals, and carriers transport

The electrical transport in a solid is due to the quasi-free electrons of its atoms. The term quasi-free, comes from a proper correction of the free electron model proposed by Drude and Lorentz in the early twentieth century. In this model the valence electrons are considered as a free electron gas, non interacting with the remaining ions of the crystalline lattice. Although several metals properties as the thermal capacity, the electrical conductivity and the magnetic susceptibility are well described by this model, other important features e.g. the difference between metals, semiconductors and insulator and other properties cannot be understand within this picture. This problem is overcome considering a small interaction between the ions and the valence electrons, hence taking the case of a free electron gas perturbed by a periodic potential. This perturbation defines the allowed and forbidden energies, and sets up allowed energy bands divided by forbidden region (energy gaps). Fig. 2.2 reports how different band occupations lead the solids to behave as metals, semiconductors or

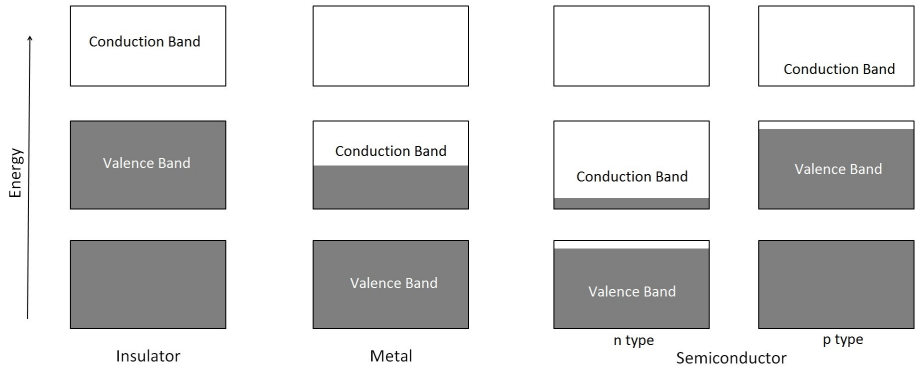

Figure 2.2: Schematics of bands occupation in the case of insulator, metal and semiconductor

insulators. For the semiconductor case the two possibilities, hence electrons (n type) and holes (p type) transport are showed. For simplicity the discussion will refer only to the n type case.

Within the picture of the Pauli exclusion principle, the electrons in the solid occupy the bands following, the Fermi-Dirac (FD) distribution

$$f_0(E) = \left[\exp\left(\frac{E-\mu}{k_B T}\right) + 1\right]^{-1} \tag{2.13}$$

where μ is a function of the temperature called chemical potential, corresponding to the energy for which $f_0(E) = \frac{1}{2}$. The FD distribution is equal to unity when $(E-\mu) \ll kT$ and equal to zero when $(E-\mu) \gg kT$, therefore its represents the probability for the level with energy E to be occupied. The transition between unity and zero, for $f_0(E)$, takes place within a range of energies large as $\approx 2kT$, therefore at absolute zero FD changes abruptly when $E = \mu = E_{\mathrm{F}}$. E_{F} is called the Fermi energy and is defined as the energy of the chemical potential at T=0 K. Now defining $g(E)$ the electron density of states, namely the number of states per volume unit in the energy range between E and $E + dE$, it is possible to find the total number of electrons as

$$n = \int_0^\infty f_0(E) g(E) dE \tag{2.14}$$

The density of states is small near the conduction band edge, but increases rapidly with E. For a 3D material $g(E)$ is given by the expression

$$g(E) = \frac{V}{2\pi^2}\left(\frac{2m^*}{\hbar^2}\right)^{3/2} E^{1/2} \tag{2.15}$$

where m^* is the effective mass, namely the apparent mass with which the electrons respond to an external force. From equation 2.14 it is possible to find an expression for the current density j as

$$j = \mp \int_0^\infty ev(E)f(E)g(E)dE \tag{2.16}$$

where the sign in front to the integral depends on the carrier sign, and e is the electron charge.

Now, supposing an event (e.g. a scattering mechanism), perturbing the carriers distribution from its equilibrium value f_0, it can be assumed that f will relax according with

$$\frac{\mathrm{d}f(E)}{\mathrm{d}t} = -\frac{f(E) - f_0(E)}{\tau} \tag{2.17}$$

where τ is the relaxion time. In this picture, the Boltzmann transport equation (BTE) relates the effects of any applied field, with the carrier scattering.
For small perturbations, it can be written

$$\frac{f(E) - f_0(E)}{\tau} = v_x \frac{\mathrm{d}f_0(E)}{\mathrm{d}E}\left(\frac{\mathrm{d}E_F}{\mathrm{d}x} + \frac{E - E_F}{T}\frac{\mathrm{d}T}{\mathrm{d}x}\right) \tag{2.18}$$

where a unidimensional flow of carriers (along x) with velocity v_x was considered, in the presence of an applied electric field ($\varepsilon = \frac{1}{e}\frac{\mathrm{d}E_F}{\mathrm{d}x}$) and a temperature gradient. Using 2.18 and the 2.16, and considering that it is possible to replace f by $(f - f_0)$, because there is no flow of carriers for $f = f_0$ it follows

$$j = \mp \int_0^\infty e\tau v(E)_x^2 \frac{\mathrm{d}f_0(E)}{\mathrm{d}E}\left(\frac{\mathrm{d}E_F}{\mathrm{d}x} + \frac{E - E_F}{T}\frac{\mathrm{d}T}{\mathrm{d}x}\right) g(E)dE \tag{2.19}$$

Then it is possible to write an equation for the electrical conductivity, given by the ratio between the current density and the electric field when $\frac{dT}{dx} = 0$, obtaining

$$\sigma = -e^2 \int_0^\infty \tau v_x^2 \frac{\mathrm{d}f_0(E)}{\mathrm{d}E} g(E)\mathrm{d}E \tag{2.20}$$

Similarly from the ratio between the electric field and the temperature gradient, when $j = 0$ an equation for the Seebeck coefficient can be obtained

$$\alpha = \pm\frac{1}{e}\frac{e^2 \int_0^\infty \tau v_x^2 \frac{E-E_F}{T} \frac{\mathrm{d}f_0(E)}{\mathrm{d}E} g(E)\mathrm{d}E}{e^2 \int_0^\infty \tau v_x^2 \frac{\mathrm{d}f_0(E)}{\mathrm{d}E} g(E)\mathrm{d}E} \tag{2.21}$$

In both equations for σ and α, it is possible to introduce the carrier mean free path MFP ($l = v_x\tau$), namely the average distance between two scattering events is used. This topic will be further discussed in paragraph 2.3.3.

Following Shakouri [39] one may simplify equations 2.20 and 2.21, introducing the differential conductivity

$$\sigma(E) = e^2 \tau v_x^2 g(E) \frac{\mathrm{d}f_0(E)}{\mathrm{d}E} \tag{2.22}$$

which represents essentially the contribution of carriers with energy E to the overall electrical conductivity, to give

$$\sigma = -\int_0^\infty \sigma(E)\mathrm{d}E \tag{2.23}$$

$$\alpha = \pm\frac{1}{eT}\frac{\int_0^\infty \sigma(E)(E - E_F)\mathrm{d}E}{\int_0^\infty \sigma(E)\mathrm{d}E} \tag{2.24}$$

In Eq. 2.22, $\frac{\mathrm{d}f_0(E)}{\mathrm{d}E}$ is often called the Fermi window factor, which is a bell shaped function $\approx 2kT$ wide, centred in E_F. From equations 2.23 and 2.24, it can be easily understood that in order to have a high electrical conductivity, a material should have high values of $g(E)$ within the Fermi window; while it should exhibit the highest asymmetry for $\sigma(E)$ (hence a higher mean energy per carrier) within the same range of energies, to show

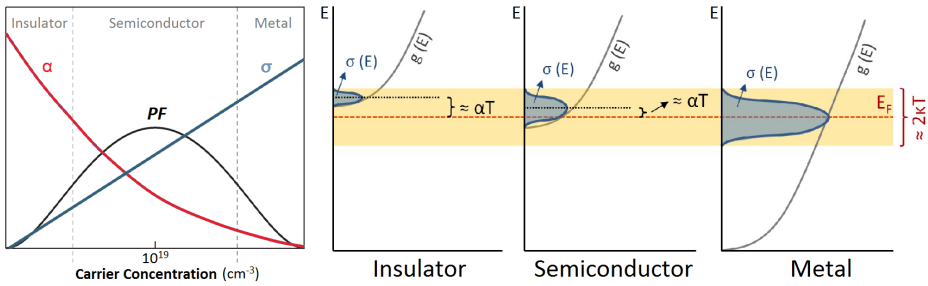

Figure 2.3: a) Trade off between electrical conductivity and Seebeck coefficient for bulk materials along carrier density; b) Schematics of electrical conductivity, Seebeck coefficient and density of state relationship for the three limit cases of insulator, semiconductor and metal.

high Seebeck coefficient. These considerations are the appropriate tools, in order to understand the behaviour of the PF (Eq. 2.12) as a function of the material carrier density. This trend will be reported, in the case of bulk materials in Figure 2.3 a. As showed within the graph, there is a trade off between the electrical conductivity and the Seebeck coefficient, for varying carrier densities. The origin of this behaviour is sketched in figure 2.3 b, where the three limiting cases of insulators, semiconductors and metals, are reported. For the metals case, a high electrical conductivity is present because of the large number of electrons available within the Fermi window. Instead the Seebeck coefficient is necessarily low because $g(E)$ is almost constant around the mean energy for carriers results very similar to E_F. The insulators case is instead clearly the opposite, with a very low electrical conductivity and a steeply change $g(E)$ at E_F. At last, the semiconductors case has intermediate behaviour, where it is possible to obtain the maximum value of PF.

2.3.2 Thermal transport and Phonons

Thermal transport in solids, at microscopic level, results from two main contributions: charge carriers and lattice vibrations. From this simple consideration it follows that the macroscopic thermal conductivity κ, is

basically the sum of two components[1]

$$\kappa = \kappa_e + \kappa_l \tag{2.25}$$

where κ_e and κ_l are respectively the electronic and the lattice contributions.

Regarding the electronic, its main features of this contribution are comprehensible within the picture of the free electron gas model. Consequently the behaviour of κ_e versus T is correctly described by the Wiedemann-Franz law

$$\kappa_e = \sigma L T \tag{2.26}$$

where L is the Lorentz number, with value of ≈2.4 x 10^{-8} J^2/K^2C^2 for metals and degenerate semiconductors, which are materials well described by the free electron model. Nevertheless the Lorentz number can vary with the doping as showed by Kumar et al. [40].

For the lattice contribution to the thermal conductivity one should recall that the quantised vibrations of the crystal lattice, called phonons, belong to the boson particle family, since for a given wave vector $\vec{K}$, their average amount is described by the Bose-Einstein distribution (BE)

$$n^0_{\vec{K}} = \left[\exp\left(\frac{\hbar\omega_{\vec{K}}}{k_B T}\right) - 1\right]^{-1} \tag{2.27}$$

with $\omega_{\vec{K}}$ the phonon angular frequency. Each mode transports $n^0_{\vec{K}}$ quanta of energy $\hbar\omega_{\vec{K}}$, so that the total mode vibrational energy is

$$E = \sum_{\vec{K}} n^0_{\vec{K}} \hbar\omega_{\vec{K}} \tag{2.28}$$

Also for phonons it is useful to introduce the density of states $\mathfrak{D}(\omega)$, which in this case represents number of vibrational modes in the frequency

[1] this discussion neglects the bipolar contribution κ_{bi}, which basically consists in the heat generated by the hole-electron annihilation, occurring normally within materials in which both types of electrical carriers are present (partially compensated materials).

range $[\omega,\ \omega + \mathrm{d}\omega]$. For the three-dimensional case, assuming isotropic dispersion properties can be demonstrate that

$$\mathfrak{D}(\omega)\mathrm{d}\omega = \frac{\mathrm{d}\vec{K}}{(2\pi/L)^3} = \frac{VK^2(\omega)\mathrm{d}K}{2\pi^2} \quad , \quad \mathfrak{D}_p(\omega) = \frac{VK^2(\omega)g_p}{2\pi^2 v_{g,p}(\omega)} \tag{2.29}$$

where $v_{g,p} = \mathrm{d}\omega/\mathrm{d}K$, is the group velocity for the polarization p, and g_p is a factor that takes into account the mode degeneracy. For a crystal with x atoms per primitive cell, there are in fact $3x$ branches: $3x$-3 acoustic and 3 optical. Thus e.g. silicon and germanium, both with two atoms per primitive cell, have six branches, one longitudinal acoustic (LA), one longitudinal optic (LO), two transversal acoustic (TA) and two transversal optic (TO). Using 2.29, equation 2.28 can be rewritten as

$$E = V \sum_p \int_\omega \left[\frac{\hbar\omega_{\vec{K}}}{\exp\left(\frac{\hbar\omega_{\vec{K}}}{k_B T}\right) - 1} \right] \frac{K^2(\omega) g_p}{2\pi^2 v_{g,p}(\omega)} \tag{2.30}$$

Let suppose now to set up a temperature gradient along x. Is possible to express the heat flux in that direction by summing the product between the phonons energies and their velocities over all wave vectors and for every polarisation:

$$\vec{Q} = \sum_p \left[\sum_{\vec{K}} \vec{v}_g \hbar\omega_{\vec{K}} n_{\vec{K}} \right] \tag{2.31}$$

Using again the relaxation time approximation, it is possible to write the BTE for the phonons subjected to the thermal gradient as

$$\frac{n^0_{\vec{K}} - n_{\vec{K}}}{\tau_K} = -\left(\vec{v}_g \cdot \frac{\mathrm{d}T}{\mathrm{d}x} \right) \frac{\mathrm{d}n^0_{\vec{K}}}{\mathrm{d}T} \tag{2.32}$$

Replacing now, equation 2.32 into 2.31, and considering that $n_{\vec{K}}$ can be replaced by $(n_{\vec{K}} - n^0_{\vec{K}})$ because there is no flow of any kind when $(n_{\vec{K}} = n^0_{\vec{K}})$ it is possible to obtain

$$\vec{Q} = \sum_p \left[\sum_{\vec{K}} \hbar\omega_{\vec{K}} (v_g^2 cos^2\theta) \tau_K \frac{\mathrm{d}T}{\mathrm{d}x} \frac{\mathrm{d}n^0_{\vec{K}}}{\mathrm{d}T} \right] \tag{2.33}$$

with θ is the angle between v_g and x. From 2.33 it is possible then to write an equation for the lattice thermal conductivity

$$k_l = -\frac{\vec{Q}}{\mathrm{d}T/\mathrm{d}x} = \sum_p \left[\frac{1}{3} \sum_{\vec{K}} \hbar\omega_{\vec{K}} v_g^2 \tau_K \frac{\mathrm{d}n^0_{\vec{K}}}{\mathrm{d}T} \right] \tag{2.34}$$

Within the Debye approximation, which assumes linear relation between frequency and wave vector ($\omega = v_s K$), equation 2.34 can be simplified because the phonon velocities are the same for all the polarisations, and the summations can be replaced by an integral

$$k_l = \frac{1}{3} \int \hbar\omega v_s^2 \tau_K \frac{\mathrm{d}n^0_{\vec{K}}}{\mathrm{d}T} \mathfrak{D}(\omega) \mathrm{d}\omega \tag{2.35}$$

with density of states

$$\mathfrak{D}(\omega) = \frac{3\omega^2}{2\pi^2 v_s^2} \tag{2.36}$$

that leads, together with the derived BE distribution, to

$$k_l = \frac{1}{2\pi^2 v_s} \int_0^{\omega_D} \hbar\omega^3 \tau_K \frac{(\hbar\omega/k_B T^2)\exp(\hbar\omega/k_B T)}{[\exp(\hbar\omega/k_B T) - 1]^2} \tag{2.37}$$

where ω_D is the so called Debye frequency, acting as a cut-off frequency such that the total number of phonon modes is $3N$ (N is the atoms number).
Defining now the Debye temperature as $\Theta_D = \hbar\omega_D/k_B T$ and replacing $\hbar\omega/k_B T$ with x it follows

$$k_l = \frac{k_B}{2\pi^2 v_s} \left(\frac{k_B}{\hbar} \right) T^3 \int_0^{\Theta_D/T} \tau_K \frac{x^4 e^x}{(e^x - 1)^2} \mathrm{d}x \tag{2.38}$$

that can be written in the usual Debye form

$$k_l = \frac{1}{3} \int_0^{\Theta_D/T} C(x) v_s l(x) \mathrm{d}x \tag{2.39}$$

where were introduced, the phonon mean free path ($l(x) = v_s\tau_K$) and the differential heat capacity

$$C(x) = \frac{3k_B}{2\pi^2 v_s}\left(\frac{k_B}{\hbar}\right)T^3\frac{x^4e^x}{(e^x-1)^2}\mathrm{d}x \tag{2.40}$$

In this pictures the heat capacity, is proportional to T^3 for very low temperature (T << Θ), where only the acoustic modes with high wavelengths are excited. For T >> Θ instead, $C(x)$ approximates the classical value $3Nk_B$.
The temperatures of interest in thermoelectric applications are normally much higher than the Debye temperature, so that the lattice thermal conductivity is dominated by the mean free path

$$k_l = Nk_Bv_sl(x) \tag{2.41}$$

2.3.3 Scattering mechanisms

In the previous two paragraphs, it was shown how perturbations on the carriers and phonons distributions are described within the relaxation time approximation theory.
Perturbations of particles and waves distribution in solids, are caused by scattering mechanisms. This means particles interactions with typically two possible sources: other particles and waves, or solid imperfections. These interactions can modify the particles kinetic energy, and/or momentum, which modify in turn their contribution to the macroscopic physical properties of the solids. Without these events particles would cross the material following the external applied field (e.g. a temperature gradient). In this case the notion of electrical and thermal conductivity would then have little meaning, as the transport would be ballistic. This is what happens at very low temperatures, or in nanostructures, as it will reported later.

In this paragraph instead the possible sources of scattering will be resumed, for the two kinds of transport described previously, electrical (electrons and holes) and thermal (phonons), in a diffusive regime i.e. within the picture of the relxation time approximation.
Of course in a real solid, more than one kind of scattering mechanisms are

present. Each of them contribute to the overall perturbation, following the Matthiessen's rule

$$\frac{1}{\tau} = \sum_{i=0}^{n} \frac{1}{\tau_i} \tag{2.42}$$

where n kind of scattering mechanisms are supposed to contribute to set the overall relaxation time.

For both transport phenomena, scattering is basically of two types: with crystal imperfections and with phonons. The first take into account many different scattering sources including: external surfaces, point defects, dislocations, ionized impurity atoms, neutral impurity atoms, grain boundaries, second phases and precipitates. The second instead includes, normal and Umklapp phonon scattering.

Collision with solids imperfections are basically dependent on the nature of the imperfection itself. Dimension, shape, state of charge and density (hence the number of defects and their mutual distance) influence in a non trivial way the defect effect on the electrical and phonon transport.

Collisions with phonons are processes involving three particles. Such events must satisfy the energy and momentum conservation as reported by the following relations

$$\omega_1 + \omega_2 = \omega_3 \tag{2.43}$$

$$K_1 + K_2 = K_3 \tag{2.44}$$

$$K_1 + K_2 = K_3 + G \tag{2.45}$$

where ω and K are the pertinent particles frequencies and wave vectors. Eq. 2.44 represents the normal phonon scattering for which the sum of the two input wave vectors lead to a third vector which belongs to the same Brillouin zone. Eq. 2.45 represents instead the Umklapp mechanism which involves a vector (G) of the reciprocal lattice, since K_3 exceeds the first Brillouin zone.

2.4 State of the art in thermoelectric materials field

In this section it will be reported an overview regarding the state of the art for thermoelectric materials. First of all it will be discussed the bulk case, for which the relationship between efficiency and crustal abundance will be shown. Secondly the nanotechnology strategies used in this filed will be described, focusing the discussion on the carrier and phonon transport optimizations. At last it will be reported an overview on thermoelectric properties of silicon which is the topic of this thesis.

2.4.1 Overview

From Eqs. 2.10 and 2.11 is clear that in order to achieve high ZT values thermoelectric materials should exhibit good carriers transport along with bad thermal properties. This approach, normally called *phonon glass-electron crystal*, has opened in the last four decades several ways for the realization of materials with good thermoelectric properties. Regarding bulk materials three approaches are successfully implemented.
The first consists in the formation of rattling structures or the creation of point defects within the unit cell, in order to enhance the phonon scattering. This is the case of alloys with binary tellurides as Bi_2Te_3 [41, 42], Sb_2Te_3 [43], PbTe [44] and GeTe [45] and other chalcogenide compounds, or structures having large voids in the unit cell as clathrates and skutterudites ($CoSb_3$ and related compounds [46]).
The second strategy consists instead on the use of complex crystal structures in order to separate the electron crystal from the phonon glass, as in half-Heusler alloys (e.g. $Hf_{0.75}Zr_{0.25}NiSb$ [47]) or in thallium based alloys (e.g. Ag_9TlTe_5 [48]) and others (e.g. Zn_4Sb_3 [49]).
The third strategy uses multiphase composites, mixed in order to enhance the phonon scattering without affecting the carriers transport as in the Zintl compound (e.g. $Ca_xYb_{1x}Zn_2Sb_2$ [50]) or LAST compounds [51] (Lead Antimony Silver Telluride, e.g. $AgPb_mSbTe_{2+m}$).
Unfortunately most of the key elements constituting these materials are not abundant in the Earth's crust and furthermore some of them are toxic. For these reasons recently new approaches directed a part of the research efforts towards materials belonging to two classes of compounds: oxides

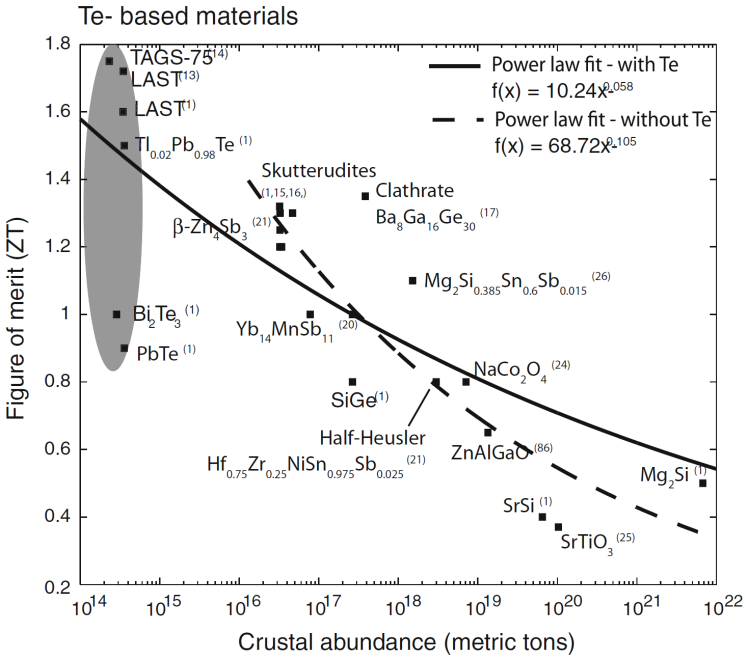

Figure 2.4: Relationship between ZT of the usual bulk thermoelectric materials and their abundance within the earth crust as reported in the study of Amatya. Reproduced with permission from [5].

and silicides. Some examples are $NaCo_2O_4$ [52], ZnO [53] and Mg_2Si [54, 55].

However, Amatya et al. [5] reported a study on the relationship between ZT and the materials crustal abundance, finding a negative power law as reported in Fig. 2.4. Although these evidences are expected to impact negatively on the possibility of a wide diffusion of thermoelectric devices, in the last decades nanotechnology opened new ways to break up this barrier. These strategies will be introduced in the following two paragraphs.

2.4.2 Nanostructures and modulation of materials properties

In 1993 two pioneering papers pointed out how dimensional constrains and the possibility to control materials at the nanoscale can be used to reach

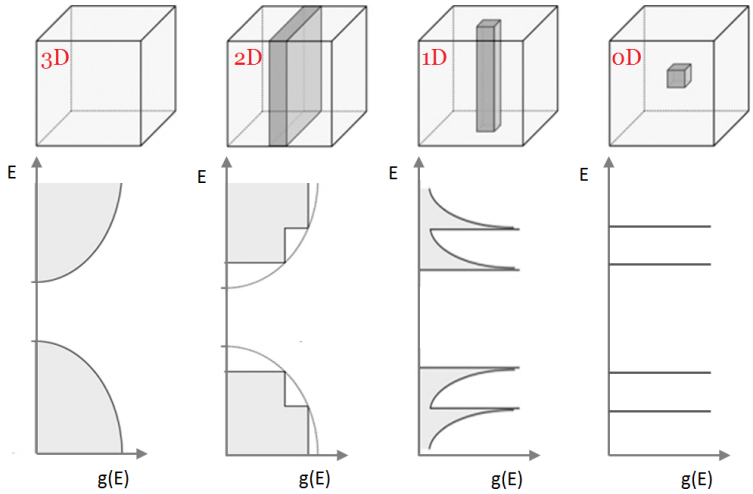

Figure 2.5: Pictorial view of the electronic density of states $g(E)$ for different dimensionality cases: 3D, 2D, 1D and 0D

better thermoelectric efficiencies compare to bulk materials. In that year, Dresselhaus and Hicks calculated the thermoelectric figure of merit firstly for the case of two dimensional Bi_2Te_3 [56] and secondly for a nanowire [57], showing a strong ZT enhancement upon decreasing the structure dimensions. These paper caused a proliferation of studies and works, focused on the optimization of the thermoelectric properties with appropriate nanostructures. Following the *phonon glass-electron crystal* idea the nanotechnology strategies will be described splitting it in two parts, the first focused on carriers and the second on phonons transport.

2.4.3 Carrier Transport Optimization

Nanostructures confine carriers wavefunction in one or more dimensions. Therefore the local density of states $g(E)$ becomes a sharp function of the electron energy as reported in Fig. 2.5. In particular for the 2D case $g(E)$ is a step function such that between any step $g(E) \propto cost$; for quantum wires instead $g(E) \approx E^{-\frac{1}{2}}$ exhibiting sharp maxima at the quantization energy; finally for the $0D$ case discrete energy peaks are present.

Referring our discussion to Eqs. 2.23 and 2.24 it is then easy to understand that such variation of $g(E)$ can alter PF. Furthermore the inverse monotone relationship between the Seebeck coefficient and the doping, also called Pisarenko law, reported in Fig. 2.3, is no longer valid. It is instead possible to act for proper doping optimization in order to maximize PF. In fact since the energy level is set essentially by the doping level, one can tune the dopant concentration in order to place E_F in a favourable position to maximize PF. These maximizing configurations are normally situated in the $g(E)$ peaks proximity or where a high $g(E)$ asymmetry exists.

Another option for PF optimization is carrier energy filtering, which consists in the introduction of proper potential barriers in the material matrix, which can selectively filter out the low energy carriers. The result is basically a strong asymmetric $\sigma(E)$ which means an increment of the mean energy per carrier, hence a higher Seebeck coefficient. This effect is reported in several computational and experimental works in which the barriers are normally set by a dispersion of metallic nano-inclusions [58, 59, 60, 61, 62]. Despite its apparent simplicity, energy filtering needs some conditions in order to occur. The first is that the barriers have to be non-planar but isotropic scattering centres, because planar barriers are acting as momentum filters instead than energy filters, as shown by Shakoury [63]. The second condition regards instead the distance among the barriers which has to be small enough to guarantee prevalence of ballistic carrier transport. Therefore carriers have not to relax between one barrier and the other. Finally the barrier height has to properly chosen in order to not suppress the electrical conductivity.

2.4.4 Phonon transport Optimization

The dimensional confinement discussed for carriers in the previous paragraph acts also on phonon transport. In this case as the structure boundaries are sources of phonon scattering, it is possible to confine or reduce the phonon transport along one or more dimensions. In particular structures whit sizes smaller than the bulk phonon MFP enhance the scattering, hence show smaller thermal conductivities. In literature this effect was well studied for the case of nanowires (NWs) [64, 65] for which ballistic

phonon transport was found, and monotone correlations between thermal conductivity and NW diameter was reported [66, 67, 68, 69]. Same behaviour was shown also for nanolayers (NLs) [70] namely thin films with very small thickness.

Similar effects are present in superlattices [71, 72, 73, 74], polycrystalline materials [75, 76] and two phases alloys[77, 78, 79] for which the boundaries between the different phases act as phonon scatters. Even though for these cases strong decreases of the thermal conductivity were reported depending upon phases sizes, a limit to this effect exists [80, 81, 82]. In particular it was show how in these cases scattering mechanism is effective just for some kind of phonons and ineffective for others. This is basically due to the fact that phonons are distributed along a wide spectrum of frequencies. For this reason phonons with wavelengths comparable or smaller that the phases dimension are well scattered, while phonons with higher wavelengths are unaffected and can efficiently conduce heat.
Same reasoning is valid in the case of scattering due to solid imperfections, like point defects, aggregates and nanovoids.

Based on this point of view, as recently reported in some reviews [83, 84], the best strategy in order to achieve low thermal conductivities, seems to act an hierarchical architecture of defects an structures which can selectively scatter different portions of the phonon spectrum. The sum of all scattering sources should led to an effect of confinement for all the phonons in the material.
However it should be highlighted that this hierarchical phonon scattering strategy has to be designed in order to act selectively only on phonon transport, without affecting electronic carrier flow. This can be done exploiting the difference between the phonon and the carrier MFPs.

2.4.5 Dimensionality drawbacks

Even thought nanostructuration opens plenty of opportunities to modulate the material properties, industrial and commercial devices based on nanostructures are basically infeasible. Even neglecting the issues regarding the scalability of the actual techniques normally implemented for the realization of these structures, some difficulties remain. These issues are

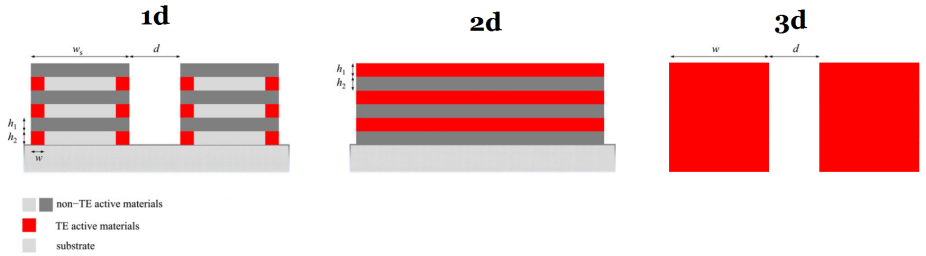

Figure 2.6: Schematics of the three device structures proposed within the text, with the quantities used to define the filling factor.

both physical and technological.

Physical problems concern the thermodynamic of thermoelectric conversion itself. In fact as reported in Sect. 2.2.1 in order to achieve better efficiencies, materials should exhibit very low thermal conductivities. This implies in terms of devices, very high thermal resistances which consequently means low power outputs, as can be seen from Eq. 2.12. In this picture these kind of devices would be very efficient but would generate very low electrical powers. Alternatively one may think to achieve higher powers creating devices which a very high numbers of legs placed in parallel. Unfortunately this approach hits with the second kind of problems that will be described.
Technological issues regard in fact the so called filling factor (ϕ) of devices, defined as the ratio between the total device and the thermoelectrically active volumes. In order to be implemented in a device, nanostructures are normally embedded, or at least grown on other materials, usually chosen to be electrically and thermally insulating. In Fig. 2.6 the case of NWs and NLs is reported compared with the bulk (3D) case. It is easy to understand that the filling factor for the 1D and the 2D cases are much lower compared with to 3D case. In fact while for bulk ϕ is near to unity, for the 1D case reported in Fig. 2.6 which is the higher packing configuration reported so far in literature[85], the filing factor is

$$\phi = \frac{2h_1 w}{(w_s + d)(h_1 + h_2)} \approx 0.14(^2) \tag{2.46}$$

[2]computed with the actual lithography resolution limit[85]

and for the 2D case

$$\phi = \frac{h_1}{h_1 + h_2} \approx 0.5([3]) \tag{2.47}$$

without substrate contribution (then considering self-standing structures) which the best desirable condition. These means that respectively ≈ 85 and $\approx 50\%$ of the device volume doesn't contribute to power generation but irremediably transmit heat from the hot to the cold side. Depending from the thermal resistance of the non thermoelectric fraction the device efficiency would be subjected to some decrement.
Considering the substrate contribution the situation worsens considerably. The filling factor decreases N times, with N the ratio between the substrate thickness and the overall thermoelectric active material thickness. NWs and NLs filling factors are expected to decrease a lot since their thickness is orders of magnitude lower than the substrate macroscopic thickness.
From these considerations it follows that nanostructures in thermoelecrtics should be considered mostly as a useful tool in order to study solutions which have to be translate into bulk in order to be of practical usefulness [86].

Different conclusions can be drawn instead for thin films[4]. In this case in fact h_1 can be much bigger than h_2, therefore Eq. 2.47 will return higher values for ϕ. For example considering $h_1 = 0.5$ μm and $h_2 = 50$ nm, $\phi = 0.91$. Furthermore also considering the substrate, higher filling factor are expected compared to the NWs and NLs cases, because of the higher N value.
This evidence collocates thin films in the middle between bulk and nano thermoelectric technologies.

2.4.6 Silicon as thermoelectric material

Because of its enormous abundance in the earth crust (second more abundant element, constituting $\approx 27.7\%$ in weight of the earth crust), silicon has always been an attractive material for several fields. Unfortunately

[3] values calculated for nanolayers [70]

[4] The difference between thin films and NLs is the typical different thickness of these structures. Are normally considered NLs, systems with thickness smaller than 100 nm.

the thermoelectric properties of bulk silicon are not good enough to appear interesting for the realization of thermoelectric devices. In fact while the silicon PF at room temperature in the case of the optimum dopant concentration (near 1 x10^{19} cm^{-3}) is comparable to Bi_2Te_3 ($\approx 3.5\ mW/m^2K$ for silicon and $\approx 4\ mW/m^2K$ for Bi_2Te_3) its high thermal conductivity ($\approx 130\ W/mK$) two order of magnitude higher than Bi_2Te_3, binds its figure of merit to very small values (≈ 0.01).
Nevertheless recently it has been demonstrated that silicon thermal conductivity can be decreased significantly in silicon NWs and NLs when their diameters are reduced to a scale of tens of nanometers in the presence of rough surfaces [64, 65, 70]. This dramatic decrease of silicon thermal properties is attributed to the strong enhancement of the phonon scattering with the boundaries of the structure, further increased by the surface roughness.
Although this evidence has attracted around silicon NWs a lot of academic interest, their application in commercial thermoelectric devices seems infeasible because of the difficulties described in 2.4.5. Therefore, as already mentioned, the focus should shift to designing bulk solids which can mimic the enhance of thermoelectric properties of nanostuctures. Furthermore, as it was shown in section 2.4.5, high conversion efficiencies which imply necessarily high thermal resistances and hence low output powers, are not always suitable.

This PhD work would be well included in this picture, since it is focused on the translation of features showed by silicon NWs into a thin film material which can exhibit high power output (through its very high PFs) and the possibility to tune its thermal properties with feasible and scalable technique.

Chapter 3

Nanocrystalline Silicon: Power Factor enhancement by dopant segregation

This PhD thesis has been devoted to the preparation, the study and the characterization of nano-crystalline silicon thin films for thermoelectric applications.
Based on previous work carried out by my research group, such systems had been found to be an interesting example of bottom-up nanostructured material for thermoelectric applications.

As be reported in the first section of this chapter, preliminary experimental evidence on the thermoelectric properties of nanocrystalline silicon thin films highly doped with boron, had showed an unexpected enhancement of their power factor upon thermal annealing cycles. This unusual behaviour had called for further investigations and explanations.

Therefore in this chapter the study carried out on the unexpected beneficial effects of thermal annealing will be reported following two main streams: the samples reproducibility and the validation of a model explaining these features.

3.1 Previous works on polycrystalline silicon thin films

Polycrystalline silicon thin films has been considered for thermoelectric applications by several groups around the world. In fact the presence of grain boundaries (GBs) can easily thought as a simple way to decrease the highly thermal conductivity of bulk silicon.
However all the works reported within the literature, which include different kind of doping and material characteristics [87, 12, 13, 14], showed very small values of power factor ($\approx$ 1-2 mW/mK^2) and of figure of merit ($\approx 10^{-2}$) at room temperature. This evidence brought researchers to conclude that poly-silicon was unlikely to be implementable in thermoelectric devices.

Nevertheless, experimental evidence of high power factors was found in degenerate nanocrystalline silicon thin films [88, 89, 6]. In fact it was shown that this kind of systems shows a simultaneous increase of electrical conductivity and Seebeck coefficient upon thermal annealing. This increase leads to power factors higher by about one order of magnitude respect to the ones reported in literature.
The sample showing these features, named S1, was 450 nm thick, with a boron concentration of 4.4x10^{20} cm^{-3} (details on the samples preparation can be found in [88]). In Fig. 3.1 it can be seen that the simultaneous increase of electrical conductivity and Seebeck coefficient was accompanied by a strong decrease of the dopant activity and a large enhancement of the electrical mobility (Fig. 3.1b). At this dopant concentration, carriers mobility is dominated by ionized impurity scattering (as confirmed by the mobility trend vs. dopant concentration) and one would expect mobility values similar to the single crystal case at similar dopant concentrations. Instead, mobility at the highest annealing temperature was found to be nearly 20% higher that of monolithic Si. This peculiar feature joins with the evidence that the Seebeck coefficient enhancement was too strong to be explained as being due to a decrease of the dopant concentration [88], called for a different explanatory model.
Since in S1 boron concentration was higher than its reported solid solubility in single-crystal silicon [90], and since boron is also known not to

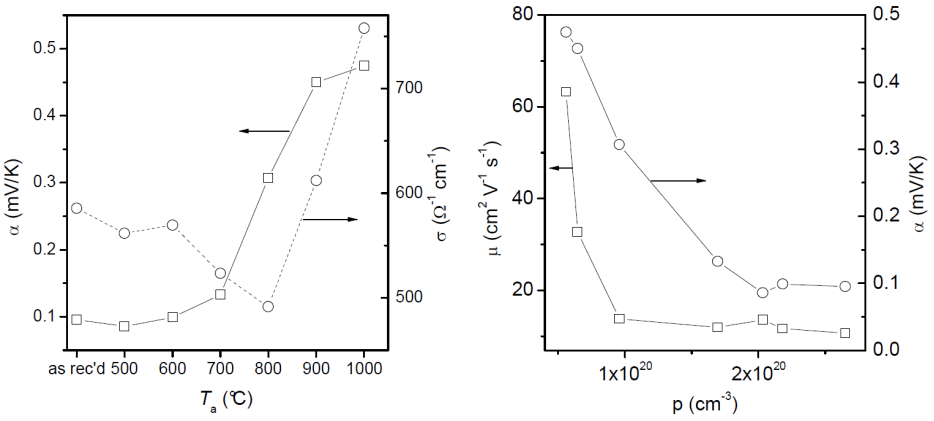

Figure 3.1: Seebeck coefficient and electrical conductivity along thermal annealing for nanocrystalline silicon thin films (left); Sebeck coefficient and electrical mobility along carrier concentration for the same samples (right). Reproduced with permission from [6].

precipitate on the GBs itselves but to segregate instead around them, a second phase was thought to be formed around GBs by thermal annealing . This second phase was supposed to create a potential barrier, able to filter energetically electrical carriers and then inducing an enhancement of the PF (cf. 2.4.3).

Therefore from the evidence just described it was possible to outline a simple preliminary explanatory model where three ingredients seemed needed for high ZT to show up: (1) the polycrystalline phase in which GBs can act as second phase creation centres; (2) a boron concentration higher than its solid solubility in order to enable segregation and second phase formation; (3) thermal treatments promoting the second phase formation.

3.2 Reproducibility and Model Confirmation

In order to validate the experimental results and the model sketched, a study on the reproducibility and the model parameters was established. Regarding reproducibility, several samples with the same characteristics of

sample S1 were prepared and characterized. Furthermore, some of the S1 clones underwent different thermal treatments, in particular to annealing performed directly at 1000°C instead then the annealing cycles already described.
Regarding the study on the model parameters, a variety of silicon-based systems meeting only some of the model requirements were prepared, changing dopant concentration and material micromorphology (i.e. grain size and orientation). Micromorphology was modified by changing the substrate and the deposition conditions. Substrates were chosen so that their different thermal resistances might have promoted the growth of films with different grain sizes and shapes. This allowed to verify whether the anomalous increase of the power factor actually requests a peculiar film morphology. From this study it has been shown that the anomalous growth of the power factor at the highest annealing temperatures T_a actually requires the concurrent presence of a nanograined morphology along with the formation of boron-enriched nanoprecipitates.

Table 1 summarises the characteristics of all samples studied compared also to sample S1. In short, three types of substrates were used, namely oxidised silicon (S family), a SiO_x-Si_3N_4 bilayer deposited onto oxidised silicon (T family) and a silica substrate (Q sample).

ID	Thickness (nm)	Impl. En. (keV)	Dose (cm^{-2})	Boron density (cm^{-3})	Grain size and orient. (nm)	Second phase
S1	450	60	2.0×10^{16}	4.4×10^{20}	$100\ \perp,\ 30-50\|\|$	observed
S2	200	30	0.4×10^{16}	2.0×10^{20}	$100\ \perp,\ 30-50\ \|\|$	absent
S3	200	30	0.8×10^{16}	4.0×10^{20}	$100\ \perp,\ 30-50\ \|\|$	absent
S4	200	30	1.2×10^{16}	6.0×10^{20}	$80-100\ \perp,\ 50-100\ \|\|$	observed
T1	200	30	1.2×10^{16}	6.0×10^{20}	$80\ \perp,\ 50-100\ \|\|$	absent
T2	200	30	0.4×10^{16}	2.0×10^{20}		
Q1	490	40	2.5×10^{16}	5.1×10^{20}	$100\ \perp,\ 100-150\ \|\|$	observed
SOI	342	50	2.5×10^{16}	3.5×10^{20}	–	

Table 3.1: Summary of the characteristics for the various samples prepared and characterized in this study.

3.2.1 Sample preparation

Polycrystalline films were all deposited by chemical vapour deposition (CVD). Silane was used, always keeping the substrate at 610 °C but for sample S1, for which a deposition temperature of 600 °C was chosen. In addition, silicon-on-insulator (SOI) single crystalline films were also analysed. All samples were boron doped by ion implantation at different doses and energies to obtain degenerate silicon films with nominal boron densities ranging around its solubility threshold at 500 °C [90] [1].
After damage recovery, samples underwent sequential thermal treatments up to 1000°C in argon, each step lasting 2 h. These annealing were always performed preheating the oven to the desired temperature in order to perform a very rapid thermal ramp.

Al-Si 5% pads were evaporated for all transport measurements and were removed by HCl followed by piranha etch (H_2O_2 33 vol%+H_2SO_4 98 vol% in a 1:2 ratio, 95°C, 30 min) and HF (5% vol.) prior to the subsequent annealing. The metallizations were performed by thermal evaporation in high vacuum ($\approx 10^{-8}$ mbar) using a vacuum chamber connected to a rotative and a diffusive pump in series.

3.2.2 Experimental Procedures

The samples characterization includes two main steps: an electrical and thermoelectric characterisation including electrical conductivity, Hall effect, and Seebeck coefficient measurements; and a morphology investigation performed by Transmission Electron Microscopy analysis.

Electric and Termoelectric characterizations: conductivity was determined by current-voltage characteristics at 20 °C. Furthermore, measurements of σ also as a function of the temperature were carried out in order to confirm for all samples a negative temperature coefficient as

[1] Sample deposition and Boron implantation were performed by the CNR - IMM institute of Bologna (Italy), and in particular by the team lead by Dr. Alberto Roncaglia, in the picture of a collaboration with the research group in which the PhD candidate has worked.

expected in a degenerate semiconductors. Those measurements were performed by using of a refrigerator-cooled cryosystem in which a helium compressor unit, a cold head, and vacuum chamber used as the thermostat were able to cool the sample down to 20 K.

Samples for the Seebeck and the electrical conductivity measurements were obtained by cutting 50x5mm^2 rectangular chips and evaporating metal contacts through a shadow mask. Seebeck coefficient was measured using a lab-made apparatus based on the so-called integral method. In this configuration one of the sample ends is held at a fixed temperature and the other brought to a larger temperature varied through the range of interest. The Seebeck coefficient at a selected temperature can then be obtained from the slope of the Seebeck voltage (V_{th}) versus temperature, $\alpha = \frac{dV_{th}(T)}{dT}$, at that temperature [91]. However in the case of constant

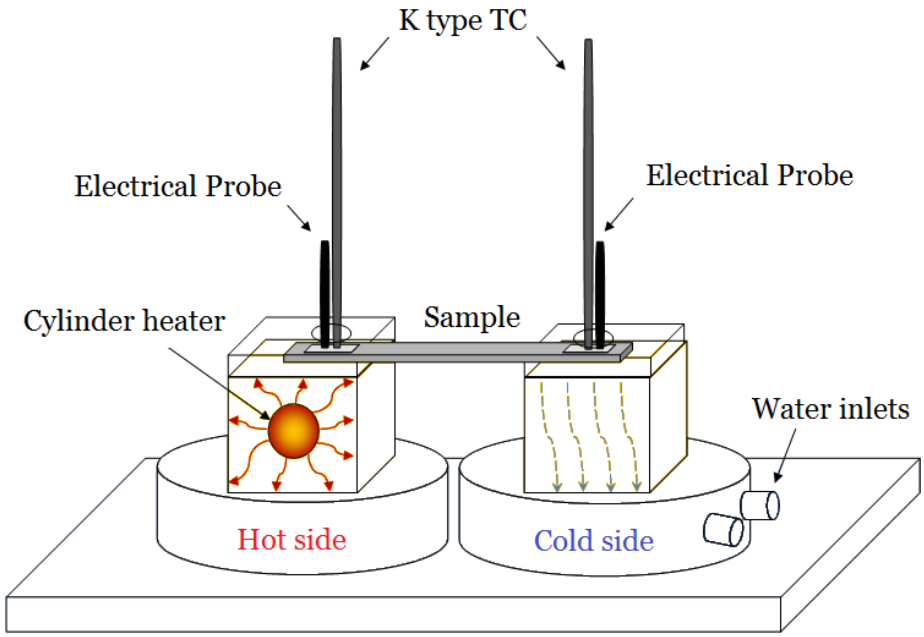

Figure 3.2: Scheme of the experimental setup for room temperature Seebeck measurements

Seebeck coefficient along the range of temperature measured, the slope $\frac{dV_{th}(T)}{dT}$ is constant and then V_{th} shows a linear relation along T. For our samples and in the range of temperature exploited, this condition was always verified to be true.
The apparatus used for this work (Fig. 3.2) was composed of a sample holder with two copper blocks respectively used as hot and cold side. For each of them two thermocouples and two electrical probes were installed to measure the temperature difference over the specimen and the resulting Seebeck voltage. The cold side was water cooled and held around 10°C while the hot side temperature was varied from room temperature to 100°C by an electrical heater. Data were acquired by a digital voltmeter equipped with a voltage scanning card interfaced with a computer through a LabView program. The temperature was manually adjusted changing the power supplied to the heater and waiting steady state conditions for both temperatures and voltage output before collecting data points. For all samples, three or four measures at different hot temperatures were recorded and then a linear fit was performed in order to obtain the Seebeck coefficient as well as information regarding the linearity of V_{th} and its intercepts with the axis (which should be equal to zero). Furthermore each set of measurements was repeated on the same sample at least three times to ensure data reliability.
At the beginning of this work the apparatus was calibrated toward single crystal silicon samples of known doping level and compared to the literature [92], enabling the estimation of its precision which were evaluated to be better than ±10% with a reproducibility better that 5%.

For Hall measurements, 17x17^2 mm^2 samples were cut and metal contacts were evaporated on small areas in the four corners according to the Van der Pauw geometry [93]. Hall measurements were carried out at room temperature with a maximum magnetic field of 0.5 T.
Accuracy was found to be better than ±1%. Precision was instead estimated, based on the deviation of contact design with respect to the ideal Van der Pauw configuration [94], to be +0/-17% for the Hall mobility and of +18/-0% for the carrier density.

Morphology: cross-sections for electron microscopy (EM) analyses were prepared by conventional methods, grinding, polishing and finally thinning the samples with an argon ion beam. Electron microscopy (EM) analyses were performed both in low energy (30 keV) dark field scanning transmission EM (DF-STEM) and in high-energy (200 keV) transmission (TEM) mode. Low-energy analyses have been performed with a FEI Strata235M equipped with bright field (BF) dark field (DF) solid state detector. TEM and energy filtered electron spectroscopic images (ESI) have been performed with a JEM2011 electron microscope (spherical aberration coefficient 0.5 mm, chromatic aberration coefficient 1.1 mm) equipped with conventional LaB6 electron source and an electron energy loss imaging filter (GIF 200®). This attachment allows to record both electron energy loss spectroscopy (EELS) data and ESI[2].

3.2.3 Results

Reproducibility of the simultaneous enhancement of electrical conductibility and Seebeck coefficient was confirmed for all the S1 clones. PF values were demonstrated to range within 15%. Furthermore, samples that underwent direct heating at 1000°C showed the same range. Therefore annealing cycles up to 1000°C or one-shot annealing, drove to similar results in terms of thermoelectric performances. This evidence led to the conclusion that the sample thermal history does not affect PF enhancements if the final annealing temperature and the annealing duration are comparable.

TEM analyses (Fig. 3.3) further showed that, while the thermal processing did not significantly modify the grain size, it caused a precipitation of a boron-rich second phase around the grain boundaries - not decorating the grain boundaries themselves. As already mentioned such a unique feature is known and reported in literature for boron [95], and encouraged to correlate the anomalous dependency of the mobility to the formation of potential barriers associated to the presence of precipitates. All polycrystalline films actually exhibited columnar growth, with grain aspect ratios

[2]Cross-section preparation and TEM analysis were performed by Prof. Stefano Frabboni at the University of Modena and Reggio Emilia (Italy).

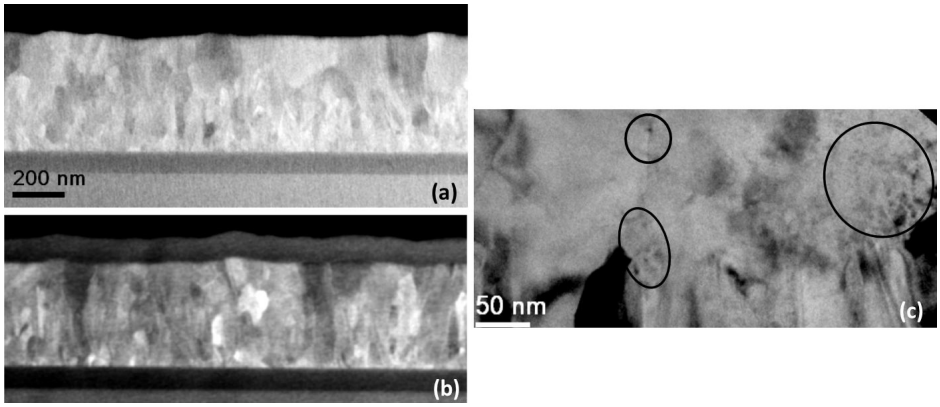

Figure 3.3: (*a*) DF-STEM image of the as-deposited S1 sample; (*b*) DF-STEM and (*c*) TEM bright field image of the same sample, both taken after annealing at 1000 °C. Circled areas in the TEM image mark diffraction contrast details due to the precipitation of a second phase. Note the preservation of grain sizes upon annealing at high temperature. Reproduced with permission from [7].

somewhat larger in the S than in the T or Q families. Figure 3.4 reports a comparison of the span of α, σ, and of the power factor measured on the samples considered in this work and consequent to the thermal processing. Of the three features considered as possibly responsible for the increase of the power factor, the role of degeneracy in itself can be immediately discarded. Single-crystalline SOI film, although degenerate, did not display any increment of the power factor significantly above the value theoretically expected for silicon (≈ 3 mW K^{-2} m^{-1} [92]). This is in good agreement with a rather large body of previous studies on heavily doped silicon [92, 96, 97]. Not even the precipitation of a second phase, expected for a heat-treated material with a nominal boron density $> 2 \times 10^{20}$ cm^{-3} appears to be sufficient to determine the mobility enhancement observed in S1.

Moving to polycrystalline films, the role played by the total boron concentration is quite evident comparing samples from the S and T families. Whenever boron content is lower than 4×10^{20} cm^{-3}, no precipitation of boron is either expected or observed - and no anomalous increase either of the mobility or of the power factor is found. It may be worthwhile to

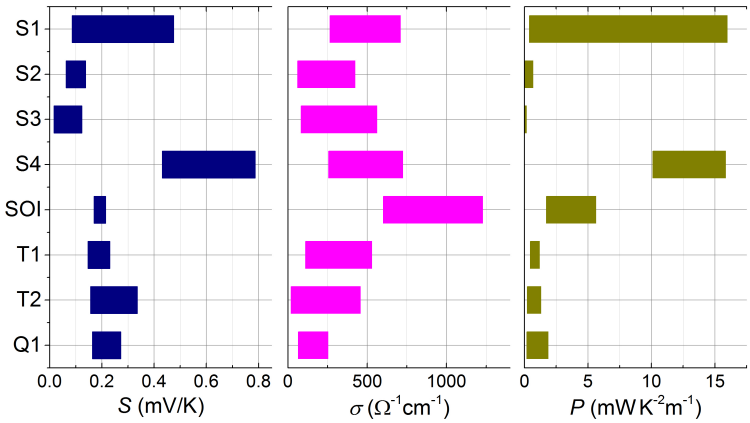

Figure 3.4: Variation of the thermoelectric coefficient, the electrical conductivity, and the power factor as a result of thermal processing up to 1000 °C on samples described in Table 3.1. Reproduced with permission from [7].

stress that the actual formation of boron precipitates is not simply related to thermodynamic considerations. Apart from the effect on the solubility threshold of grain boundaries and their eventual decoration [98], the formation of a second phase upon relatively short (2 hours) heat treatments is also ruled by boron diffusivity. Using standard models [99] it can be verified that, in the range of temperature-time conditions considered in this study, boride precipitation occurs only for initial boron concentrations exceeding $\approx 4 \times 10^{20}$ cm^{-3}. This is consistent with our experimental results, where no formation of boron-rich second phase was actually observed for lower initial boron densities.

Boron supersaturation is not however sufficient to induce a power factor enhancement. While actually sample S4 reports a power factor value comparable to that observed on S1, no likely effect is observed either on sample T1 or Q1. Interestingly enough, sample Q1 displays a concurrent increase of α and σ upon annealing, but the final power factor value it reaches after the heat treatment at 1000 °C is about one order of magnitude lower than that observed in S1. A key to understand such a difference is in the grain size, much larger for Q1 than for S1. Since energy filtering is proportional to the volume of grain boundaries and its effect is larger when energy relaxation within the grains is less efficient (i.e. when grain size is small),

it is not unreasonable to conclude that carrier filtering is active but less effective in Q1, explaining its lower performances.
Sample T1 is more puzzling. Absence of a second phase clearly explain the lack of power factor enhancement. Yet it is not immediate to understand why, in spite of the high nominal boron density, no precipitation occurs upon annealing. In principle, since diffusivity in polycrystalline materials strongly depends on the structure of grain boundaries, a larger abundance of grains oriented along 311 (reported by TEM) might provide a rationale to the observed metastability of the boron-silicon solution.

Therefore it seems sensible to conclude that an enhancement of the power factor in silicon does require the concurrency of the following features: (1) a grain size enabling only partially energy-relaxed carrier transport; and (2) the presence of suitable energy filtering barriers (in our case the boron-rich second phase) preventing slow carriers from participating in the energy and charge transport. Grain sizes from 30 to 50 nm (cf. samples S1 and S4) were found to best suit such requirements. Energy filtering in single crystals and in relatively large-grained polycrystalline materials only partially compensates the reduction of σ resulting from a decrease of the actual carrier density. No simultaneous increase of the thermopower and of the electrical conductivity is found as charge transport occurs in the diffusion regime, so that carrier relaxation dumps the effect of energy filtering on electrical mobility. Instead, in nanocrystalline systems with grains small enough to allow only partial carrier energy relaxation, filtering fully enables the participation of fast carriers only to conduction, leading to the observed overcompensation of the lowered carrier density.

3.2.4 Computational work

In order to validate the results just reported and to strengthen the picture justifying such an unexpected PF increase, a computational work was established. In this thesis the discussion will be limited just to the assumptions and results of this computational work. Details are reported in [8, 100][3].

[3]The computational work described in this section were developed by Dr. Neophytos Neophytou at the Technical University of Vienna (Austria), and Prof. Xanthippi Zianni at the National Center for Scientific Research-Demokritos, Athens (Greece), in the

The computation uses a semiclassical one-dimensional model that considers electron and phonon transport through nanocrystalline Si with grain size $L_G = 30$ nm, grain boundary width $L_{GB} = 2$ nm, and barrier height $V_b = 0.165$ eV. This assumptions were used in order to mimic the as-grown material characteristics, namely before being subjected to the thermal annealing. While L_G and L_{GB} were set based upon TEM images, V_b results from the analysis of hole mobility versus temperature [8, 101].
The effect of the thermal annealing on the system was modelled by considering a modification of V_b with carrier density within the grains. Three cases were considered (Fig. 3.5) the first assumes uniform thermal conductivity κ_l=140 W/mK in the entire material (blue lines); the second assumes a non-uniform thermal conductivity with $\kappa_G = 12$ W/mK and $\kappa_{GB} = 2$ W/mK (red lines); the third make the same assumptions of the previous two cases, but in addition it considers a depletion width such that that reduces the carrier concentration in the grain to 55% (green lines). All these cases are compared also with bulk silicon (black line). Figure 3.5 clearly show that the third is the only case able to justify a strong simultaneous increase of electrical conductivity and Seebeck coefficient. Therefore this phenomenon was proposed to result from the fact that as the barrier rises and/or the width of the depletion region around the grain boundary increases, two effects take place: (i) the Fermi level rises, and is placed well inside the valence band (it has been evaluated that E_F is 0.095 eV into the valence band) which allows only faster high energy carriers to participate in transport, and (ii) the overall MFP for scattering increases because high energy carriers are scattered less by impurities, which are the dominant scattering centres. These two effects compensate the detrimental effect of the grain boundary barriers on the conductivity, and for $p < 10\times^{20}$ cm^{-3} (or above a specific E_F), an overall increase in σ is achieved. The rise in E_F is possible because the volume (or length) of the grain boundary together with the depletion region are comparable to the volume of the grain (≈ 30 nm). For larger grain sizes, i.e. 1 μm, where the grain boundary and depletion region occupy a very small portion of the overall volume, simulations show that PF approaches the bulk value

picture of a collaboration with the research group in which the PhD candidate has worked.

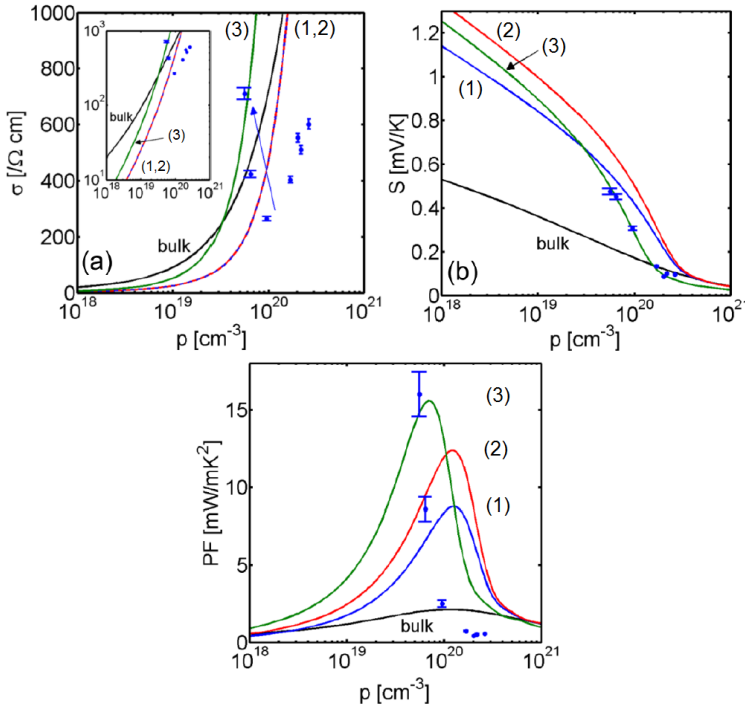

Figure 3.5: Comparison between experimental (blue dots) and the computational data for three different cases: (1) uniform thermal conductivity κ_l=140 W/mK in the entire material (blue lines); (2) non-uniform thermal conductivity with κ_G = 12 W/mK and κ_{GB} = 2 W/mK (red lines); (3) same assumptions of the previous two cases, but in addition it considers a depletion width that reduces the carrier concentration in the grain to 55% (green lines). Black lines represent the case of bulk silicon. The three graphs are for: (a) electrical conductivity: (b) Seebeck coefficient; (c) Power factor. Reproduced with permission from [8].

within 10%. Therefore, both nanocrystallinity and extremely high boron doping levels at the center of the grain are essential ingredients for this novel observation, in excellent agreement with the conclusions drawn in section 3.2.3 .

Furthermore a non uniform thermal conductivity has to be considered in order to fit the experimental data. This assumption seems quite natural considering that the thermal conductivity in the grain would be surely higher than at the grain boundaries. This feature consequently implies a

non uniform temperature distribution. Therefore the Seebeck coefficients has to be weighted by the temperature drops in the two different regions, with the result that the Seebeck coefficient in the regions with low thermal conductivity is dominant. The electrical conductivity, (Fig. 3.5a) is not affected by this assumption (red and blue lines coincide).

Summarizing, the theoretical investigation, developed along with experimental characterizations reveals that: (1) the improvement in the Seebeck coefficient can be attributed to carrier filtering due to the energy barriers at the grain boundaries, and to the difference in the lattice thermal conductivity of the grains and grain boundaries, and (2) the improvement in the electrical conductivity is a result of a high Fermi level in the grains, due to the formation of a depletion layer associated to the second phase formation around GBs. This allows high energy carriers only to contribute to transport, which increases the impurity scattering limited mean-free-path, and increases the conductivity in the grains and thus in the whole material
These conclusions seem to be in very good agreement with what reported in the previous section, completing the picture on the PF enhancement effect.

Chapter 4

Nanocrystalline Silicon - Phonon Engineering by Nanovoids

In the second part of this thesis it was demonstrated that a tuning of the thermal properties of silicon thin film can be made through the formation of a dispersion of nanovoids (NVs).

The motivation for this study was the evidence that even if nanocrystalline silicon thin films present smaller thermal conductivities than single crystal, these values are still to high, limiting their figure of merit.

In this work a dispersion of NVs were obtained using a technique well know for single crystal silicon, based upon helium implantation and subsequent thermal annealing. After having shown the possibility to use such technique to form NVs with tunable size and density, the work focused on the study of NV effects on thermal and thermoelectric properties.

The work was then organised as follows. Firstly a batch of silicon thin films (the same presented in the previous chapter) were implanted with helium and the treated with different procedures. The samples were then analysed from a morphological point of view, investigating the NV presence and characteristics. The thermoelectric properties were characterised to understand the compatibility of NVs with the energy filtering

effect exhibited by those structures. Finally, the thermal properties were measured and analysed.

4.1 Thermal properties of silicon thin films

As discussed in section 2.4.6 because of its very high thermal conductivity (≈ 130 W/mK) single crystal silicon is unlike to be used for thermoelectric applications.
However silicon thin films, especially if polycrystalline, can show much better thermal properties. Thermal conductivity is actually decreased by: (1) the finite thickness, which provides a huge source of phonon scattering with the system boundaries; (2) the presence of GBs, which also provide a source of phonon scattering. Furthermore the presence of dopant can contribute to these mechanisms.
Consequently the thermal conductivities of polycrystalline silicon thin films is a function of the thickness, the grains size and orientation, and the doping level.

Fig. 4.1 shows a summary of literature data about those dependences for single crystalline silicon [9]. In particular in Fig. 4.1(a) is reported the dependence of thermal conductivity along the film (layer) thickness and in Fig. 4.1(b) the same trend vs. doping. As expected, κ decreases when the thickness decreases and/or upon increasing the dopant concentration. A more difficult matter is instead the dependence of thermal conductivity on grain size in polycrystalline silicon thin films, since this contribution

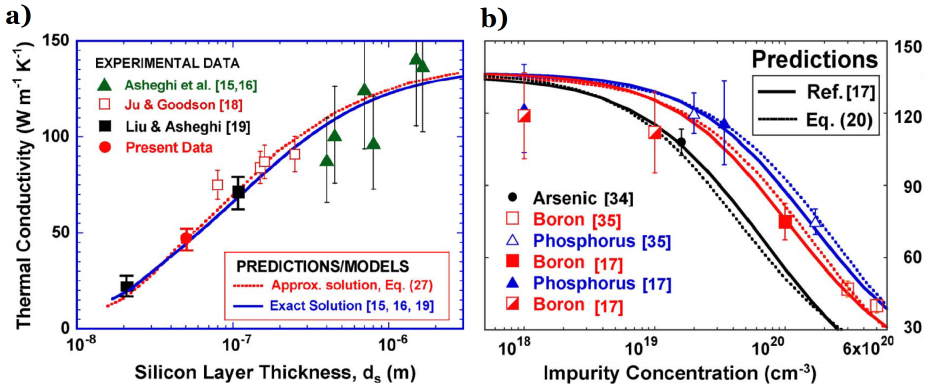

Figure 4.1: Summary of thermal conductivity vs. (a) thickness and (b) doping, in single crystal silicon thin films. Reproduced with permission from [9].

depends upon the grain orientation and the defects density within the GBs. However in the literature typical values of κ for polycrystalline silicon with thickness and doping of the same order of magnitude than those object of this study are reported to be around 15-30 W/mK.

4.2 Previous work: Helium implantation

Helium implantation in single crystal silicon and subsequent thermal annealing are a well known and characterized technique to create NVs with tunable dispersion and characteristics. In the literature is possible to find works related to helium implantation starting from 1970. Most of these studies were focused on the effects of NVs for applications in microelectronics. In fact these structures has been reported as: (i) efficient getters for transition metals [102, 103, 104, 105, 106, 107]; (ii) reactants with point defects affecting dopant diffusivity and secondary defects [108, 109]; (iii) deep levels within silicon band gap useful to control carrier lifetimes [110, 111, 112].

The process of NVs creation can be described as follows: (1) a certain dose of helium ions are implanted within the sample with a given energy; (2) helium entering within the crystal structure generates vacancies in amounts and depth with depending on the implantation dose and energy, respectively; (3) then thermally treating the implanted sample it is possible to promote vacancy aggregations around He atoms that start forming (at low temperatures) di-vacancy complexes and then (at higher temperatures) nano-bubbles filled with helium; bubble formation and growth can be due, depending on the implantation parameters by coalescence process or Oswald repining [113]; (5) at high enough temperatures ($> 700-800°C$) helium out-diffuses from the bubbles and the sample, leaving NVs within the silicon matrix; (6) further anneling can promote change in the NV shapes which reach at temperatures higher than 1000° tetrakaidecahedral geometry [114].
Multiple helium implantation can be implemented in order to obtain different NV distribution and size[115].

In this work, the mentioned literature and some preliminary feasibility studies (carried out in the frame of a previous PhD work [116]) served as reference state for this project.
The first aim was to reproduce the NV generation process for the nanocrystaline silicon thin films and exhibiting the simultaneous enhancement of electrical conductivity and Seebeck coefficient.

4.3 This work: Samples preparation

Two wafers of 450–nm thick nanocrystalline silicon films, doped with boron to the nominal concentration of 4.4×10^{20} cm^{-3} (thus exactly the same described in previous chapter) were submitted to a two–step helium implantation (90 keV, fluence of 4×10^{16} cm^{-2}; 58 keV, fluence of 1.5×10^{16} cm^{-2}) through an aluminum sacrificial layer[1]. Implantation at two energies and doses enabled to obtain a rather uniform distribution of helium atoms along the film thickness, as can be seen in Fig. 4.2 where TRIM simulations [117, 118] (TRansport of Ions in Matter) are reported. TRIM is a Monte Carlo algorithm that calculates the interactions of ions with solid matter. Fig. 4.2(a) shows the most probable position and amount of the helium atoms within the sample.
Fig. 4.2(b) shows instead a simulation of the damage induced by the implantation, than it is correlated with the vacancy position and amount. This graph shows that while the damage is uniformly distributed along the film thickness, the helium atoms are located mostly in a deep region. This distribution prevents a premature out-diffusion of helium from the samples.
However it should be noted that the simulations just described are based on the assumption of a target material consisting of single crystal silicon. The presence of GBs is not taken into account, so the results should be considered as only indicative guidelines.

After removal of the aluminum film by etching in hydrochloric acid, the chips were annealed in argon. Four samples were studied as reported

[1]Helium implantation was performed by Prof. Giampiero Ottaviani and Dr. Rita Tonini of the University of Modena and Reggio Emilia (Italy), at the National Laboratories of Legnaro LNL - INFN (Italy).

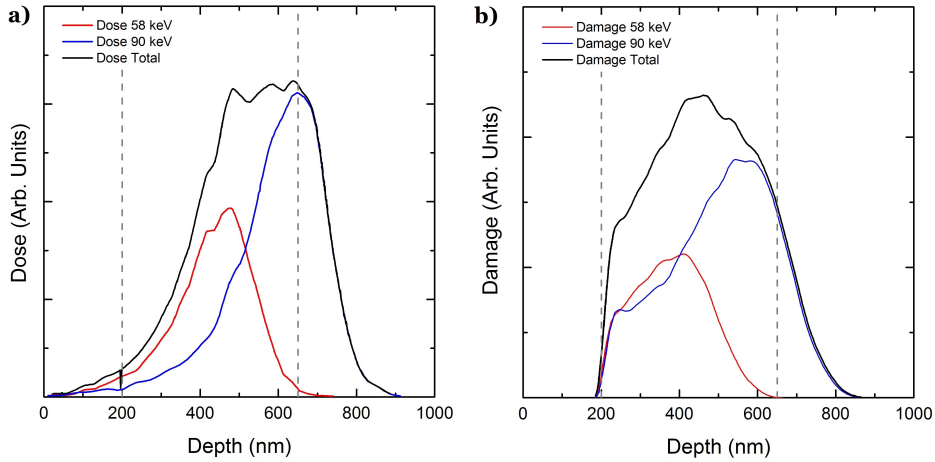

Figure 4.2: TRIM simulations for the two step He^+ implantation made on the nanocrystalline silicon thin films object of this study. (a) Helium dose as a function of the film depth; (b) Damage due to He^+ penetration as a function of the film depth. The dashed grey lines represent the film top and bottom surfaces.

in Table 4.1. Samples A and B underwent a single two-hour annealing at 500°C and 1000°C, respectively. Sample C was instead sequentially annealed at 500 and 1000°C. Finally, a full sequence of treatments from 500 to 1000°C in 100°C steps was carried out on sample D. Each annealing step for samples C and D lasted two hours.

ID	He impl. Dose (cm^{-2})	He Impl. En. (keV)	Thermal Treatments (TT) (K)	TT time (hours)
A	$4 \times 10^{16} + 1.5 \times 10^{16}$	90 + 58	500	2
B	$4 \times 10^{16} + 1.5 \times 10^{16}$	90 + 58	1000	2
C	$4 \times 10^{16} + 1.5 \times 10^{16}$	90 + 58	500 + 1000	2 each
D	$4 \times 10^{16} + 1.5 \times 10^{16}$	90 + 58	500 - 1000 (step 100)	2 each

Table 4.1: Summary of the helium implantation and thermal treatments characteristics.

4.4 Experimental Procedures

As mentioned, the characterisation consisted of: (1) an investigation on the NV formation process, correlating thermal treatments and NV morphology; (2) electrical and thermoelectrical characterization in order to test the compatibility between NV formation and energy filtering effect; (3) a characterization of the thermal conductivity variation due to NVs. In this section all the techniques and measurement tools used for these characterisations will be described.

4.4.1 Temperature Programmed Desorption

In order to evaluate the density of helium atoms actually present inside the silicon lattice, temperature programmed desorption (TPD) measurements were carried out after helium implantation. TPD experiments, consisting of the measurement of the helium effusion rate, measured by a quadrupole mass spectrometer during a thermal treatment in a temperature ramp with assigned heating rate, is an ideal technique to study the evolution of vacancy–related defects in helium implanted silicon [119, 120]. TPD actually gives insight into the structures wherein helium is trapped. TPD spectra were performed at a pressure of $\approx 10^{-6}$ mbar, with a ramp rate of 0.75 K/s in the temperature range 80–800°C. In order to determine the total amount of helium, three TPD runs with the same heating rate were performed on the same sample[2].

4.4.2 Hall and Seebeck measurements

Also for these samples Hall measurements were performed in order to characterise electrical conductivity, electrical mobility and carrier density. The apparatus used was the same described in subsection 3.2.2 with the addition of a dedicated sample holder able to heat the sample up to 100°C. With the use of such configuration it was possible to perform precise measurements as function of temperature.

[2]TPD measurements were performed by Dr. Rita Tonini at the University of Modena and Regggio Emilia (Italy).

4.4.3 Morphological characterization

The morphological investigation was carried out by TEM. These analyses were performed with a Jeol 2011 microscope (with spherical aberration coefficient - $C_s = 0.5$ mm, and chromatic aberration coefficient - $C_c = 1.1$ mm). Images of nano-bubbles and voids were acquired in out-focus mode in order to enhance their visibility. Image resolution in this mode is approximately 1 nm[3].

The images were then analysed with a graphical computer program (Klonk Image Measurement®) in order to estimate the NV total volume, size, and density.

4.4.4 Thermal Conductivity Measurements

Thermal conductivity was measured with a pico-second time domain thermoreflectance (TDTR) apparatus[4]. This technique consists of inducing heat generation within a sample by an incident laser pulse (pump beam), measuring the temperature increase by probing the changing reflectance of its surface (with the probe beam). In Fig. 4.3 a scheme of the apparatus used is reported. The pump beam is injected by a periodic pump pulse from a mode-locked Nd:YVO_4 laser (9.2 ps pulse width, 82 MHz repetition rate, ≈10 nJ/pulse energy, 1064 nm wavelength) establishing a transient temperature field within the sample. The surface temperature is then measured by a delayed probe beam, derived from the pump, which is reflected from the sample and collected by photodetector. The pump beam is externally modulated at variable frequency (between 1 and 10 MHz) by an electro-optic modulator for lockin detection and converted to 532 nm with a second harmonic generator to enable the rejection of pump leakage at the detector. The coaligned pump and probe beams are focused on the sample surface with Gaussian waist. Normally a highly reflective metal coating is deposited on the sample in order to enhance the reflected

[3]Cross-section preparation and TEM analysis were performed by Prof. Stefano Frabboni at the University of Modena and Reggio Emilia (Italy).

[4]TDTR measurements were performed by the candidate during his stage at the NanoHeat group of Prof. Goodson at Stanford University (California - US). The characterisation was performed under the guidance of Aditya Sood and Marc Dunham.

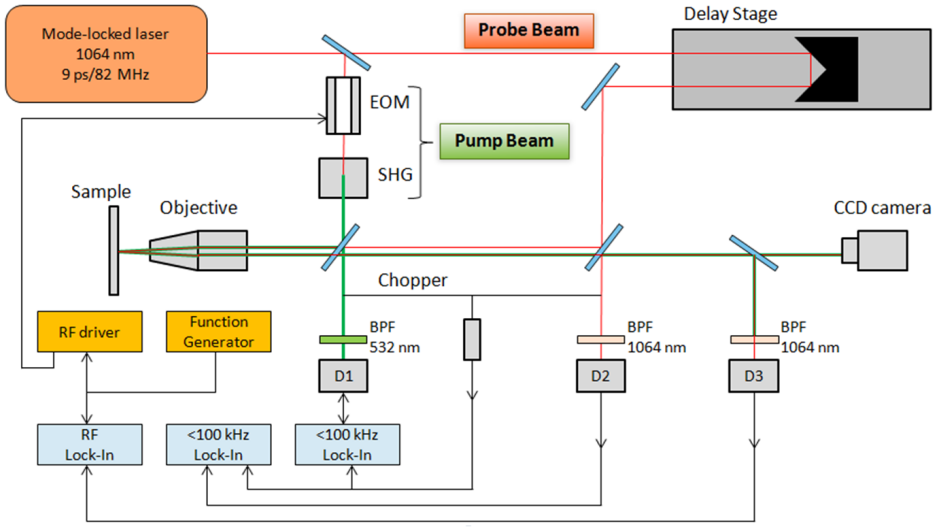

Figure 4.3: Scheme of the TDTR apparatus used for the thermal characterisation.

signal.
In Fig. 4.4 a scheme of the four fundamental measurement step is reported. Fig. 4.4 (a) shows the pump beam pulses, which are then modulated and converted by the second harmonic generator (b). The pump heats the sample and its rapid thermal response falls in between each pump pulse (c), which is then measured since the reflected probe pulse has a modulation caused by the sample thermal response. Finally the response is fitted by a model able to return the thermal conductivity of the sample [121].

TDTR is a technique known since 1986 [122] but only recently it has found wide application especially for its nano-metric resolution, able to isolate the effects of interface conductance from the thermal conductivity of a thin layer [123]. Other great advantages are that it does not request lithographic steps (as for example 3ω method) and its simple adaptability for measurements of κ versus temperature.

The samples reported in Table 4.1 were covered by an aluminium thin film (thickness $\approx$ 50 nm) by thermal evaporation and then measured at room temperature.

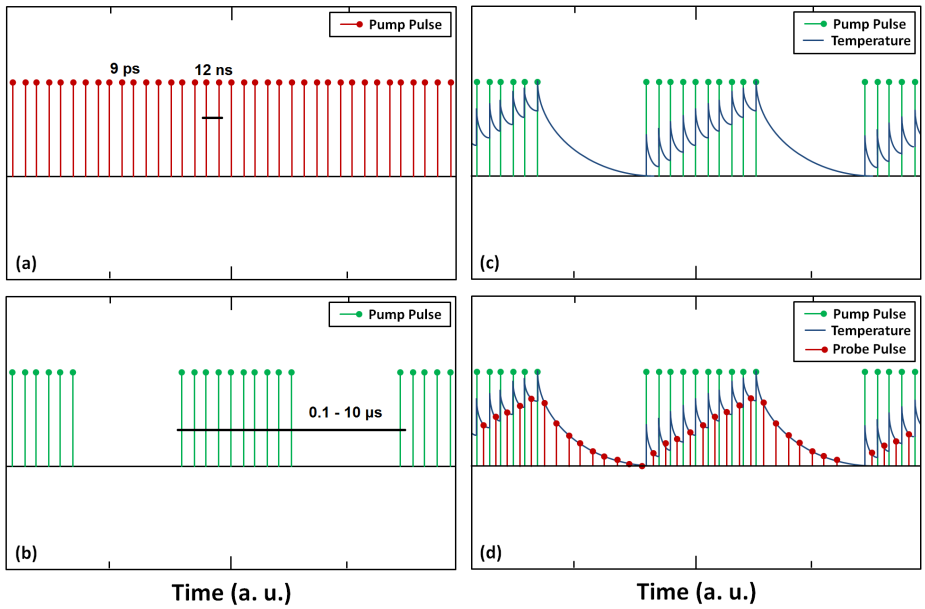

Figure 4.4: Scheme of the four main steps of TDTR measures.

4.5 Results and Discussion

For sake of clarity the discussion will be organised in three subsections, each focused on one of the points described at the begin of section 4.4.

4.5.1 NV formation

TPD analysis performed on the as–implanted sample (Fig. 4.5) showed a total effusive helium fluence of 4.5×10^{16} cm^{-2} (computed by summing the helium flux over the three heating ramps), equalling the implanted dose within the experimental accuracy, and is compatible with data reported in literature for single-crystal silicon [124]. As in the single–crystalline case, a large outdiffusion peak was found around 780°C, along with smaller shoulders at lower temperatures (around 450 °C and at $\approx$ 650°C).
According to the literature the lower temperature peak corresponds to helium desorption due to breaking of small He-vacancies clusters and/or dissolved helium; the second peak relates instead to bubble formation,

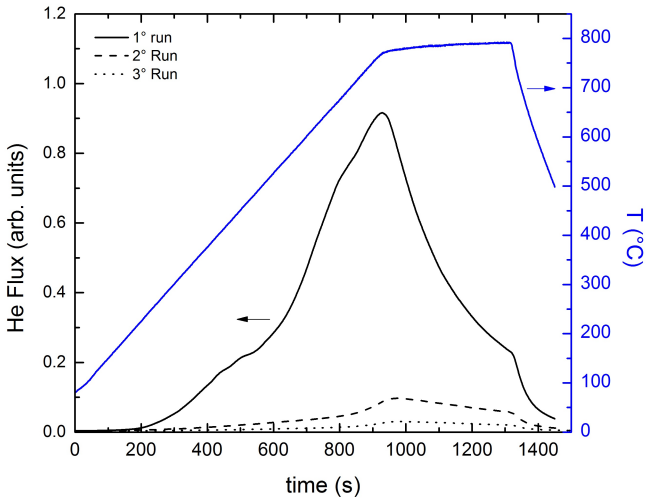

Figure 4.5: Thermally programmed desorption spectrum of He–implanted nanocrystalline silicon vs. run time. The blue line reports the temperature profile vs. time. Three runs of the same ramp were performed on the sample. Reproduced with permission from [10].

since not all the helium is captured within the nanobubbles and then some out-diffuses; finally the temperature higher peak is due to helium escaping from the bubbles and it related to NVs formation.

TEM images of sample A treated at 500°C (Fig. 4.6 a) show that voids of different sizes are present throughout the film. The larger voids are located preferentially near the GBs. Instead, voids within the grains are smaller, with a diameter d_v between 2 and 4 nm. Their density δ_v within the grains accounted to $(3.0 \pm 0.9) \times 10^{17}$ cm^{-3} with a mean spacing of 14 ± 1.7 nm. Assuming voids to be spherical the density of vacancies δ_V in the film can be estimated to be $\delta_v(1/6\pi d_v^3)n_{Si}$ (where n_{Si} is the silicon density). In sample A one obtains $\delta_V = 0.40 \pm 0.12$ nm^{-3}, corresponding to 0.4 ± 0.1 vacancy per impinging helium ion – in good agreement with results reported for single crystals (0.6) [115].
TEM micrographs also provide information about the different morphology evolution upon annealing. In sample C (TT 500 + 1000°C) voids were found to be almost absent or of size close to the TEM resolution threshold

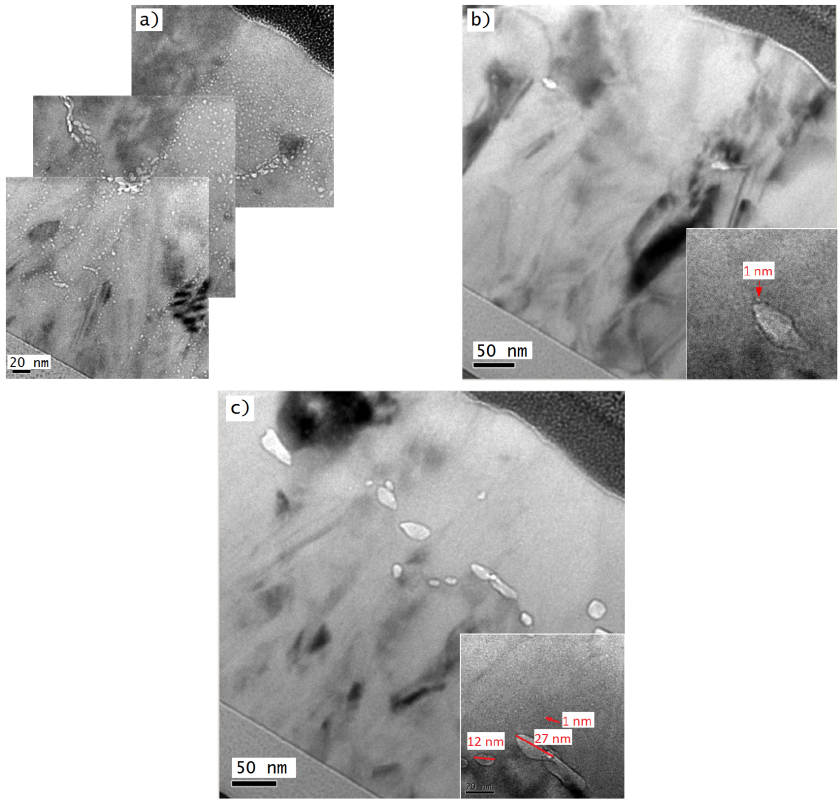

Figure 4.6: TEM images of the He–implanted boron–doped nanocrystalline samples: a) sample A annealed at 500°C; b) sample C annealed at 500 and 1000°C; c) sample D annealed sequentially between 500 and 1000°C with step of 100°C. Reproduced with permission from [10].

(inset of Fig. 4.6 b) – except for a few large voids at GBs.
In sample D (TT from 500 to 1000°C), instead, several voids is observed with diameter ranging between 10 and 30 nm, along with few small voids. Finally, sample B (TT 1000°C) shows voids with an average diameter of 1 nm, their density computing to $(2.0 \pm 0.6) \times 10^{18}$ cm^{-3} (Fig. 4.7 a), with a mean spacing of 8 ± 1 nm. No void is found within 80–100 nm from the outer surface (Fig. 4.7 b) while only very few large voids (located at the grain boundaries) with a diameter ranging from 10 to 50 nm are observed (blue circles in Fig. 4.7 b). In sample B one also computes a total vacancy

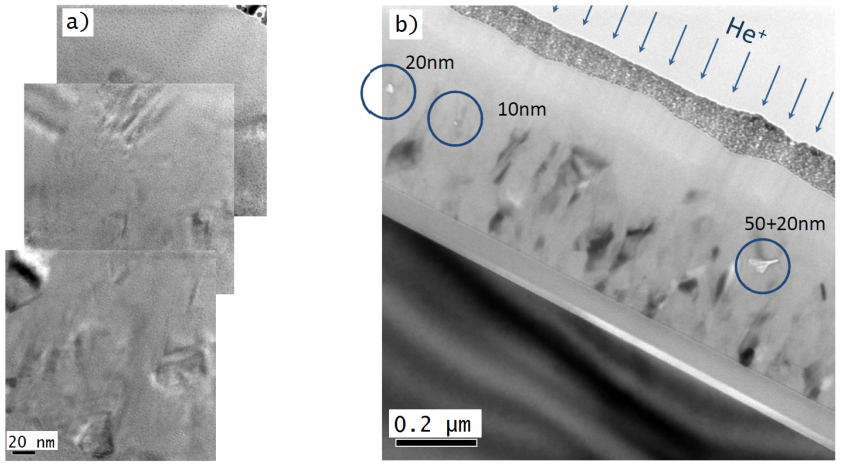

Figure 4.7: TEM micrographs at two different magnifications for sample B: a) at high magnification a huge density of tiny voids is detected; b) at lower magnification an upper layer without voids was found (helium bombardment direction and the few large voids are indicated in blue). Reproduced with permission from [10].

density of 0.40 ± 0.06 nm^{-3}. The fact that this value is the same in both samples A and B indicates that neither evaporation or annihilation of vacancies can be invoked to explain the different morphologies. Vacancies just rearrange differently in the two samples. In other therms samples A and B present the same void volume, thus the same porosity (δ), simply defined as the ratio between the void and the total volumes. In those samples $\delta \approx 0.05\%$.

The behaviour resulting from the analysis of the TEM images is very different from that observed in the single-crystalline case in which coalescence of vacancies rules the size and the density evolution of the voids. As shown in literature [115, 113, 114] in the monocrystalline case vacancies tend to aggregate during the annealing. The presence of dissolved helium leads at low temperature (300°C) to the formation of planar structures called platelets, which then evolve to give lenticularly shaped helium–filled bubbles (400-600°C), finally forming empty tetrakaidecahedral voids with a mean diameter of 10-30 nm upon annealing at 1000°C. In polycrystals, instead, coalescence only partially drives void size and distribution. We

will focus here primarily on voids within the grains. Nanostructures at GBs will follow a different dynamics as GBs are vacancy sinks.
Analyzing the evolution of sample A it is possible to state that the annealing temperature is sufficient to just marginally promote vacancy aggregation, resulting in a high density of small aggregates (Fig. 4.6 a). As TPD shows that helium desorption at 500°C is very small, one may conclude that the observed nanostructures are bubbles filled by helium. This is further confirmed by the different shapes observed, suggesting that it is the entrapped helium pressure that at one time avoids nanostructure collapse and determines their shape.
Further annealing at 1000°C (sample C) promotes a rapid effusion of helium atoms that leave the bubbles and cease providing the inner pressure needed for further vacancy aggregation. Hence the voids (now out of equilibrium) either fully collapse or become so small to be hardly detectable by TEM (inset to Fig. 4.6 b).
Instead, if the initial annealing at 500°C is followed by a multi-step gradual heat treatment from 600°C to 1000°C (sample D), below 800°C helium may slowly outdiffuse from voids but does not appreciably leave the film. This is clearly confirmed by TPD showing how the effusion flux is smaller in this temperature range. Thus, helium remains available to enable both further nucleation and growth of bubbles. At higher temperatures ($\geq$ 800°C) helium finally outdiffuses from the film leaving behind the relatively large density of small voids observed by TEM (Fig. 4.6). In this picture it can be conclude that for sample D the void size and spacing are functions of the annealing temperature. In particular, while the NV diameter increases by increasing the annealing temperature, at the same time the mean distance between voids decreases while maintaining the porosity constant. This trend is confirmed in the literature for the single crystal case [115].
The behavior observed in sample B can also be explained in this framework. Here the single annealing at 1000°C causes the immediate effusion of helium, leaving too little time for vacancies to aggregate into large voids. In addition, in this case NVs are small enough to be subjected to the collapsing mechanism invoked for sample C. The resulting morphology is then characterized by smaller voids (Fig. 4.7 a), except for a very few large structures located near GBs (Fig. 4.7 b).

In summary, the parameters and mechanism which set the nanomorphology of these samples are:

1. helium implantation parameters (dose and energy) which set the voids distribution along the film thickness and the total void volume (hence the porosity)

2. thermal treatments performed after helium implantation that modify void dimensions and density through coalescence, repining, and collapse

3. helium outdiffusion, separately occurring from bubbles at $\geq 600°C$ and from the silicon lattice only at higher temperatures ($\geq 800°C$)

4. vacancy clustering, leading to the formation of voids only in the presence of helium filling the voids

5. void collapse (dependent on size) when helium leaves the bubbles

In addition, grain boundaries may cause the formation of irregularly shaped bubbles or voids as a result of the local strain field that may arise in the intergrain regions and of the local vacancy–GB equilibria there establishing.

Therefore it may be conclude that helium implantation followed by thermal treatments is a viable technique to create a tunable dispersion of NVs also in nanocrystalline silicon thin films.

4.5.2 Compatibility with Power Factor enhancement

From what discussed up to now, heat treatments promote three simultaneous diffusion processes, namely (a) vacancy diffusion, leading to the final formation of nanovoids; (b) boron diffusion, resulting in its segregation at grain boundaries (GBs) and then eventually to its precipitation as a second phase; and (c) helium outdiffusion from silicon. The three processes are expected to be characterized by different rates.
In this section the electrical and thermoelectric characteristics of sample

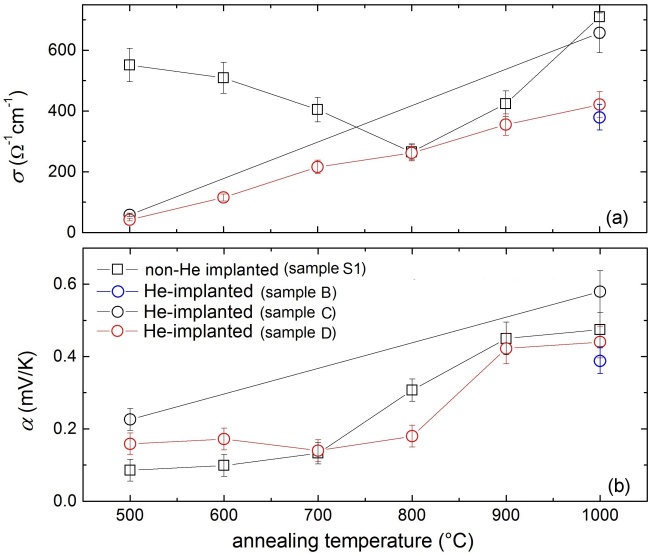

Figure 4.8: (a) Electrical conductivity and (b) Seebeck coefficient vs. annealing temperature for samples B, C, D (implanted with helium, see Tab. 4.1) and sample S1. Reproduced with permission from [11].

S1 (no He implanted) will be compared with sample B, sample C and sample D (Table 4.1).

The evolution of the Seebeck coefficient α in sample D showed a trend closely reminiscent of that observed in non-He-implanted (S1) samples (Fig. 4.8). Seebeck coefficient shows actually a rather abrupt increase upon annealing at 800°C, reaching a topmost value of 0.45 mV/K after being annealed at 1000°C. The electrical conductivity displays instead an almost linear increase with the annealing temperature, quite different from that observed in S1 specimens.

It is interesting to compare such a trend with that observed in sample C. While both σ and α after annealing at 500°C are similar in the two experiments, sample C shows an electrical conductivity at 1000°C closely comparable to that of the S1 samples; while sample D results in a final σ value about half of that observed in the absence of helium implantation. On the contrary, the final Seebeck coefficient for sample D is equal to that of the S1 material while sample C returns a final α value about 15% larger.

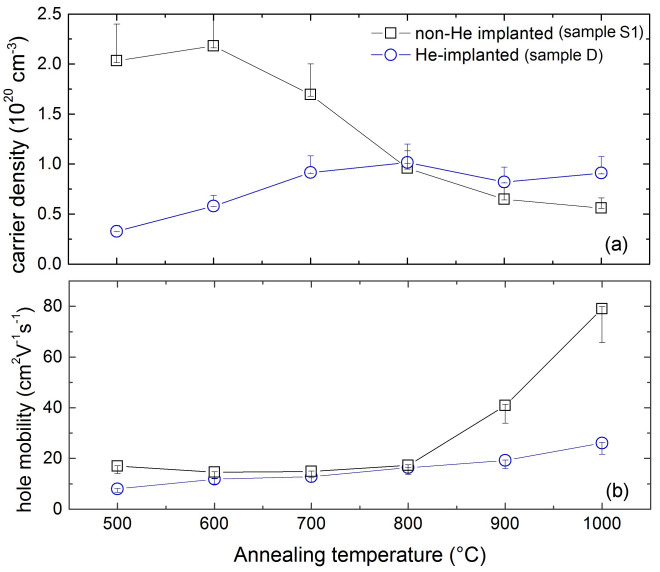

Figure 4.9: (a) Carrier density and (b) hole mobility vs. annealing temperature for sample S1 and D. Reproduced with permission from [11].

In addition, sample B subjected to one-shot annealing at 1000°C presents values of σ and α instead very close to those of sample D. To elucidate such differences, Hall effect measurements were carried out (Fig. 4.9). As expected, the steady increase of σ observed in all He–implanted samples is apparently caused by the regular increase of the hole mobility μ, changing by almost a factor of four from the as–implanted to the fully cured film. As of the carrier density, in S1 specimens, p reflected the diffusion–limited precipitation of boron from the supersaturated Si–B solid solution. A different $p(T_a)$ trend is observed in sample D, where actually p smoothly increase by a factor of five upon annealing up to 700°C, levelling at 1000°C to 10^{20} cm^{-3}, approximately twice the density of sample S1.

The set of evidences just reported confirms that film properties are controlled by the simultaneous occurrence of vacancy and helium diffusion, and of boron diffusion–limited precipitation, leading to the generation of nanovoids and to the formation of a SiB_x second phase.
In the longest processing sequence (sample D), the variation of the Seebeck

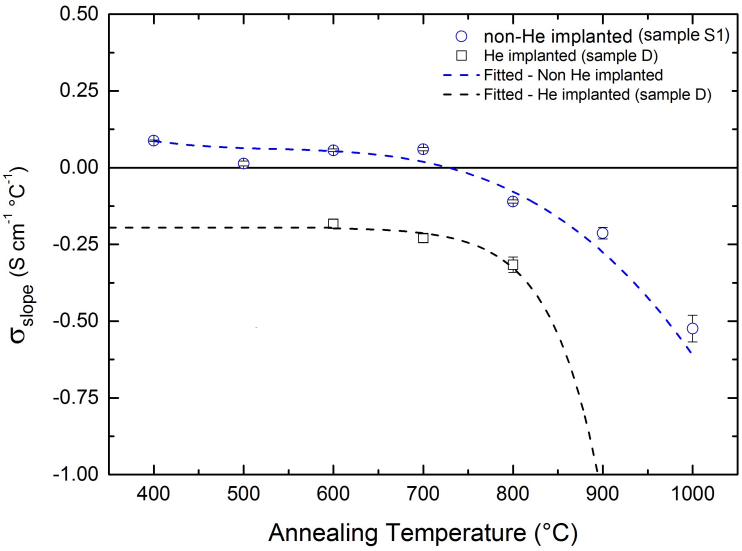

Figure 4.10: Slope of σ versus annealing temperature for sample S1 and D as resulting from measurements of electrical conductivity versus T.

coefficient basically reproduces that observed in S1 specimens submitted to the same annealing sequence. The concurrent increase of σ and α with the annealing temperature properly fits in the framework of carrier energy filtering in two-phase systems.

However the conductivity is smaller than in S1 samples so that a negative impact on the electrical transport properties due to the presence of NVs could be invoked. This assumption can be anyway excluded and the behaviour explained to be caused by a slower dopant segregation. Such conclusion relies on two main evidences: (1) the final carrier density for sample D is higher (approximately twice) than sample S1; (2) a different $\sigma(T)$ is observed (Fig. 4.10). In particular while S1 shows a metallic behaviour at all annealing temperatures, sample D presents a thermally activated behaviour for annealing temperatures lower than 700°C and a metallic behaviour for higher temperatures. This evidence calls for a hampered Boron segregation which leads to a slower second phase formation and a smaller increase of electrical mobility due to energy filtering. Possible explanations for such effect are: the well documented effect of NVs on

decreasing the boron diffusion coefficient [115]; or the formation of Boron-vacancies complexes during helium implantation. This hinders Boron segregation as high temperature annealing are needed to free boron atoms from complexes [125]. The latter explanation is compatible with the very low carrier density showed by sample D at low annealing temperature.

Concerning sample C, the shortest annealing cycle apparently leads to an increase of α over that observed in S1 films, calling for a mechanism which leads to an higher dopant segregation. Unfortunately Hall measurements for sample C are not available at this time. However, it may be conjectured that in the depletion region surrounding NVs a lower carrier density (and, as a result, a larger fraction of neutral dopants) should be found. The lower carrier density would lead to a larger Seebeck coefficient. Also, since ionized impurity-limited mobility linearly depends on the reciprocal carrier density [126], the reduction of p would be compensated by an increase of μ, thus justifying a conductivity comparable to that observed in S1 films.
The augmented dopant segregation could be related to the peculiar behaviour of sample C showed by TEM analysis in which NVs seem to collapse, disappearing during the annealing performed at 1000°C (Fig. 4.6).

Finally since sample B exhibits a behaviour very close to sample C, it confirms the trend showed by non helium implanted samples for which one-shot annealing at 1000°C leads to the same effects than annealing cycles between 500 and 1000°C.

Summarizing, helium implantation is compatible with the energy filtering effect observed in the nanocrystalline silicon thin films object of this thesis. However the high density of vacancies created by the implantation and their diffusion appear to interfere with Boron segregation and the second phase required for energy filtering. Further investigations are under way to elucidate such behaviour and there will be object of future works.

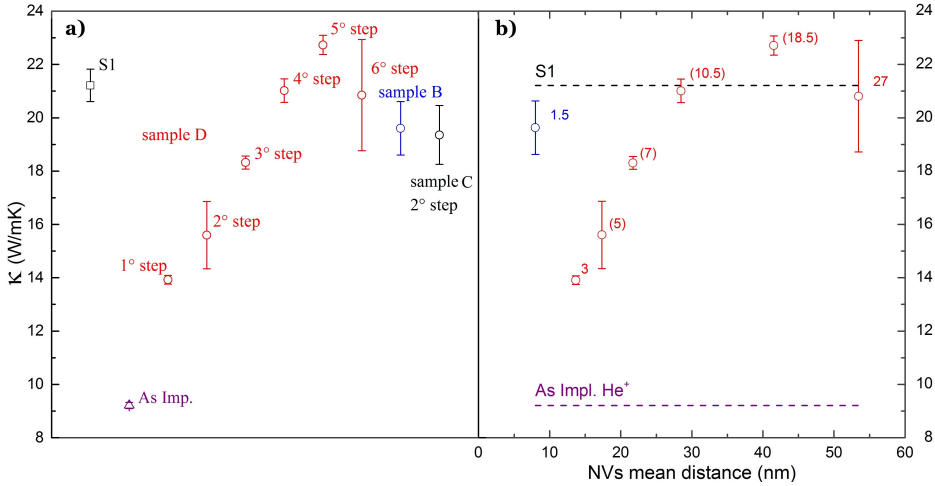

Figure 4.11: (a) Values of κ for samples: S1 (black square), B (blue circle), C - 2° step (black circle), D - all six steps (red circles) and as-implanted (purple triangle). (b) κ versus mean distance between voids for samples B (blue circle) and D (red circles). The labels are the detected or calculated (between brackets) mean void diameters expressed in nm. The dashed lines represent the measured κ for sample S1 and the as-implanted sample.

4.5.3 Thermal Characterisation

TDTR measurements were performed for the following batch of samples: sample S1 prior to any thermal annealing (which was taken as the reference sample); sample B; sample C (after the second annealing step); and sample D. The last one was analysed after any annealing step (500, 600, 700, 800, 900 and 1000°C). In addition, also the as-implanted sample prior to any thermal annealing was measured. In Fig. 4.11 TDTR results are showed.

Fig. 4.11a reports on κ absolute values. Sample S1 displays a thermal conductivity of 22.1 W/mK. This is compatible with what reported within the literature on polycrystalline silicon thin films [127, 128].
The effect of the helium implantation can be seen from the thermal conductivity measured on the as-implanted sample which results to be 9.2 W/mK. This κ decrement is what one would expect due to the huge density of vacancies created by the helium implantation.

For the thermally treated samples, the most straightforward result is for sample C, which shows a κ value just a little smaller (19.4 W/mK) than S1. Considering that thermal treatments were verified not to modify the grain size and orientation of the films (as discussed in section 3.2.3) it should be concluded that any variation on the thermal conductivity in helium implanted and treated samples have to be ascribed to the second phase formation and/or the presence of NVs.
TEM analysis showed that sample C after annealing at 1000°C (Fig. 4.6b) had almost no remaining voids thus it may be concluded that the small variation of κ for sample C is due only to the presence of the second phase.

Sample D shows instead a thermal conductivity spanning between 13.9 and 22.7 W/mK depending on the annealing cycle step. Starting from the as-implanted sample, thermal conductivity increases upon thermal treatments, reaching values around 22 W/mK for annealing temperatures higher than 700°C (steps 4, 5 and 6). This trend is compatible with the reorganization of the silicon structure (namely the vacancy aggregation) as a function of the thermal annealing, as shown by TEM analysis (Fig. 4.6a and c).
Therefore NVs impact on the thermal transport of sample D depending on their size and density. The high density of tiny voids showed after the first annealing step affects thermal conductivity more then the smaller density of larger NVs for subsequent annealing steps. This behaviour is quite normal considering NVs as phonon scattering centres. A decrease in the NVs density implies an increase in the distance between voids leading to a larger phonon MFP and thus higher conductivity.

On the contrary the thermal conductivity measured in resulting for sample B is not easily understandable. In fact even if, based upon TEM analyses, this sample exhibits the highest density of NVs (Fig. 4.7), its thermal conductivity is comparable to that measured on sample C, which does not show any void. Therefore the thermal properties of sample B appear to be insensitive to NVs.
This unexpected behaviour is further highlighted in Fig. 4.11b where the thermal conductivities of samples B and D are reported as a function of the mean NVs spacing. This spacing was determined by the analysis of

the TEM images available for the first and the last steps of the annealing cycle and for sample B. The other values were estimated by considering constant porosity and using literature data regarding the change in NV dimensions with thermal treatments for single crystal silicon [115]. The labels near data points display the average void diameter (estimated values are in brackets).
Therefore the correlation between κ and the phonon MFP showed by sample D seems to brake down for sample B. This can be explained considering that in these samples a decrease in the NV distance means also a decrease in the NV size. Since scattering centres can be effective only if their size are comparable to the phonon wavelength, it can be concluded that in sample B, NV sizes are too small to affect phonon transport. As reported in several computational studies, silicon thermal conductivity is due to phonons spanning a wide spectrum of phonon wavelength [129, 130]. Therefore one may speculate that for very small NV dimensions most of the phonons are not scattered by voids because they have wavelengths larger than the void dimensions. This is in very good agreement with several computational and theoretical studies recently appeared in literature regarding the frequency dependent nature of the phonon scattering [80, 131, 132], confirmed by very few experimental works [133].

Then it may be concluded that for very small NVs dimensions, the so-called "gray model" (which assume a constant phonon transmissivity), is a misleading tool in order to describe porous systems, and a frequency dependent approach should be preferred.

Summarizing, the thermal characterisation carried out on nanocrystalline silicon thin films, showed that:

1. the second phase generated by the thermal annealing have just a marginal reducing effect on the thermal conductivity of the samples

2. NVs can impact on the samples thermal transport properties decreasing thermal conductivity depending on their size and spacing

3. κ decreases almost linearly by decreasing NV spacing; however since also NV diameter decreases, because of the constant porosity, the trend breaks-down for small NV diameters

4.5.4 Figure of merit evaluation

Knowing PF and κ one can evaluate the room temperature figure of merit of the samples. It has to be pointed out that this evaluation is based on measurements performed along two different sample directions. Actually, while PF was measured in the in-plane direction, κ was measured in the through-plane direction. In any case an estimation of ZT would return important information on the samples properties.

Fig. 4.12 reports a plot of κ vs. PF for samples B, C, and D compared to typical values for polycrystalline silicon thin films, from literature [12, 13, 14].
From this graph two major conclusions could be drawn.
First, samples analysed in this study exhibit lower thermal conductivities,

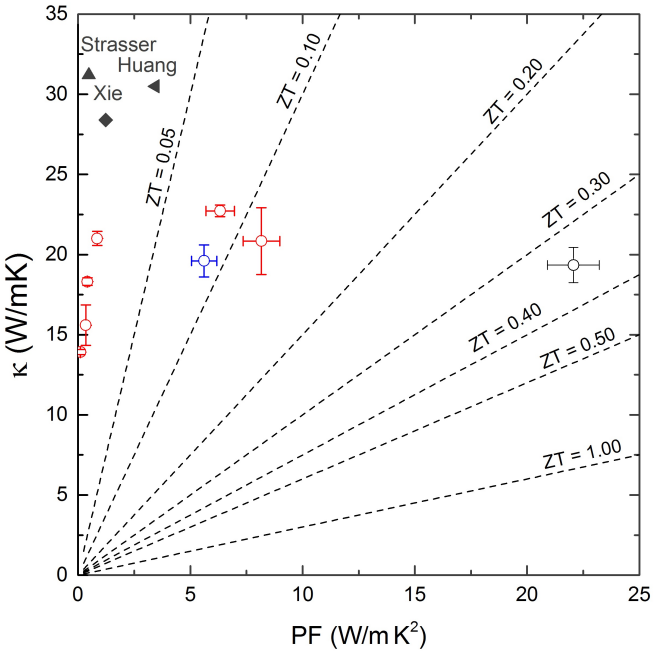

Figure 4.12: Plot of κ versus PF for samples B (blue circle), C (black circle) and D (red circles) and their comparison with ZT values found in literature: Xie et al. [12], Huang et al. [13] and Strasser et al. [14].

and in some cases (for high annealing temperatures) higher PFs. This leads to ZT enhancement of up to one order of magnitude.
Secondly, highest ZTs values were measured in case of thermal conductivities comparable to sample S1. Thus the contribution of NVs is not helping the ZT enhancement. This fact is basically caused by a mismatch between the PF and κ behaviours upon thermal annealing, since an increase of PF requires high temperatures annealing, which in turn lead to a decrease in the NV effect on κ. Therefore ZT are bound to values lower than 0.4.

Solutions to avoid this mismatch can be though, e. g. performing a first high temperature thermal annealing prior to the helium implantation and then a second annealing at lower temperatures in order to reach the best NV dimensions, thus maximizing the figure of merit.

4.6 Summary

In this chapter a deep study on the possibility of using helium implantation followed by thermal annealing in order to modulate the thermal properties of nanocrystalline silicon thin film was reported.

It was showed that helium implantation can be used in order to create a tunable dispersion of NVs within the films. Furthermore it was demonstrated that while the final film porosity is set by the implantation parameters, the voids dimension and spacing can be changed by thermal annealing.

The compatibility between the PF enhancement process and the creation of NVs was then tested, showing that implantation can influence Boron segregation and the subsequent second phase formation needed to reach high PF values.

Finally the NV impact on the film thermal conductivity was studied as a function of the thermal treatments. This work showed that κ can be decreased almost linearly by decreasing the NV spacing down to a minimum value for which the frequency dependent behaviour of the scattering

mechanism disallows further κ reduction.

Chapter 5

Conclusions

In this PhD work the main activity was focused on a non-toxic abundant nanostructured material for thermoelectric applications, based on nanocrystalline silicon thin films highly doped with boron. The work was organised in two main activities.

In the first the possibility to induce an enhancement of the film power factors, due to a simultaneous increase of the Seebeck coefficient and of the electrical conductivity, was demonstrated. These enhancements have been discovered to be caused by the dopant segregation (induced by thermal annealing) and the creation of a second phase, which led to an energy filtering effect. This evidence along with a computational work led to a model describing this phenomenon. The model was found to require the concurrency of the following features: (1) a grain size enabling only partially energy-relaxed carrier transport; and (2) the presence of suitable energy filtering barriers (in our case the boron-rich second phase) preventing slow carriers from participating in the energy and charge transport. Energy filtering in single crystals and in relatively large-grained polycrystalline materials were demonstrated instead to only partially compensates the reduction of σ resulting from a decrease of the carrier density. In fact no simultaneous increase of the thermopower and of the electrical conductivity was found in these systems, as charge transport occurs in the diffusive regime, so that carrier relaxation dumps the effect of energy fil-

tering.

In the second part of this thesis it was demonstrated that a tuning of the thermal properties of silicon thin film can be made through the formation of a dispersion of nanovoids (NVs). NVs were obtained using a technique well know for single crystal silicon, based upon helium implantation and subsequent thermal annealing.
This study allowed for the first time the determination of the main parameters and mechanisms which set the NVs nanomorphology in polycrystalline silicon thin films: (1) helium implantation parameters (dose and energy) which set the void distribution along the film thickness and the porosity; (2) thermal treatments performed after helium implantation that modify void dimensions and density through coalescence, ripening, and collapse; (3) helium outdiffusion, separately occurring from bubbles at ≥ 600°C and from the silicon lattice only at higher temperatures (≥ 800°C); (4) vacancy clustering, leading to the formation of bubbles only in the presence of helium filling it; (5) void collapse (dependent on size) when helium leaves the bubbles. In addition, grain boundaries were found to cause the formation of irregularly shaped bubbles or voids as a result of the local strain field that may arise in the intergrain regions and of the local vacancy–GB equilibria there establishing.
Therefore helium implantation followed by thermal treatments were demonstrated to be a viable technique to create a tunable dispersion of NVs in nanocrystalline silicon thin films.
Moving from this evidence, the work was then focused on the study of NV effect on thermal and thermoelectric properties.
Firstly the thermoelectric properties were characterised to test the compatibility of NVs with the energy filtering effect exhibited by those structures. The results showed that helium implantation does not prevent the simultaneous increase of α and σ. However the high density of vacancies created by the helium implantation and their diffusion appeared to interfere with Boron segregation, and the second phase formation required for the energy filtering effect.
The thermal properties of the samples were then measured and analysed as a function of the void morphology. This characterisation showed that: (1) the second phase generated by the thermal annealing have just a marginal

reducing effect on the thermal conductivity of the samples; (2) NVs impact on the sample thermal transport properties, decreasing thermal conductivity depending on their size and spacing; (3) κ decreases almost linearly by decreasing NV spacing, however since also NV diameter decreases, because of the constant porosity, the trend breaks down for small NV diameters, calling for the frequency dependent behaviour of the scattering mechanism reported recently by several theoretical works.
Finally knowing PF and κ it was possible to evaluate the room temperature figure of merit. The results showed that: (1) the samples analysed in this thesis exhibit ZT values of up to one order of magnitude higher than the literature; (2) the highest ZTs values were measured in case of sample in which the NV effect on the thermal conductivity was negligible. This evidence was found to be caused by a mismatch between the PF and κ behaviours upon thermal annealing, since an increase of PF requires high temperatures annealing, which in turn lead to a decrease in the NV effect on κ. Therefore ZT was found to be bound to values lower than 0.4.

Appendix A

Hybrid Thermoelectric - Photovoltaic Devices

From the analysis of the energy fluxes within a single junction photovoltaic device it is easy to understand that its largest efficiency limitation is due to the unavoidable decoupling between the energy source (the Sun) and the absorbing material. Actually, while the solar spectrum is continuous over a wide range of frequencies, the device has the capability of efficiently converting photons only at the frequency corresponding to the energy gap (E_g) of its absorbing material. The remaining part of the spectrum is either fully not absorbed ($E < E_g$) or absorbed but partially converted into heat ($E > E_g$). Such energy losses (along with other optical and electrical losses) constrain the photovoltaic (PV) efficiency (η_{PV}) under the Shockley-Queisser (SQ) limit [134], with values around 30% depending on the absorber E_g [135].
A possible solution to overcome this limit is the implementation of multi-junction solar cells in which more materials operate as absorbers. On these premises many different devices have been proposed in literature (the so–called *Third Generation PV*). They include tandem cells, three– and four– junction solar cells, up–down conversion devices, and light con-

centrators. More recently, an alternative approach has become popular. Energy wasted by the single junction PV device is converted into useful work by heat recovering [24, 136, 137, 32, 138]. Lets call this class of devices: *Hybrid Thermo–Photovoltaic systems* (HTPVs). The actual way they convert heat into useful work may differ.

In this thesis the work was focused on a special sub–class of HTPV devices, wherein a PV cell is both thermally and electrically coupled to a thermoelectric generator (TEG) in series. We will refer to them as hybrid thermoelectric-photovoltaic devices (HTEPVs).
In the following sections a model to predict the performances of HTEPV devices will be proposed. Starting from the SQ limit the maximum device efficiency as a function of both E_g and T_{cell} will be computed in two different configurations. The first just coupled the solar cell to the thermoelectric device; while the second made use of an additional absorbing layer to partially convert also the low-frequency tail of the solar spectrum.

A.1 Losses in single junction PV

Manifestly enough, to increase the conversion efficiency in single–junction solar cells a proper definition and identification of all sources of loss is needed. The efficiency of a generic photovoltaic system is simply the ratio between the output and input power, namely

$$\eta_{PV} \equiv \frac{P_{out}}{P_{in}} = \frac{V_{oc} J_{sc} FF}{\Phi_{Sun}} \tag{A.1}$$

where V_{oc}, J_{sc}, and FF are respectively the open circuit voltage, the short circuit current density, and the filling factor; while Φ_{Sun} is the solar radiation intensity. From a thermodynamic point of view, the maximum efficiency η_C achievable in a solar cell equals the Carnot efficiency, i.e. $\eta_C = 1 - T_{cell}/T_{Sun}$, where T_{cell} is the device (cold side) temperature and T_{Sun} is the Sun temperature. According to Landsberg [139] this formula should be modified taking into account the non–zero radiation emitted by the absorber:

$$\eta_{max} \equiv \frac{P_{max}}{P_{in}} = 1 - \frac{3}{4}\left(\frac{T_{cell}}{T_{Sun}}\right) + \frac{1}{3}\left(\frac{T_{cell}}{T_{Sun}}\right)^4 \tag{A.2}$$

Taking $T_{\text{cell}} = 300$ K and $T_{\text{Sun}} = 6000$ K one gets an efficiency of 93.33%. However, Shockley and Queisser [134] showed how in a single–junction device the actual achievable efficiency is bound to much lower values due to several types of energy losses. This evaluation defines the so-called SQ limit.
It may be useful to group the energy loss as follows:

1. **Optical Losses (L_1):**
   (a) contact grid shadow
   (b) radiation reflection
   (c) spurious absorptions
2. **Source-absorber decoupling losses (L_2):**
   (a) non–absorbed photons with $E < E_{\text{g}}$
   (b) thermalization of hot carriers (photons with $E > E_{\text{g}}$)
3. **Thermal losses (L_3)**, namely the Joule effect
4. **Electrical losses (L_4):**
   (a) non–unitary quantum efficiency
   (b) material defects
5. **Recombination losses (L_5):**
   (a) radiative recombination
   (b) non radiative recombination

Since such losses occur sequentially, the actual output power P reads

$$P = P_{\text{max}} \prod_{n=1}^{5} L_n \tag{A.3}$$

Thus the efficiency η accounts to

$$\eta = \frac{P}{P_{\text{in}}} = \eta_{\text{max}} \prod_{n=1}^{5} L_n \tag{A.4}$$

The SQ limit neglects optical, thermal and electrical losses, thus accounting only for losses of type (2) and (5). Furthermore, it assumes that T_{cell} equals room temperature. In next section the SQ limit will be rewritten relaxing such assumption namely letting T_{cell} be larger than 300 K to evaluate the maximum achievable efficiency for a single junction PV cell as a function of its actual operating temperature. Such calculation is required to properly model its contribution to the overall efficiency of the hybrid device.

A.2 Temperature Dependence of the SQ Limit

Following Shockley and Queisser [134] lets assume that: (i) the solar cell is oriented normal to the sunlight beam; (ii) all photons with energy larger than the absorber energy gap are absorbed, while photons with smaller energies produce no effect; (iii) the device has unitary quantum efficiency, i.e. any absorbed photon generates an electron–hole pair at a voltage $V_\gamma = E_\gamma/q$ (where E_γ is the photon energy and $-q$ is the electron charge); (iv) the only mechanism of electron-hole recombination is radiative.

In order to compute the maximum PV efficiency the ASTM data for the AM1.5 solar spectrum with an intensity of 1000 W/m^2 [140] was used (Fig. A.1 (a)), and with cutoff energies E_{min}= 0.30 eV and E_{max}= 4.4 eV. The distribution function of the incident photon flux $n_\gamma(E_\gamma)$ (in eV^{-1}cm^{-2}s^{-1}) is then obtained by dividing the spectral intensity by the photon energy. In view of assumptions (i) and (ii) one evaluates the fractions of energy loss due to photons with $E < E_{\text{g}}$

$$L_{2\text{a}}(E_{\text{g}}) = \frac{\int_{E_{\text{min}}}^{E_{\text{g}}} n_\gamma(E_\gamma) E_\gamma \mathrm{d}E_\gamma}{\int_{E_{\text{min}}}^{E_{\text{max}}} n_\gamma(E_\gamma) E_\gamma \mathrm{d}E_\gamma} \tag{A.5}$$

finding that, as expected, $L_{2\text{a}}$ increases almost linearly with E_{g}, spanning from $\approx$ 16% for bulk silicon to more than 50% in the case of thin film technologies (Fig. A.1(b)).

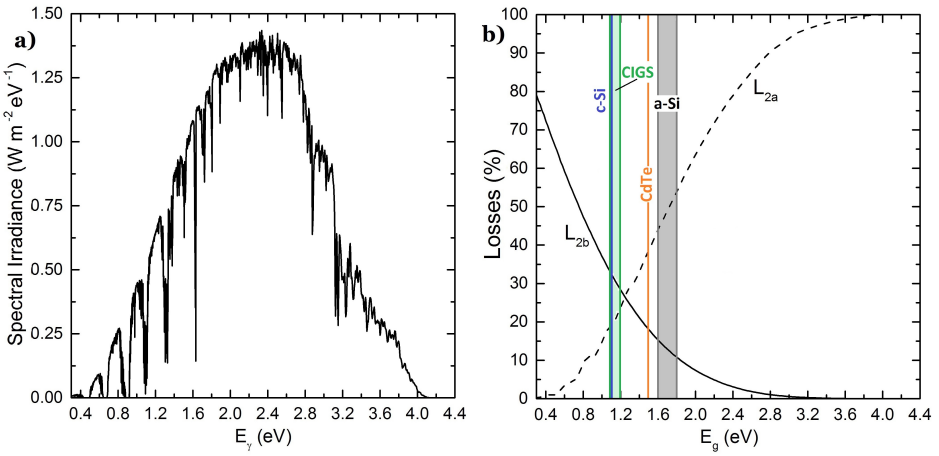

Figure A.1: (a) AM1.5 solar spectrum used for all calculations reported in this paper; (b) Energy losses L_{2a} and L_{2b} vs. the absorber material energy gap. E_g values of some PV materials are highlighted.

And to photons with $E > E_g$ (causing carrier thermal relaxation)

$$L_{2b}(E_g) = \frac{\int_{E_g}^{E_{max}} n_\gamma(E_\gamma)(E_\gamma - E_g)\mathrm{d}E_\gamma}{\int_{E_{min}}^{E_{max}} n_\gamma(E_\gamma)E_\gamma \mathrm{d}E_\gamma} \tag{A.6}$$

These quantities are displayed as a function of the energy gap of the absorber material in Fig. A.1(b). For silicon, $L_{2b} \approx 30\%$ while smaller values (down to 10%) are found in materials with larger E_g. Note that $L_{2b}(E)$ has a larger slope than $L_{2a}(E)$.
In both equation the overall incoming power per unit area has been rewritten as $\Phi_{Sun} = \int_{E_{min}}^{E_{max}} n_\gamma(E_\gamma)E_\gamma \mathrm{d}E_\gamma$.

The electric power produced by a solar device is known to decrease with its working temperature. This is due to the increase of the electron–hole recombination rate. As a result, a larger dark saturation current is expected when the cell temperature increases, affecting in turn V_{oc} [135]. The relationship between V_{oc} and T_{cell} is approximately linear. Since the short–circuit current J_{sc} is instead just marginally affected by the increase

of T_{cell}, the output power $P_{\text{PV}}^{\text{out}}$ is also proportional to T_{cell}^{-1} — and so is its efficiency η_{PV}. This decrease of the PV cell performance was widely confirmed by experimental works [141, 142, 143].
Thus, under Standard Test Condition (STC, namely solar radiation flux of 1000 W/m^{-2}, A.M. 1.5, temperature of 25 °C).

$$\eta = \eta_{\text{STC}} - (T_{\text{cell}} - 25°C)\gamma_{rel} = \eta_{\text{STC}} - L_{2\text{c}} \tag{A.7}$$

where it has been defined the coefficient $L_{2\text{c}}$, essentially the percentage of the solar cell efficiency lost because to the temperature increase.
Temperature coefficients γ_{rel} for some materials used in PV technology can be found in the literature [141].
Several methods have been proposed for a proper determination of T_{cell} [143].The most common approach accounts for an energy flux balance between the incoming and the outgoing power in the PV system, leading to

$$\tau\alpha\Phi_{\text{Sun}} = U_{\text{L}}(T_{\text{cell}} - T_{\text{a}}) \tag{A.8}$$

where τ and α are respectively the glazing transmittance and the PV layer absorbance; T_{a} is the ambient temperature; and U_{L} is the thermal loss coefficient, which has the dimensions of a thermal conductance. Considering the cell heating process as fully due to the thermalization of the hot photogenerated carriers, Eq. (A.8) reads

$$L_{2\text{b}}\Phi_{\text{Sun}} = U_{\text{L}}(T_{\text{cell}} - T_{\text{a}}) \tag{A.9}$$

so that

$$L_{2\text{c}} = L_{2\text{b}}\Phi_{\text{Sun}}\frac{\gamma_{\text{rel}}}{U_{\text{L}}} \tag{A.10}$$

The only unknown term in Eq. (A.10) is U_L. As a matter of fact, a PV device exchanges energy with the environment radiatively and convectively (at least) both from the top and the bottom parts of the module [144]. As a result, wind speed, the type of mounting, the materials used in the top and bottom finalizing layers, and the way the cell is encapsulated concur to set U_{L}. A range of U_L values for different types of PV configurations can be found in the literature [143, 142].
Fig. A.15(a) displays the dependency of T_{cell} upon the absorber energy gap for different values of U_{L}. As can be seen, T_{cell} decrease for increasing

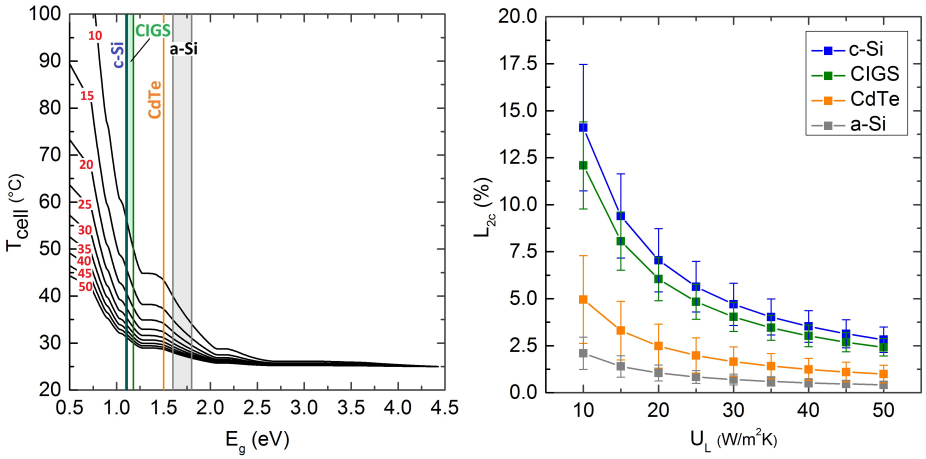

Figure A.2: a) Plot of T_{cell} vs. the absorbing material E_{g} for different values of U_{L} between 10 and 50 W m^{-2}K^{-1}. b) Values of $L_{2\text{c}}$ vs. U_{L} for four types of absorbing materials. Reproduced with permission from [15].

E_{g}, because of its proportionality to $L_{2\text{b}}$. This dependency is much more relevant for small U_{L} while it becomes negligible for large U_{L} because of an higher heat flux between the cell and the environment. A likely trend is shown in Fig. A.15(b), reporting the dependence of $L_{2\text{c}}$ upon U_{L} for four given absorbers.

According to assumption (iii) is possible to evaluate the temperature effect on the cell performances by calculating the radiative recombination. First for the spectral power above the energy gap is needed

$$\Phi_{\text{above}}(E_{\text{g}}) = \int_{E_{\text{g}}}^{E_{\text{max}}} n_{\gamma}(E_{\gamma}) E_{\gamma} \mathrm{d}E_{\gamma} \tag{A.11}$$

This parameter contributes to carrier generation and sets the current density produced by the device. Radiative recombination depends upon the probability of collisional events between holes and electrons, then depending on the difference between hole and electron quasi-fermi levels. Thus

the current density J generated by the solar device can be written as

$$J = q\left\{N_{\gamma,\text{above}}(E_\text{g}) - r_0\left[\exp\left(\frac{qV}{k_\text{B}T_\text{cell}}\right) - 1\right]\right\} \tag{A.12}$$

where

$$N_{\gamma,\text{above}}(E_\text{g}) = \int_{E_\text{g}}^{E_\text{max}} n_\gamma(E_\gamma)\text{d}E_\gamma, \tag{A.13}$$

k_B is the Boltzmann constant, V is the external bias on the junction, and r_0 is the radiative recombination rate when there quasi-fermi energies equal each other [145]:

$$r_0 = \frac{2\pi}{c^2h^3}\int_{E_\text{g}}^{E_\text{max}} \frac{E_\gamma^2\text{d}E_\gamma}{\exp\left[\left(E_\gamma - qV\right)/k_\text{B}T_\text{cell}\right]} \tag{A.14}$$

Using Eq. A.12 one can find the maximum power output $P_\text{PV}^\text{out}(E_\text{g})$ by maximizing $J \times V$ for a given E_g. The ratio between $P_\text{PV}^\text{out}(E_\text{g})$ and Φ_sun returns the cell maximum efficiency, namely the SQ limit, as a function of E_g and T_cell. Furthermore, J_sc and V_oc can be obtained from Eq. A.12, the former by setting $V = 0$ and the latter by setting $J = 0$. This will eventually lead to compute the so–called filling factor FF by Eq. A.1.

It may be worth noting that the present calculation (as the original SQ scheme) neglects any temperature profile within the PV cell. Actually, although there is clearly a temperature gradient between the front and the back of the cell, introducing such correction leads to very minor numerical changes in the final result as in all equations T_cell always appears within Arrenhius–like terms (e.g. $\exp\left(E_\gamma - qV\right)/k_\text{B}T_\text{cell}$) but in Eq. A.9. Since it is easy to verify that temperature differences up to some tens of kelvins lead to numerical corrections of less than 1 % in all Arrhenius terms, we will safely and consistently take T_cell as the temperature of the cell back, and will keep disregarding temperature gradients moving from the back to the front of the PV cell.

One can now use the explicit dependence on T_cell (Eqs. A.12 and A.14) to plot the SQ maximum efficiency $\eta_\text{PV}(E_\text{g}, T_\text{cell})$. Fig. A.3(a) shows $\eta_\text{PV}(E_\text{g}, T_\text{cell})$ for E_g and T_cell ranging between 0.5 and 2.5 eV and between

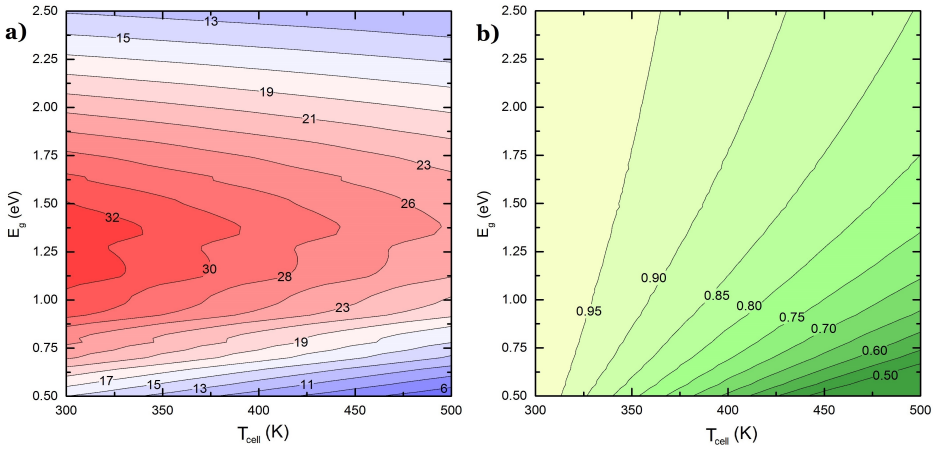

Figure A.3: SQ limit versus temperature. (a) Maximum PV efficiency (%) as a function of E_g and T_{cell}. (b) Same as (a) but normalized to the PV efficiency for T_{cell}=300 K.

300 and 500 K, resp.. The calculation returns that the maximum efficiency at 300 K is $\approx$ 33.6 % at $\approx$ 1.34 eV. This is in good agreement with the literature [146].

For any E_g we observe that $\eta_{PV}(E_g, T_{cell})$ decreases when the temperature increases. The decrease is steeper for small gaps. This trend is easily understood considering that for small gaps the probability of radiative recombination is higher and then the maximum efficiency shifts towards higher E_g for increasing T_{cell}. This feature is even more evident when plotting the ratio $\eta_{PV}(E_g, T_{cell})/\eta_{PV}(E_g, 300\ K)$ [Fig. A.3(b)]. Thus one may conclude that while it is true that the best achievable efficiency occurs for E_g around 1.3 eV, the performances deteriorate much faster with the T_{cell} for higher E_g. As we will see, this is actually the key point to evaluate when coupling in HTEPV can be beneficial.

A.3 HTEPV device modelling

As already mentioned, in HTEPV devices a TEG is basically connected thermally and electrically in series to the PV stage. In what follows two

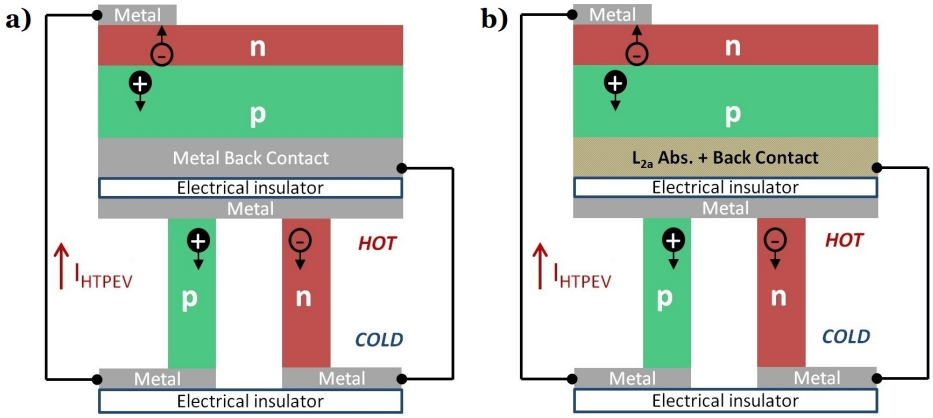

Figure A.4: Schematics of the device structures discussed in this work. (a) Case 1, in which the TEG is just placed underneath the solar cell and is electrically connected to it; (b) Case 2, where also the portion of the spectrum with $E_\gamma < E_g$ (L_{2a}) is recovered by introducing an additional absorbing layer.

different device structures will be discussed. In the first structure (hereafter Case 1) the TEG is just placed underneath the solar cell and is electrically connected to it (Fig. A.4(a)). Therefore T_{cell} follows from Eq. A.9 and the only part of the spectrum that can be recovered by the TEG is $L_{2b}(E_g)$.

Instead, in the second construction (Case 2) we recover also the portion of the spectrum with $E_\gamma < E_g$ by adding a layer acting as a black body and capable to convert this part of the spectrum into heat [cf. Fig. A.4(b)]. Therefore the power fraction recovered by the TEG is $L_{2a}(E_g) + L_{2b}(E_g)$ and Eq. A.9 has to be modified as

$$[L_{2a}(E_g) + L_{2b}(E_g)]\,\Phi_{sun} = U_L\,(T_{cell} - T_a) \tag{A.15}$$

that sets ideal heat dissipation conditions. Thus the TEG will convert the heat flowing trough its thermoelectric elements working between T_{cell} and T_a. The output power reads then

$$P_{TEG}^{out} = \eta_{TEG} L_{2b}(E_g) \Phi_{sun} \tag{A.16}$$

for Case 1 and

$$P_{\mathrm{TEG}}^{\mathrm{out}} = \eta_{\mathrm{TEG}} \left[L_{2\mathrm{a}}(E_{\mathrm{g}}) + L_{2\mathrm{b}}(E_{\mathrm{g}}) \right] \Phi_{\mathrm{sun}} \tag{A.17}$$

for Case 2.

In both equations η_{TEG} is given by

$$\eta_{\mathrm{TEG}} = \left(1 - \frac{T_{\mathrm{a}}}{T_{\mathrm{cell}}} \right) \frac{\sqrt{1 + Z\bar{T}} - 1}{\sqrt{1 + Z\bar{T}} + T_{\mathrm{a}}/T_{\mathrm{cell}}} \tag{A.18}$$

where ZT is the thermoelectric figure of merit and $\bar{T} = (T_{\mathrm{cell}} + T_{\mathrm{a}})/2$. Thus

$$\eta_{\mathrm{TEG}}^{\mathrm{out}} = \frac{P_{\mathrm{TEG}}^{\mathrm{out}}}{\Phi_{\mathrm{sun}}} = \begin{cases} \eta_{\mathrm{TEG}} L_{2\mathrm{b}}(E_{\mathrm{g}}) & \text{Case 1} \\ \eta_{\mathrm{TEG}} \left[L_{2\mathrm{a}}(E_{\mathrm{g}}) + L_{2\mathrm{b}}(E_{\mathrm{g}}) \right] & \text{Case 2} \end{cases} \tag{A.19}$$

and the hybrid device efficiency reads

$$\eta_{\mathrm{HTEPV}} = \frac{P_{\mathrm{PV}}^{\mathrm{out}} + P_{\mathrm{TEG}}^{\mathrm{out}}}{\Phi_{\mathrm{sun}}} = \begin{cases} \eta_{\mathrm{PV}} + \eta_{\mathrm{TEG}} L_{2\mathrm{b}}(E_{\mathrm{g}}) & \text{Case 1} \\ \eta_{\mathrm{PV}} + \eta_{\mathrm{TEG}} \left[L_{2\mathrm{a}}(E_{\mathrm{g}}) + L_{2\mathrm{b}}(E_{\mathrm{g}}) \right] & \text{Case 2} \end{cases} \tag{A.20}$$

A.4 Results and Discussions

In what follows all results are computed considering TEG material pairs having ZT=1.

A.4.1 Direct Coupling (Case 1)

The case of no extra absorbing layer HTEPV, is reported in Fig. A.5. Fig. A.5(a) shows the TEG output efficiency as a function of E_{g} and T_{cell}. In this configuration the TEG only converts the portion of the spectrum above the gap of the absorber. Thus $\eta_{\mathrm{TEG}}^{\mathrm{out}}$ increases for decreasing E_{g}.

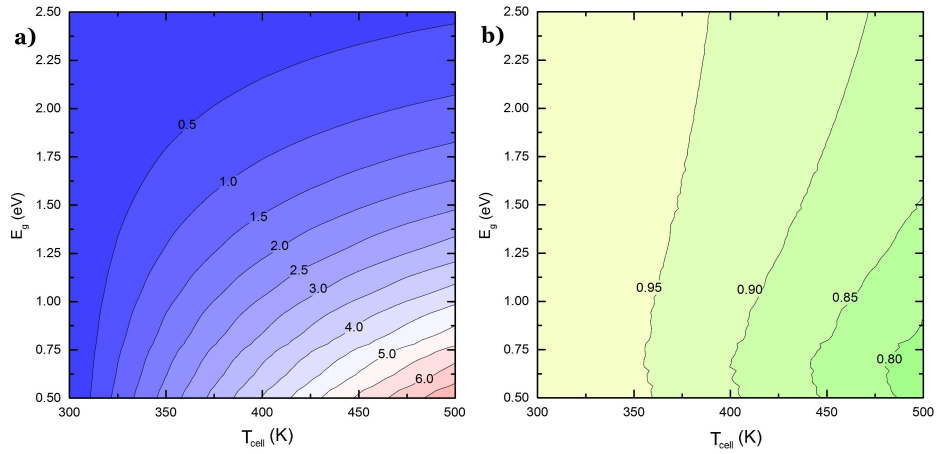

Figure A.5: HTEPV efficiency: CASE 1. (a) TEG efficiency (%) vs. E_g and T_{cell}. (b) HTEPV efficiency vs. E_g and T_{cell}, normalized to the PV efficiency for T_{cell}=300 K.

Instead, and manifestly enough, for any given E_g we observe η_{TEG}^{out} to increase with T_{cell}.

Fig. A.5(b) shows instead the HTEPV efficiency normalized to η_{PV} at 300 K. It shows that the most important effect of the TEG stage is to mitigate the decrease η_{PV} with increasing T_{cell}. This effect is more evident for small E_g, that is when the TEG contribution to the total efficiency is larger. Therefore the HTEPV device performs better than the PV alone, especially for small energy gaps. However, considering the range of temperatures normally reached by a solar cell under illumination (320 - 350 K [142]), the advantage seems unlikely to justify the effort needed to add the TEG stage.

A.4.2 Use of an Intermediate Absorbing Layer (Case 2)

In the presence of an extra absorbing layer able to covert the sub-gap fraction (L_{2a}) of the solar spectrum, the cell temperature is set by both L_{2a} and L_{2b}. Fig. A.6(a) shows the TEG output efficiency as a function of E_g and T_{cell}. In this case for small T_{cell}, η_{TEG}^{out} stays nearly constant for

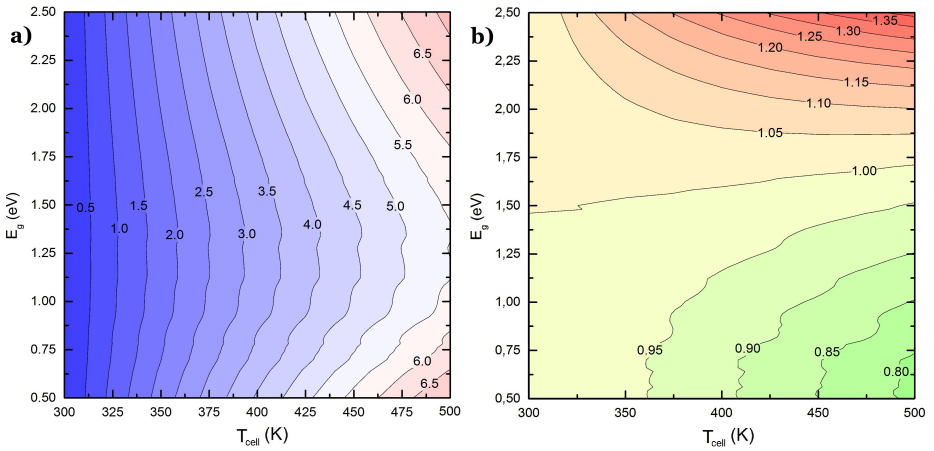

Figure A.6: HTEPV efficiency: Case 2. (a) TEG efficiency (%) vs. E_g and T_{cell}. (b) HTEPV efficiency vs. E_g and T_{cell}, normalized to the PV efficiency for T_{cell}=300 K.

any E_g, with a shallow minimum around 1.25 eV at high temperatures. The difference between minimum and maximum η_{TEG}^{out} values increases by increasing T_{cell}.

Fig. A.6(b) shows instead the HTEPV efficiency normalized to η_{PV} at 300 K. While for small E_g the situation is similar to that seen in Fig. A.5(b), new interesting features show up for intermediate and wide energy gaps. In fact in this region $\eta_{TEG}^{out}/\eta_{PV}(E_g, 300\ K)$ displays values larger than one. This means that in that range of energy gaps the HTEPV device performs better than the PV in its best scenario (namely for $T_{cell} = 300$ K). The lowest E_g for which this happens is around 1.50 eV at low temperatures and the threshold E_g increases up to ≈ 1.75 eV at 500 K. Therefore it may be concluded that in this configuration the TEG devices is worth being implemented to achieve higher efficiencies than those provided by standard single-junction solar cells with $E_g > 1.5$ eV. This implies that a TEG stage may also enable the use of wide-bandgap PV materials that are normally not considered in PV energy conversion because of their low intrinsic performances.

A.4.3 Evaluation of U_{L}

In this section an evaluation of which would be the overall thermal conductance between the PV cell and the environment in order to provide beneficial hybridization in HTEPV devices will be addressed. Knowing this, it will be consequently possible to make an evaluation on the ideal TEG thermal resistance. Since CASE 2 is the only one which exhibited normalized efficiencies higher than one we will focus our discussion on this system.

Firstly we need to select from Fig. A.6(b) a range of values (E_{g} and $\mathrm{T_{cell}}$) that we will define as the HTEPV best case. Within the region which shows $\eta^{\mathrm{out}}_{\mathrm{TEG}}/\eta_{\mathrm{PV}}(E_{\mathrm{g}}, 300K) > 1$, a reasonable range of values seems to be the one defined by: $\mathrm{T_{cell}}$ = 375 - 425 K and E_{g} = 2.0 - 2.5 eV. Within these parameters the absolute HTEPV efficiency ranges between 16 and 24% (1.06 - 1.3 if normalized).

Then using Eq. A.15 one can determine which are the U_{L} needed in order to have a $\mathrm{T_{cell}}$ ranging between 375 and 425 K. The equation returns that the overall thermal conductance should be between 6 and 12 $\mathrm{W/m^2K}$. Now considering that for a free standing PV module working under standard operating conditions the medium thermal resistance (the inverse of the conductance) with the environment is reported to be: $R^{fs}_{\mathrm{PV}} \simeq 0.021$ $\mathrm{m^2K/W}$ [143] we can roughly estimate that the TEG thermal resistance (R_{TEG}) should be between 0.06 and 0.14 $\mathrm{m^2K/W}$. In fact R_{TEG} follows by

$$\frac{1}{U_{\mathrm{L}}} = R^{fs}_{\mathrm{PV}} + R_{\mathrm{TEG}} \tag{A.21}$$

which is approximately one order of magnitude higher than what one can find in the actual thermoelectric devices commercially available. Therefore considering no change in the geometry of thermoelectric elements a smaller number of them per unit of area, respect to standard TEG is needed in order to reach the desired range of temperatures. This is in accordance with what reported recently in literature [24] about the need of thermal concentration in thermoelectric solar devices. However one should also guarantee a high thermal flux, between the device and the environment, avoiding the drift of the TEG cold junction temperature, towards T_{cell}. Therefore, in general, a proper thermal optimization is needed to maximize the hybrid device performances.

Furthermore this optimization has to be complemented with an electrical hybridization analysis (problem raised recently in [138]) to properly design thermoelectric modules reaching the best hybridization conditions.

A.5 Summary and Conclusions

In appendix it has been proposed a model to predict the performances of HTEPV devices in two different configurations. The first just coupled the solar cell to the thermoelectric device; while the second made use of an additional absorbing layer to partially convert also the low-frequency tail of the solar spectrum.
Moving from an extension of the SQ limit it was possible to compute the maximum solar cell efficiency as a function of both E_g and T_{cell}. This has led to the evaluation of the hybrid device performances as a function of the same parameters. The analysis lead to the conclusion that in the first class of HTEPV devices the TEG stage only mitigates the standard decrease of the PV efficiency for increasing T_{cell}, suggesting that in this configuration HTEPV devices are unlike to be a convenient option. The situation were found to be dramatically different in the second case, where the hybrid device was found to operate with an enhanced efficiency exceeding the SQ limit in a single–junction cell. It was further shown that the second construction also enables the use of wide bandgap materials in the PV stage, opening novel perspectives in the selection of photovoltaic materials.

A word of caution is however to be spent. All the results reported, further to the standard simplifying assumptions the SQ limit rests upon, assume ideal heat dissipation conditions at the cold end of the TEG stage. Thermal matching and properly tuned thermal conductance of the whole HTEPV device may not be easy to achieve, especially if standard TEGs are used. The actual implementation of the constructs presented in this paper requires instead a TEG design optimized to meet the requirements set forth by Eq. A.8 or A.9. Further analyses of TEG design strategies meeting this aim without decreasing the actual efficiency of the HTEPV device are needed and will be addressed in forthcoming papers.

Appendix B

B.1 List of Publications

1. M. Acciarri, S. Binetti, A. Le Donne, **B. Lorenzi**, L. Caccamo, L. Miglio, R. Moneta, S. Marchionna, and M. Meschia, "Development of a hybrid sputtering/evaporation process for Cu(In,Ga)Se_2 thin film solar Cells", *Crystal Research Technology*, 1 6 (2011), doi: 10.1002/crat.201000670

2. N. Neophytou, X. Zianni, H. Kosina, S. Frabboni, **B. Lorenzi**, D. Narducci, "Simultaneous increase in electrical conductivity and Seebeck coefficient in highly boron-doped nanocrystalline Si", *Nanotechnology*, 24 (2013) 205402; doi: 10.1088/0957-4484/24/20/205402.

3. N. Neophytou, X. Zianni, H. Kosina, S. Frabboni, **B. Lorenzi**, D. Narducci, "Power factor enhancement by inhomogeneous distribution of dopants in two-phase nanocrystalline systems", *Journal of Electronic Materials*, Jun 2014, Vol. 43 Issue 6, pp 1896-1904, doi: 10.1007/s11664-013-2898-z

4. D. Narducci, **B. Lorenzi**, X. Zianni, N. Neophytou, S. Frabboni, G. C. Gazzadi, A. Roncaglia, F. Suriano, "Enhancement of the power factor in two-phase silicon-boron nanocrystalline alloys", *Physica Status Solidi A*, 211, No. 6, 12551258 (2014), doi: 10.1002/pssa.201300130

5. **B. Lorenzi**, D. Narducci, R. Tonini, S. Frabboni, G.C. Gazzadi,

G. Ottaviani, N. Neophytou, X. Zianni, "Paradoxical enhancement of the power factor in polycrystalline silicon due to the formation of nanovoids", *Journal of Electronic Materials*, Oct. 2014, Vol. 43, Issue 10, pp 3812-3816, doi: 10.1007/s11664-014-3170-x

6. **B. Lorenzi**, S. Frabboni, G. C. Gazzadi, R. Tonini, G. Ottaviani, D. Narducci, "Nanovoids Formation and Dynamics in He^+-implanted Nanocrystalline Silicon, *Journal of Electronic Materials*, Oct. 2014, Volume 43, Issue 10, pp 3852-3856, doi: 10.1007/s11664-014-3249-4

7. **B. Lorenzi** and D. Narducci, "Riduzione e recupero dei cascami termici: il contributo delle tecnologie", in L. De Paoli (ed.), *Efficienza energetica: governance, strumenti e mercato*, Fondazione EnergyLab, Edilplan Editrice; ISBN 978-88-96726-18-1

8. **B. Lorenzi**, M. Acciarri, D. Narducci, "Analysis of Thermal Losses in Various Single Junction Photovoltaic Cells - An Interesting Source for Thermoelectric Heat Recovery", *Journal of Electronic Materials*, December 2014, doi: 10.1007/s11664-014-3562-y

B.2 Conferences and Schools

1. Summer School on Emerging renewable energy conversion and storage, Lake Como, Italy, 9-13 September 2013

2. International Conference on Thermoelectrics - ICT 2014, Nashville, Tennessee, USA - July 6-10, 2014

   Poster Title: *Analysis of Thermal Losses in Various Single Junction Photovoltaic Cells - An Interesting Source for Thermoelectric Heat Recovery*

   Poster Title: *Thermotunneling Effect in Asymmetric Systems*

3. Giornate sulla Termoelettricità - GiTe 2015, Milano, Italy - February 18-19, 2015

Oral Presentation: *Modulation of the Thermal Properties of Nanocrystalline Silicon Thin Films with Creation of Nanovoids By He^+ Implantation*

Oral Presentation: *Losses in Single Junction Solar Cell for Thermoelectric Heat Recovery: a Theoretical Study*

References

[1] P. Gerland, a. E. Raftery, H. Ev Ikova, N. Li, D. Gu, T. Spoorenberg, L. Alkema, B. K. Fosdick, J. Chunn, N. Lalic, G. Bay, T. Buettner, G. K. Heilig, and J. Wilmoth, "World population stabilization unlikely this century," *Science*, vol. 234, 2014. xi, 1, 2

[2] BP, "Statistical Review of World Energy," tech. rep., June 2014. xi, 2, 3, 6

[3] Ren 21, "RENEWABLES 2014 GLOBAL STATUS REPORT," tech. rep., 2014. xi, 2, 5, 8

[4] C. B. Vining, "An inconvenient truth about thermoelectrics.," *Nature materials*, vol. 8, no. February, pp. 83–85, 2009. xi, 11, 12

[5] R. Amatya and R. J. Ram, "Trend for Thermoelectric Materials and Their Earth Abundance," *Journal of Electronic Materials*, vol. 41, pp. 1011–1019, Dec. 2011. xii, 33

[6] D. Narducci, E. Selezneva, A. Arcari, G. Cerofolini, E. Romano, R. Tonini, and G. Ottaviani, "Enhanced thermoelectric properties of strongly degenerate polycrystalline silicon upon second phase segregation," *Mater. Res. Soc. Symp. Proc.*, vol. 1314, pp. 1–6, 2011. xii, 42, 43

[7] D. Narducci, B. Lorenzi, X. Zianni, N. Neophytou, S. Frabboni, G. C. Gazzadi, A. Roncaglia, and F. Suriano, "Enhancement of the power factor in two-phase silicon-boron nanocrystalline alloys," *Physica Status Solidi (a)*, vol. 211, pp. 1255–1258, June 2014. xii, xiii, 49, 50

[8] N. Neophytou, X. Zianni, H. Kosina, S. Frabboni, B. Lorenzi, and D. Narducci, "Simultaneous increase in electrical conductivity and Seebeck coefficient in highly boron-doped nanocrystalline Si.," *Nanotechnology*, vol. 24, p. 205402, May 2013. xiii, 51, 52, 53

[9] W. Liu, K. Etessam-Yazdani, R. Hussin, and M. Asheghi, "Modeling and data for thermal conductivity of ultrathin single-crystal SOI layers at high temperature," *IEEE Transactions on Electron Devices*, vol. 53, no. 8, pp. 1868–1876, 2006. xiii, 57

[10] B. Lorenzi, S. Frabboni, G. C. Gazzadi, R. Tonini, G. Ottaviani, and D. Narducci, "Nanovoid Formation and Dynamics in He+-Implanted Nanocrystalline Silicon," *Journal of Electronic Materials*, vol. 43, pp. 3852–3856, June 2014. xiii, xiv, 65, 66, 67

[11] B. Lorenzi, D. Narducci, R. Tonini, S. Frabboni, G. C. Gazzadi, G. Ottaviani, N. Neophytou, and X. Zianni, "Paradoxical Enhancement of the Power Factor of Polycrystalline Silicon as a Result of the Formation of Nanovoids," *Journal of Electronic Materials*, vol. 43, pp. 3812–3816, May 2014. xiv, 70, 71

[12] J. Xie, C. Lee, M.-F. Wang, Y. Liu, and H. Feng, "Characterization of heavily doped polysilicon films for CMOS-MEMS thermoelectric power generators," *Journal of Micromechanics and Microengineering*, vol. 19, p. 125029, Dec. 2009. xiv, 42, 77

[13] I.-Y. Huang, G.-M. Chen, and T.-Y. Wu, "Development of microthermoelectric generators using integrated suspending bridge-type polysilicon thin-film thermopiles," *Journal of Micro/Nanolithography, MEMS, and MOEMS*, vol. 12, p. 013001, 2013. xiv, 42, 77

[14] M. Strasser, R. Aigner, C. Lauterbch, T. F. Sturm, M. Franosch, and G. Wachutka, "Macromachined cmos thermoelectric generators

as on-chip power supply," in *TRANSDUCERS 12th Int. Conf. Solid-State Sensors, Actuators Microsystems (IEEE, 2003)*, pp. 45–48., 2003. xiv, 42, 77

[15] B. Lorenzi, M. Acciarri, and D. Narducci, "Analysis of thermal losses for a variety of single-junction photovoltaic cells: An interesting means of thermoelectric heat recovery," *Journal of Electronic Materials*, pp. 1–5, 2014. xv, 91

[16] A. Weisman, *Countdown: Our Last, Best Hope for a Future on Earth?* Little, Brown Book Group, 2013. 1

[17] EIA, "International energy statistics," http://www.eia.gov/, 2011. 2

[18] NREL, "Life cycle assessment harmonization," http://www.nrel.gov/, 2014. 7

[19] A. Catalin, F. Covrig, M. Ardelean, J. Vasiljevska, A. Mengolini, G. Fulli, E. Amoiralis, M. S. Jiménez, and C. Filiou, "Smart Grid Projects Outlook 2014," tech. rep., Joint Research Centre, European Community, 2014. 9

[20] V. Linnhoff, Bodo and Sahdev, *Pinch Technology*. Wiley-VCH Verlag GmbH and Co. KGaA, 2000. 10

[21] EU, "Odyssee-mure project," http://www.odyssee-mure.eu/, 2014. 10

[22] C. Bullock and G. Caraghiaur, *A Guide to Energy Service Companies*. A Guide to Energy Service Companies, Fairmont Press, 2001. 11

[23] J. Karni, "Solar energy: the thermoelectric alternative.," *Nature materials*, vol. 10, no. 7, pp. 481–482, 2011. 11, 12

[24] D. Kraemer, B. Poudel, H.-P. Feng, J. C. Caylor, B. Yu, X. Yan, Y. Ma, X. Wang, D. Wang, A. Muto, K. McEnaney, M. Chiesa, Z. Ren, and G. Chen, "High-performance flat-panel solar thermoelectric generators with high thermal concentration.," *Nature materials*, vol. 10, no. 7, pp. 422–427, 2011. 12, 15, 86, 98

[25] A. Eder and M. Linde, "Efficient and dynamic–the bmw group roadmap for the application of thermoelectric generators," Presented at Second Thermoelectric Applications Workshop, San Diego, January 2011, available at www1.eere.energy.gov., 2011. 13

[26] V. Leonov and R. Vullers, "Wearable thermoelectric generators for body-powered devices," *Journal of Electronic Materials*, vol. 38, no. 7, pp. 1491–1498, 2009. 14

[27] M. Van Bavel, V. Leonov, Y. R. F., T. Torfs, C. Van Hoof, P. N. E., and V. R. J. M., "Wearable battery-free wireless 2-channel eeg systems powered by energy scavengers," *Sensors and Transducers Journal*, vol. 94, pp. 103–115, July 2008. 14

[28] T. Torfs, V. Leonov, and V. R. J. M., "Pulse oximeter fully powered by human body heat," *Sensors and Transducers Journal*, vol. 80, pp. 1230–1238, June 2007. 14

[29] V. Leonov, "Thermoelectric energy harvester on the heated human machine," *Journal of Micromechanics and Microengineering*, vol. 21, no. 12, p. 125013, 2011. 14

[30] V. Leonov, T. Torfs, P. Fiorini, and C. Van Hoof, "Thermoelectric converters of human warmth for self-powered wireless sensor nodes," *Sensors Journal, IEEE*, vol. 7, pp. 650–657, May 2007. 14

[31] H. Najafi, *Evaluation of alternative cooling techniques for photovoltaic panels*. PhD thesis, 2012. 15

[32] N. Wang, L. Han, H. He, N.-H. Park, and K. Koumoto, "A novel high-performance photovoltaicâthermoelectric hybrid device," *Energy and Environmental Science*, vol. 4, pp. 422–427, 2011. 15, 86

[33] W. G. J. H. M. V. Sark, "Feasibility of photovoltaic - Thermoelectric hybrid modules," *Applied Energy*, vol. 88, pp. 2785–2790, 2011. 15

[34] X. Z. Guo, Y. D. Zhang, D. Qin, Y. H. Luo, D. M. Li, Y. T. Pang, and Q. B. Meng, "Hybrid tandem solar cell for concurrently converting light and heat energy with utilization of full solar spectrum," *Journal of Power Sources*, vol. 195, no. 22, pp. 7684–7690, 2010. 15

[35] Y. Vorobiev, J. González-Hernández, P. Vorobiev, and L. Bulat, "Thermal-photovoltaic solar hybrid system for efficient solar energy conversion," *Solar Energy*, vol. 80, pp. 170–176, 2006. 15

[36] D. Kraemer, L. Hu, A. Muto, X. Chen, G. Chen, and M. Chiesa, "Photovoltaic-thermoelectric hybrid systems: A general optimization methodology," *Applied Physics Letters*, vol. 92, no. 243503, 2008. 15

[37] A. F. Ioffe, *Semiconductor thermoelements, and Thermoelectric cooling.* Infosearch, ltd., 1957. 21

[38] D. Narducci, "Do we really need high thermoelectric figures of merit? A critical appraisal to the power conversion efficiency of thermoelectric materials," *Applied Physics Letters*, vol. 99, no. 10, p. 102104, 2011. 21

[39] S. Ali and Z. Mona, "Nanoengineered Materials for Thermoelectric Energy Conversion," in *Thermal Nanosystems and Nanomaterials* (V. Sebastian, ed.), pp. 225 – 299, Springer, 2009. 25

[40] G. Kumar, G. Prasad, and R. Pohl, "Experimental determinations of the lorenz number," *Journal of Materials Science*, vol. 28, no. 16, pp. 4261–4272, 1993. 27

[41] F. Rosi, "Thermoelectricity and thermoelectric power generation," *Solid-State Electronics*, vol. 11, pp. 833–868, Sept. 1968. 32

[42] C. Wood, "Materials for thermoelectric energy conversion," *Reports on Progress in Physics*, vol. 51, no. 4, p. 459, 1988. 32

[43] R. R. C. and R. R. J., "Alpha-plot in sigma-plot as a thermoelectric-material performance indicator," *J. Mater. Sci. Lett.*, vol. 14, pp. 617–619, 1995. 32

[44] Y. Gelbstein, Z. Dashevsky, and M. P. Dariel, "High performance n-type PbTe-based materials for thermoelectric applications," *Physica B-condensed Matter*, vol. 363, no. 1, pp. 196–205, 2005. 32

[45] D. Wu, L.-D. Zhao, S. Hao, Q. Jiang, F. Zheng, J. W. Doak, H. Wu, H. Chi, Y. Gelbstein, C. Uher, C. Wolverton, M. Kanatzidis, and J. He, "Origin of the High Performance in GeTe-Based Thermoelectric Materials upon Bi2Te3 Doping," *Journal of the American Chemical Society*, vol. 136, no. 32, pp. 11412–11419, 2014. 32

[46] J. L. Feldman, D. J. Singh, I. I. Mazin, D. Mandrus, and B. C. Sales, "Lattice dynamics and reduced thermal conductivity of filled skutterudites," *Phys. Rev. B*, vol. 61, pp. R9209–R9212, Apr. 2000. 32

[47] S. Chen and Z. Ren, "Recent progress of half-Heusler for moderate temperature thermoelectric applications," *Materials Today*, vol. 16, no. 10, pp. 387–395, 2013. 32

[48] K. Kurosaki, A. Kosuga, H. Muta, M. Uno, and S. Yamanaka, "Ag(9)TlTe(5): A high-performance thermoelectric bulk material with extremely low thermal conductivity," *Applied Physics Letters*, vol. 87, no. 6, pp. –, 2005. 32

[49] T. Caillat, J.-P. Fleurial, and A. Borshchevsky, "Preparation and thermoelectric properties of semiconducting Zn(4)Sb(3)," *Journal of Physics and Chemistry of Solids*, vol. 58, no. 7, pp. 1119–1125, 1997. 32

[50] F. Gascoin, S. Ottensmann, D. Stark, S. M. Haïle, and G. J. Snyder, "Zintl Phases as Thermoelectric Materials: Tuned Transport Properties of the Compounds Ca(x)Yb(1-x)Zn(2)Sb(2)," *Advanced Functional Materials*, vol. 15, no. 11, pp. 1860–1864, 2005. 32

[51] N. Chen, F. Gascoin, G. J. Snyder, E. Müller, G. Karpinski, and C. Stiewe, "Macroscopic thermoelectric inhomogeneities in [AgSbTe(2)](x) [PbTe](1-x)," *Applied Physics Letters*, vol. 87, no. 17, pp. –, 2005. 32

[52] I. Terasaki, Y. Sasago, and K. Uchinokura, "Large thermoelectric power in naco(2)o(4) single crystals," , vol. 56, p. 12685, Nov. 1997. 33

[53] T. Tsubota, M. Ohtaki, K. Eguchi, and H. Arai, "Thermoelectric properties of Al-doped ZnO as a promising oxide material for high-temperature thermoelectric conversion," *J. Mater. Chem.*, vol. 7, no. 1, pp. 85–90, 1997. 33

[54] M. Akasaka, T. Iida, A. Matsumoto, K. Yamanaka, Y. Takanashi, T. Imai, and N. Hamada, "The thermoelectric properties of bulk crystalline n- and p-type Mg(2)Si prepared by the vertical Bridgman method," *Journal of Applied Physics*, vol. 104, no. 1, pp. –, 2008. 33

[55] T. Sakamoto, T. Iida, N. Fukushima, Y. Honda, M. Tada, Y. Taguchi, Y. Mito, H. Taguchi, and Y. Takanashi, "Thermoelectric properties and power generation characteristics of sintered undoped n-type Mg2Si," *Thin Solid Films*, vol. 519, no. 24, pp. 8528–8531, 2011. 33

[56] L. D. Hicks and M. S. Dresselhaus, "Effect of quantum-well structures on the thermoelectric bgure of merit," *PHYSICAL REVIEW B*, vol. 47, no. 19, pp. 727–731, 1993. 34

[57] L. D. Hicks and M. S. Dresselhaus, "Thermoelectric figure of merit of a one-dimensional conductor," *PHYSICAL REVIEW B*, vol. 47, no. 24, pp. 8–11, 1993. 34

[58] S. V. Faleev and F. Léonard, "Theory of enhancement of thermoelectric properties of materials with nanoinclusions," *Physical Review B - Condensed Matter and Materials Physics*, vol. 77, no. March, pp. 1–9, 2008. 35

[59] J. Zide, D. Vashaee, Z. Bian, G. Zeng, J. Bowers, a. Shakouri, and a. Gossard, "Demonstration of electron filtering to increase the Seebeck coefficient in In0.53Ga0.47AsâIn0.53Ga0.28Al0.19As superlattices," *Physical Review B*, vol. 74, p. 205335, Nov. 2006. 35

[60] A. Popescu, L. Woods, J. Martin, and G. Nolas, "Model of transport properties of thermoelectric nanocomposite materials," *Physical Review B*, vol. 79, p. 205302, May 2009. 35

[61] L. P. Bulat, I. a. Drabkin, V. V. Karataev, V. B. Osvenskii, Y. N. Parkhomenko, D. a. Pshenai-Severin, G. I. Pivovarov, and N. Y. Tabachkova, "Energy filtration of charge carriers in a nanostructured material based on bismuth telluride," *Physics of the Solid State*, vol. 53, no. 1, pp. 29–34, 2011. 35

[62] R. Kim and M. S. Lundstrom, "Computational study of energy filtering effects in one-dimensional composite nano-structures," *Journal of Applied Physics*, vol. 111, no. 2, p. 024508, 2012. 35

[63] A. Shakouri, "Recent Developments in Semiconductor Thermoelectric Physics and Materials," *Annual Review of Materials Research*, vol. 41, pp. 399–431, Aug. 2011. 35

[64] A. I. Boukai, Y. Bunimovich, J. Tahir-Kheli, J.-K. Yu, W. a. Goddard, and J. R. Heath, "Silicon nanowires as efficient thermoelectric materials.," *Nature*, vol. 451, pp. 168–71, Jan. 2008. 35, 39

[65] A. I. Hochbaum, R. Chen, R. D. Delgado, W. Liang, E. C. Garnett, M. Najarian, A. Majumdar, and P. Yang, "Enhanced thermoelectric performance of rough silicon nanowires.," *Nature*, vol. 451, pp. 163–7, Jan. 2008. 35, 39

[66] E. B. Ramayya and I. Knezevic, "Ultrascaled silicon nanowires as efficient thermoelectric materials," *Proceedings - 2009 13th International Workshop on Computational Electronics, IWCE 2009*, no. Iwce, pp. 25–28, 2009. 36

[67] Y. Hasegawa, M. Murata, D. Nakamura, and T. Komine, "Reducing thermal conductivity of thermoelectric materials by using a narrow wire geometry," *Journal of Applied Physics*, vol. 106, no. 2009, 2009. 36

[68] N. Mingo, L. Yang, D. Li, and A. Majumdar, "Predicting the Thermal Conductivity of Si and Ge Nanowires," *Nano Letters*, vol. 3, pp. 1713–1716, 2003. 36

[69] T. T. M. Vo, A. J. Williamson, V. Lordi, and G. Galli, "Atomistic design of thermoelectric properties of silicon nanowires," 2008. 36

[70] D. Narducci, G. Cerofolini, M. Ferri, F. Suriano, F. Mancarella, L. Belsito, S. Solmi, and A. Roncaglia, "Phonon scattering enhancement in silicon nanolayers," *Journal of Materials Science*, vol. 48, pp. 2779–2784, Sept. 2012. 36, 38, 39

[71] R. Venkatasubramanian, E. Siivola, T. Colpitts, and B. O'Quinn, "Thin-film thermoelectric devices with high room-temperature figures of merit.," *Nature*, vol. 413, pp. 597–602, Oct. 2001. 36

[72] J. C. Caylor, K. Coonley, J. Stuart, T. Colpitts, and R. Venkatasubramanian, "Enhanced thermoelectric performance in PbTe-based superlattice structures from reduction of lattice thermal conductivity," *Applied physics letters*, vol. 87, no. 2, p. 23105, 2005. 36

[73] X. Fan, G. Zeng, C. LaBounty, J. E. Bowers, E. Croke, C. C. Ahn, S. Huxtable, A. Majumdar, and A. Shakouri, "SiGeC/Si superlattice microcoolers," *Applied Physics Letters*, vol. 78, no. 11, p. 1580, 2001. 36

[74] C. Chiritescu, D. G. Cahill, N. Nguyen, D. Johnson, A. Bodapati, P. Keblinski, and P. Zschack, "Ultralow thermal conductivity in disordered, layered WSe(2) crystals.," *Science (New York, N.Y.)*, vol. 315, pp. 351–3, Jan. 2007. 36

[75] F. Yang, T. Ikeda, G. J. Snyder, and C. Dames, "Effective thermal conductivity of polycrystalline materials with randomly oriented superlattice grains," *Journal of Applied Physics*, vol. 108, no. 3, p. 034310, 2010. 36

[76] D. G. Cahill, P. V. Braun, G. Chen, D. R. Clarke, S. Fan, K. E. Goodson, P. Keblinski, W. P. King, G. D. Mahan, A. Majumdar, H. J. Maris, S. R. Phillpot, E. Pop, and L. Shi, "Nanoscale thermal transport. II. 2003-2012," *Applied Physics Reviews*, vol. 1, pp. 1–45, 2014. 36

[77] P. K. Samantray, P. Karthikeyan, and K. Reddy, "Estimating effective thermal conductivity of two-phase materials," *International Journal of Heat and Mass Transfer*, vol. 49, pp. 4209–4219, Oct. 2006. 36

[78] X. Y. Li, X. L. Zhao, X. Y. Guo, Z. M. Shao, and M. X. Ai, "New theoretical equation for effective thermal conductivity of two-phase composite materials," *Materials Science and Technology*, vol. 28, no. 5, pp. 620–626, 2012. 36

[79] K. S. Reddy and P. Karthikeyan, "Estimation of Effective Thermal Conductivity of Two-Phase Materials Using Collocated Parameter Model," *Heat Transfer Engineering*, vol. 30, no. 12, pp. 998–1011, 2009. 36

[80] C. Hua and A. J. Minnich, "Importance of frequency-dependent grain boundary scattering in nanocrystalline silicon and silicon-germanium thermoelectrics," *Semicond. Sci. Technol.*, vol. 29, Apr. 2014. 36, 76

[81] A. S. Henry and G. Chen, "Spectral phonon transport properties of silicon based on molecular dynamics simulations and lattice dynamics," *Journal of Computational and Theoretical Nanoscience"*, vol. 5, no. 2, pp. 141–152, 2008. 36

[82] Z. Tian, K. Esfarjani, J. Shiomi, A. S. Henry, and G. Chen, "On the importance of optical phonons to thermal conductivity in nanostructures," *Applied Physics Letters*, vol. 99, no. 5, 2011. 36

[83] L.-D. Zhao, V. P. Dravid, and M. G. Kanatzidis, "The panoscopic approach to high performance thermoelectrics," *Energy and Environmental Science*, vol. 7, p. 251, 2014. 36

[84] a. J. Minnich, M. S. Dresselhaus, Z. F. Ren, and G. Chen, "Bulk nanostructured thermoelectric materials: current research and future prospects," *Energy and Environmental Science*, vol. 2, p. 466, 2009. 36

[85] G. F. Cerofolini, M. Ferri, E. Romano, F. Suriano, G. P. Veronese, S. Solmi, and D. Narducci, "Terascale integration via a redesign of the crossbar based on a vertical arrangement of poly-Si nanowires," *Semiconductor Science and Technology*, vol. 25, p. 095011, Sept. 2010. 37

[86] J. P. Heremans, M. S. Dresselhaus, L. E. Bell, and D. T. Morelli, "When thermoelectrics reached the nanoscale," vol. 8, no. July, pp. 471–473, 2013. 38

[87] D. L. Young, H. M. Branz, F. Liu, R. Reedy, B. To, and Q. Wang, "Electron transport and band structure in phosphorus-doped polycrystalline silicon films," *Journal of Applied Physics*, vol. 105, no. 2009, 2009. 42

[88] D. Narducci, E. Selezneva, G. Cerofolini, S. Frabboni, and G. Ottaviani, "High figures of merit in degenerate semiconductors. Energy filtering by grain boundaries in heavily doped polycrystalline silicon," *AIP Conference Proceedings*, vol. 1449, pp. 311–314, 2012. 42

[89] D. Narducci, E. Selezneva, G. Cerofolini, S. Frabboni, and G. Ottaviani, "Impact of energy filtering and carrier localization on the thermoelectric properties of granular semiconductors," *Journal of Solid State Chemistry*, vol. 193, pp. 19–25, 2012. 42

[90] G. L. Vick and K. M. Whittle, "Solid Solubility and Diffusion Coefficients of Boron in Silicon," *Journal of The Electrochemical Society*, vol. 116, p. 1142, 1969. 42, 45

[91] R. Heikes and R. W. Ure, *Thermoelectricity: Science and Engineering*. New York: Interscience, 1961. 46

[92] T. H. Geballe and G. W. Hull, "Seebeck Effect in Silicon," *PHYSICAL REVIEW*, vol. 98, no. 4, 1955. 47, 49

[93] L. J. van der Pauw, "A method of measuring specific resistivity and hall effect of discs of arbitrary shape," *Philips Research Reports*, vol. 13, no. 1, pp. 1–9, 1958. 47

[94] L. J. van der Pauw, "A method of measuring the resisticity and hall coefficient on lamellae of arbitrary shape," *Philips technical review*, vol. 20, pp. 220–224, 1958. 47

[95] M. M. Mandurah, K. C. Saraswat, C. R. Helms, and T. I. Kamins, "Dopant segregation in polycrystalline silicon," *Journal of applied physics*, vol. 51, no. 11, pp. 5755–5763, 1980. 48

[96] W. Fulkerson, J. P. Moore, R. K. Williams, R. S. Graves, and D. L. McElroy, "Thermal Conductivity, Electrical Resistivity, and Seebeck Coefficient of Silicon from 100 to 1300 K," *Phys. Rev.*, vol. 167, pp. 765–782, Mar. 1968. 49

[97] C. N. Liao, C. Chen, and K. N. Tu, "Thermoelectric characterization of Si thin films in silicon-on-insulator wafers," *Journal of Applied Physics*, vol. 86, no. 6, p. 3204, 1999. 49

[98] X. Luo, S. B. Zhang, and S.-H. Wei, "Understanding Ultrahigh Doping: The Case of Boron in Silicon," *Phys. Rev. Lett.*, vol. 90, no. 2, p. 26103, 2003. 50

[99] F. S. Ham, "Theory of diffusion-limited growth," *Journal of Physics and Chemistry in Solids*, vol. 6, no. 4, pp. 335–351, 1958. 50

[100] N. Neophytou, X. Zianni, H. Kosina, S. Frabboni, B. Lorenzi, and D. Narducci, "Power Factor Enhancement by Inhomogeneous Distribution of Dopants in Two-Phase Nanocrystalline Systems," *Journal of Electronic Materials*, vol. 43, pp. 1896–1904, Nov. 2013. 51

[101] J. W. Orton and M. J. Powell, "The Hall effect in polycrystalline and powdered semiconductors," *Reports on Progress in Physics*, vol. 43, no. 11, p. 1263, 1980. 52

[102] V. Raineri, "Gettering by Voids in Silicon: A Comparison with other Techniques," *Solid State Phenomena*, vol. 57 - 58, no. 43, pp. 43–52, 1997. 58

[103] J. Wong-Leung, C. E. Ascheron, M. Petravic, R. G. Elliman, and J. S. Williams, "Gettering of copper to hydrogen-induced cavities in silicon," *Applied physics letters*, vol. 66, no. 10, pp. 1231–1233, 1995. 58

[104] M. H. F. Overwijk, J. Politiek, R. C. M. de Kruif, and P. C. Zalm, "Proximity gettering of transition metals in silicon by ion implantation," *Nuclear Instruments and Methods in Physics Research Section B-beam Interactions With Materials and Atoms*, vol. 96, no. 1, pp. 257–260, 1995. 58

[105] B. Mohadjeri, J. S. Williams, and J. Wong-Leung, "Gettering of nickel to cavities in silicon introduced by hydrogen implantation," *Applied Physics Letters*, vol. 66, no. 15, p. 1889, 1995. 58

[106] S. M. Myers, G. A. Petersen, and C. H. Seager, "Binding of cobalt and iron to cavities in silicon," *Journal of Applied Physics*, vol. 80, no. 7, p. 3717, 1996. 58

[107] S. M. Myers and G. A. Petersen, "Transport and reactions of gold in silicon containing cavities," *Phys. Rev. B*, vol. 57, pp. 7015–7026, Mar. 1998. 58

[108] V. Raineri and S. U. Campisano, "Secondary defect dissolution by voids in silicon," *Applied Physics Letters*, vol. 69, no. 12, 1996. 58

[109] V. Raineri and S. Campisano, "Voids in silicon as sink for interstitials," *Nuclear Instruments and Methods in Physics Research Section B: Beam Interactions with Materials and Atoms*, vol. 120, pp. 56–59, Dec. 1996. 58

[110] C. H. Seager, S. M. Myers, R. A. Anderson, W. L. Warren, and D. M. Follstaedt, "Electrical properties of He-implantation-produced nanocavities in silicon," *Phys. Rev. B*, vol. 50, no. 4, pp. 2458–2473, 1994. 58

[111] V. Raineri, P. G. Fallica, G. Percolla, A. Battaglia, M. Barbagallo, and S. U. Campisano, "Gettering of metals by voids in silicon," *Journal of Applied Physics*, vol. 78, no. 6, p. 3727, 1995. 58

[112] M. Saggio, V. Raineri, R. Letor, and F. Frisina, "Innovative localized lifetime control in high-speed IGBT's," *IEEE Electron Device Letters*, vol. 18, no. 7, pp. 333–335, 1997. 58

[113] G. F. Cerofolini, F. Corni, S. Frabboni, C. Nobili, G. Ottaviani, and R. Tonini, "Hydrogen and helium bubbles in silicon," *Materials Science and Engineering*, vol. 27, pp. 1–52, 2000. 58, 67

[114] E. Romano, D. Narducci, F. Corni, S. Frabboni, G. Ottaviani, R. Tonini, and G. F. Cerofolini, "Nanocavities in silicon: An infrared investigation of internal surface reconstruction after hydrogen implantation," *Materials Science and Engineering B: Solid-State*

Materials for Advanced Technology, vol. 159-160, pp. 173–176, 2009. 58, 67

[115] V. Raineri, M. Saggio, and E. Rimini, "Voids in Silicon by He Implantation: From Basic to Applications," *Journal of Materials Research*, vol. 15, pp. 1449–1477, 2000. 58, 65, 67, 68, 73, 76

[116] E. Selezneva, *Physical and Chemical Aspects of Thermoelectric Phenomena in Nanostructured Materials*. PhD thesis, 2012. 59

[117] J. F. Ziegler, "Particle interaction with matter," http://www.srim.org/. 59

[118] G. H. Kinchin and R. S. Pease, "The Displacement of Atoms in Solids by Radiation," *Reports on Progress in Physics*, vol. 18, no. 1, p. 1, 1955. 59

[119] F. Corni, C. Nobili, G. Ottaviani, R. Tonini, G. Calzolari, G. F. Cerofolini, and G. Queirolo, "Helium in silicon: Thermal-desorption investigation of bubble precursors," *Phys. Rev. B*, vol. 56, no. 12, pp. 7331–7338, 1997. 61

[120] G. F. Cerofolini, G. Calzolari, F. Corni, S. Frabboni, C. Nobili, G. Ottaviani, and R. Tonini, "Thermal desorption spectra from cavities in helium-implanted silicon," *Phys. Rev. B*, vol. 61, pp. 10183–10193, Apr. 2000. 61

[121] D. G. Cahill, "Analysis of heat flow in layered structures for time-domain thermoreflectance," *Review of Scientific Instruments*, vol. 75, pp. 5119–5122, 2004. 63

[122] C. A. Paddock and G. L. Eesley, "Transient thermoreflectance from thin metal films," *Journal of Applied Physics*, vol. 60, no. 1, pp. 285–290, 1986. 63

[123] D. G. Cahill, K. Goodson, and A. Majumdar, "Thermometry and Thermal Transport in Micro/Nanoscale Solid-State Devices and Structures," *Journal of Heat Transfer*, vol. 124, no. April, p. 223, 2002. 63

[124] S. Frabboni, F. Corni, C. Nobili, R. Tonini, and G. Ottaviani, "Nanovoid formation in helium-implanted single-crystal silicon studied by in situ techniques," *Phys. Rev. B*, vol. 69, p. 165209, Apr. 2004. 64

[125] J. Adey, R. Jones, D. W. Palmer, P. R. Briddon, and S. Öberg, "Theory of boron-vacancy complexes in silicon," *Phys. Rev. B*, vol. 71, p. 165211, Apr. 2005. 73

[126] D. Chattopadhyay and H. J. Queisser, "Electron scattering by ionized impurities in semiconductors," *Rev. Mod. Phys.*, vol. 53, no. 4, pp. 745–768, 1981. 73

[127] A. D. McConnell, S. Uma, and K. E. Goodson, "Thermal conductivity of doped polysilicon layers," *Journal of Microelectromechanical Systems*, vol. 10, no. 3, pp. 360–369, 2001. 74

[128] S. Uma, a. D. McConnell, M. Asheghi, K. Kurabayashi, and K. E. Goodson, "Temperature-dependent thermal conductivity of undoped polycrystalline silicon layers," *International Journal of Thermophysics*, vol. 22, pp. 605–616, 2001. 74

[129] T. Ackbarow and M. J. Buehler, "Hierarchical coexistence of universality and diversity controls robustness and multi-functionality in protein materials," *Journal of Computational and Theoretical Nanoscience*, vol. 5, no. 2, pp. 1193–1204, 2008. 76

[130] Z. Tian, K. Esfarjani, J. Shiomi, A. S. Henry, and G. Chen, "On the importance of optical phonons to thermal conductivity in nanostructures," *Applied Physics Letters*, vol. 99, 2011. 76

[131] X. Li and R. Yang, "Effect of lattice mismatch on phonon transmission and interface thermal conductance across dissimilar material interfaces," *Phys. Rev. B*, vol. 86, no. 5, p. 54305, 2012. 76

[132] Z. Tian, K. Esfarjani, and G. Chen, "Green's function studies of phonon transport across Si/Ge superlattices," *Physical Review B*, vol. 89, no. 23, p. 235307, 2014. 76

[133] Z. Wang, J. E. Alaniz, W. Jang, J. E. Garay, and C. Dames, "Thermal Conductivity of Nanocrystalline Silicon: Importance of Grain Size and Frequency-Dependent Mean Free Paths," *Nano Letters*, vol. 11, no. 6, pp. 2206–2213, 2011. 76

[134] W. Shockley and H. J. Queisser, "Detailed balance limit of efficiency of p-n junction solar cells," *Journal of Applied Physics*, vol. 32, no. 1961, pp. 422–427, 1961. 85, 87, 88

[135] J. L. Gray, "The physics of the solar cell," in *Handbook of Photovoltaic Science and Engineering* (L. Antonio and H. Steven, eds.), pp. 61–111, John Wiley and Sons Ltd, 2003. 85, 89

[136] T. T. Chow, "A review on photovoltaic/thermal hybrid solar technology," vol. 87, no. 2, pp. 422–427, 2010. 86

[137] B. Parida, S. Iniyan, and R. Goic, "A review of solar photovoltaic technologies," *Renewable and Sustainable Energy Reviews*, vol. 15, no. 3, pp. 422–427, 2011. 86

[138] K.-T. Park, S.-M. Shin, A. S. Tazebay, H.-D. Um, J.-Y. Jung, S.-W. Jee, M.-W. Oh, S.-D. Park, B. Yoo, C. Yu, and J.-H. Lee, "Lossless hybridization between photovoltaic and thermoelectric devices.," *Scientific reports*, vol. 3, pp. 422–427, 2013. 86, 99

[139] P. T. Landsberg and P. Baruch, "The thermodynamics of the conversion of radiation energy for photovoltaics," *Journal of Physics A: Mathematical and General*, vol. 22, no. 11, p. 1911, 1989. 86

[140] ASTM, "ASTM G173-03(2012), Standard Tables for Reference Solar Spectral Irradiances: Direct Normal and Hemispherical on 37 Tilted Surface," pp. 422–427, 2012. 88

[141] G. Friesen, D. Pavanello, and A. Virtuani, "Overview of Temperature Coefficients of Different Thin Film Photovoltaic Technologies," pp. 422–427, 2010. 90

[142] T. Nordmann and L. Clavadetscher, "Understanding temperature effects on PV system performance," *3rd World Conference onPhotovoltaic Energy Conversion, 2003. Proceedings of*, vol. 3, pp. 422–427, 2003. 90, 96

[143] E. Skoplaki and J. a. Palyvos, "On the temperature dependence of photovoltaic module electrical performance: A review of efficiency/power correlations," *Solar Energy*, vol. 83, no. 5, pp. 422–427, 2009. 90, 98

[144] M. Fuentes, *A simplified thermal model for Flat-Plate photovoltaic arrays*. May 1987. 90

[145] D. K. Schroder, *Semiconductor Material and Device Characterization*. A Wiley-Interscience publication, Wiley, 1998. 92

[146] S. M. Sze, *Physics of Semiconductor Devices*. Wiley, 1981. 93